The Pennsylvania State University

The Graduate School

Department of Physics

STUDIES OF THE HIGH MOMENTUM TRANSFER HARD QUASI-EXCLUSIVE PP INTERACTIONS WITH EVA DETECTOR

A Thesis in

Physics

by

Daniel Zhalov

Submitted in Partial Fulfillment
of the Requirements
for the Degree of

Doctor of Philosophy

December 2001

We approve the thesis of Daniel Zhalov.

Date of Signature

Steven F. Heppelmann
Associate Professor of Physics
Thesis Adviser
Chair of Committee

Mark I. Strikman
Professor of Physics

Richard W. Robinett
Professor of Physics

Pablo Laguna
Professor of Astronomy and Astrophysics

Jayanth R. Banavar
Professor of Physics
Head of the Department of Physics

ABSTRACT

We report the new effects observed in $pp \to ppX$ reaction. The data was collected using the EVA apparatus. EVA is a part of the E850 experiment, located at the AGS (Alternating Gradient Synchrotron) in Brookhaven National Laboratory.

We study the inclusive $pp \to ppX$ processes using the kinematic variable X_L. This variable is called the fraction of the incident longitudinal momentum observed in the 'two-track' final state. We discuss an interesting effect of the shift in the X_L distribution for the nuclear target when compared to the X_L distribution for the Hydrogen target.

The unexpected dependences in the distributions of the missing transverse momentum are observed in the more constrained set of data, which consists of $pp \to pp\pi^0$ processes. The P_T^2 distribution for the events in this set is flat in the wide range of values. The expected behavior of this distribution is an exponential fall off. We also observe a puzzling asymmetry for the components of the missing momentum. We propose a possible explanation of these effects.

Table of Contents

List of Tables

List of Figures

ACKNOWLEDGMENTS

I would like to express my gratitude to Dr. Steven F. Heppelmann for making me a member of the E850 experiment, directing and supervising the research described in this thesis and useful discussions of the underlying physics in the analysis. I wish to thank Dr. Alan Carroll and Dr. Eli Piasetzky for their help and advice during the data acquisition time as well as their participation in the preparation of this work. I am indebted to Dr. Vitalii Baturin, Dr. Aleksandr Schetkovsky and to all the members of the E850 collaboration for sharing with me their knowledge and experience. It is my great pleasure to express my appreciation to Dr. Mark Strikman and to my father, Dr. Mikhail Zhalov, for the numerous theoretical discussions and support during the years of work. Finally, I am very grateful to Ms. Claire Anderson for her continuous support and understanding that sometimes graduate students have to work long hours.

I would like to dedicate this work to my family. My interest in physics was sparked by my Mother and my Father long ago. Their devotion and support have kept me focused over the many years of study and work. I am happy to be able to express the gratitude to my parents in this dedication . . .

Chapter 1

Introduction

We report, from experiment E850, the new effects observed in the $pp \rightarrow ppX$ reactions. These are the reactions of the proton-proton scattering into two final state protons and extra particles X.

The E850 experiment was designed to study the Color Transparency Phenomenon. It was the main focus of the research in previous years.

The signal in this analysis of the recent years consisted of the elastic and quasi-elastic events. These come from the proton scattering on a proton in Hydrogen or nuclear target. The elastic process in the kinematics of the detector has a very small cross section. We analyzed some features of the elastic and quasi-elastic events [1, 2, 3]. There is a large background under the elastic signal. We used the 'background' events in a large part of our research.

The background consists of many types of semi-exclusive processes. It is possible to study these processes due to the very large spatial coverage of the spectrometer. The background events proved to have a number of exciting features. We observed unexpected trends in the distributions of the kinematic variables.

For example, we studied the missing transverse momentum squared distributions for

$pp \rightarrow pp\pi^0$ reaction. In this reaction, the missing transverse momentum (P_t) is the transverse momentum of π^0. In the kinematic region of the π^0 production the $\frac{d\sigma}{dP_t^2}$ distribution has a lack of events at $P_t^2 \sim 0$ and a flat distribution which falls off around $P_t^2 \sim 0.8(Gev/c)^2$. We cannot explain this dependence using the existing models for pion production. We propose that the features of these distributions can be a consequence of the process of the hard scattering.

The experiment was designed to select elastic proton-proton scattering at the angles close to 90° in the Center of Mass frame. These angles are characteristic of the hard scattering. The cross section of the hard 90° scattering has a very strong dependence on the Mandelstam variable s ($s = (\hat{P}_{inc} + \hat{P}_{target})^2 = E_{CM}^2$).

It was shown that the dependence has a scaling law $\frac{d\sigma_{90^\circ}}{dt} \sim s^{-m}$ [4]. The power of the dependence is related to the number of constituents taking part in the scattering. It was also predicted that the scattered particles may collapse to a smaller size.

A nucleus was used in the experiments to filter the small objects. The measure of the interaction of the particles with nucleus is called the nuclear transparency. It was expected that for the smaller objects the interaction with the nucleus is suppressed. The increase of the nuclear transparency due to the suppression of the initial and final state interactions of particles and nucleus was given the name of **color transparency**.

The trends of the transparency were extensively discussed in many theoretical studies [5, 6, 7, 8, 9, 10, 11, 12]. There were five experiments that reported results on the **color transparency** effect [13, 14, 15, 16, 17, 2]. These experiments studied the dependence of the color transparency on energy, momentum transfer and A-nuclear number.

In the E850 experiment we study, among other things, the energy dependence of the

color transparency. It is shown to have a non-trivial energy dependence. The energy trend is drastically different from the conventional nuclear absorption picture [2, 3].

The transparency increases from the level of Glauber calculations [9] (in Glauber calculations there are no **color transparency** effects) at 6 GeV to almost twice the value of the transparency at 9 GeV. The transparency decreases back to the Glauber level around 13 GeV. The rise of the nuclear transparency can be an indication that the small objects are created in the hard elastic scattering.

The hard quasi-elastic scattering may be a part of the explanation of another result obtained in the analysis of the backward neutrons production in Carbon [18]. The neutron detectors are the integral part of our experiment. The neutron counter arrays are used to detect the backward going neutrons in coincidence with the main event.

A very intriguing observation is made in the analysis. The yield of backward neutrons is 4-5 times larger then the yields obtained in other experiments that studied backward neutron production. The event selection process in the E850 experiment has a special kinematic constraint. Only the events with high transverse momentum tracks are accepted. Other experiments have more inclusive selection.

A strong s-dependence of the cross section leads to the selection of the protons in Carbon that have a large forward longitudinal component of the nuclear momentum. The large nuclear momentum component may be associated with the short-range nucleon-nucleon correlations. One of the Carbon's neutrons can be a correlated partner of the scattered proton. In the process of the proton knock-out in the hard scattering the recoiling neutron travels in the backward direction.

Large neutron production may not be a surprise in the case of hard quasi-elastic scat-

tering. In this case proton-proton scattering is known to have a strong s^{-10} dependence. However, the same large yield is observed in a more general class of events that do not satisfy the quasi-elastic criteria. Can it be an indication of the strong s-dependence in the underlying cross section of the inclusive background? This question has motivated the analysis that we have done for this thesis.

In the analysis we choose a certain class of the semi-exclusive processes. We select the events with a small missing mass. It is of the order of the mass of a pion. The sample consists of the events with two high P_T (transverse momentum) tracks and a missing pion. We impose a condition to have no extra tracks in the chambers. With this condition the missing pion can only be a π^0.

There are several ways to create a π^0 in proton-proton scattering. It can be created in the process of a resonance decay. In this case the resonance is formed in the proton-proton scattering. A pion can also be produced directly in the hard vertex during the scattering. In the third case a pion is emitted via the proton fragmentation in the initial or final state. Initial state fragmentation is followed by a hard proton-proton scattering ('star dust' type process [19, 20]). We emphasize the importance of a, possibly dominant, Landshoff mechanism (type of proton-proton scattering) with gluon bremsstrahlung.

These processes have a different s-dependence of the cross section but they occupy the same phase space in our kinematics at our energy. It is not possible to distinguish between these cases using kinematic cuts. We characterize a number of the distributions of the kinematic variables. Based on the shapes of the distributions and Monte-Carlo simulations we eliminate some of the possible explanations of the nature of the studied events.

We propose an explanation of the observed effect. The explanation is based on the

suppression of the radiation of the small objects undergoing the hard scattering via the Landshoff mechanism.

The thesis is written in the following order.

This chapter is an introduction. It familiarizes the reader with the general ideas that guided this research.

In the second chapter we give a description of the detector assembly and the running conditions. We describe in detail the working principle of the triggering system, straw tubes operation and other essential parts of the spectrometer. We provide the results of the studies of the straw tube operational regimes and the characteristic distributions of the other parts of the system. The counting curves of the Cerenkov counters and beam counters are also included.

The third chapter goes over the detector calibration procedures and the event reconstruction algorithm. There are three parts of the detector calibration. They are described in great detail. There are several branches of the event reconstruction. We explain how the event reconstruction works. We also show the Monte-Carlo simulations used to ensure the quality of the reconstruction. A brief description of the event output and the file structure of the analyzing package is included.

The subject of the forth chapter is the theoretical background for this research. We describe the features of the hard proton-proton scattering in the restricted kinematics of our detector. There is a discussion of the different processes contributing to the data sample.

Chapter five has a consistent picture of this analysis evolution. We plot the numerous distributions of the kinematic variables that are essential for our understanding of the event sample. We present a puzzling behavior of the $\frac{d\sigma}{dP_t^2}$ spectrum. It seems to exclude the easily

understood explanations of the process's nature. We speculate as to what the nature of the process could be that gives a rise to such unexpected distributions.

Conclusions and the summary of this research are given in Chapter six.

Chapter 2

Detector assembly and running conditions

Introduction

This chapter is devoted to the description of our EVA spectrometer. I took part in the preparation for the 1998 run for three years. During this period improvements in electronics, rigid structure of the straw tube chambers, studies of gas mixtures and efficiency of detector elements as well as many other projects were completed. The biggest concern was the performance of the EVA solenoid. This super-conducting magnet failed during the previous run in 1994. Eventually all the obstacles were cleared. We took data for six months starting June 1998. We will cover all of the improvements that were done and go over the running conditions of 1998 run.

2.1 Detector disposition

The EVA spectrometer (Figure 2.1) was assembled at BNL (Brookhaven National Laboratory), Long Island, New York. The EVA spectrometer was part of the experiment that

was running in 1994 and was modified and improved for the 1998 running period. It is positioned in the C1 line of the AGS (Alternating Gradient Synchrotron). The C1 line is

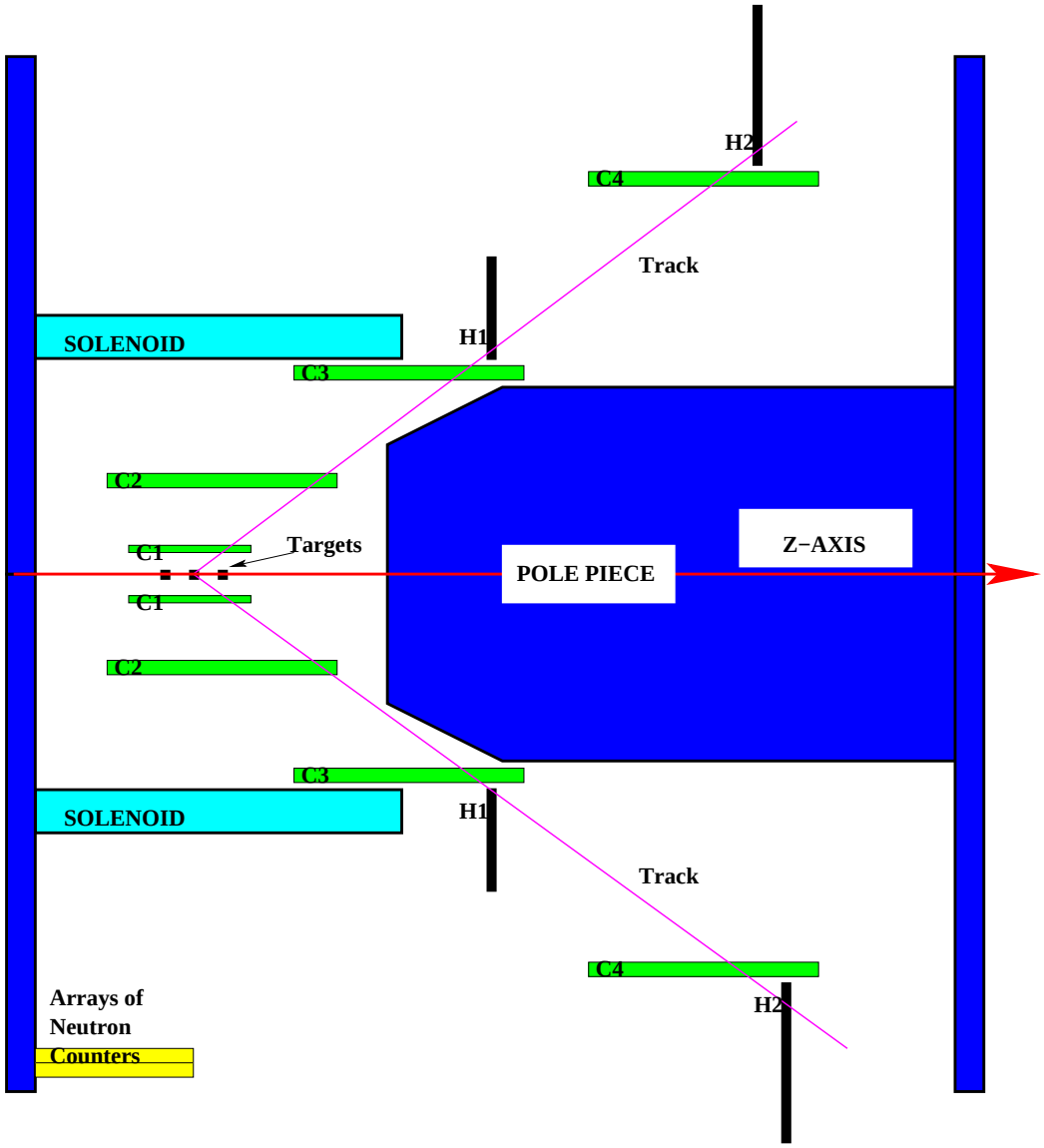

Figure 2.1: The schematic representation of the EVA-spectrometer. *RZ*-plane section. The dimensions are scaled.

transporting the beam of protons, produced in the secondary target. The energy of the primary beam is ~ 20 GeV. We use the secondary beam. The secondary beam is controlled by the magnets in the beam line. We set the energy of the secondary beam.

The energies that we used are 6, 8, 9, 11.7, 14.4 GeV. The beam only partially consists of protons. For example, a beam at 6 GeV has 49% protons, 50% pions and 1% kaons. This ratio changes as the energy increases. At 14 GeV we have almost 70% protons and 30% pions.

2.2 Detector assembly

2.2.1 EVA solenoid

A super-conducting magnet was installed as an integral part of the EVA spectrometer. It provides us with the ability to determine the transverse momenta of the charged particles passing through the detector. The super-conducting magnet was taken from the "CLEO" detector at the Cornell Electron Storage Ring. The solenoid was installed for the first running period of the spectrometer in 1994-1995. A detailed description of the structure and parameters of the magnet can be found elsewhere [21].

Being the most important part of the experimental apparatus, the solenoid was also the most troublesome. It failed at the end of the 1995 run and underwent very thorough checks during the preparation for the 1998 run. Due to the tremendous efforts of Alan Carroll (BNL,AGS), Alex Leksanov (PSU) and the cryo-support group from BNL the magnet was repaired, improved and was working with a very high stability. It was operating at 1200A current. This current produces a magnetic field of 0.8T in the center-field region. It creates a homogenous field along the Z-axis of the detector (solenoid axis). Several measurements of the magnetic field were performed. They were used for the calculations of the magnetic field in the whole volume (magnetic field simulation program, BNL). The calculations agreed

with the measurements with accuracy of $\sim 1\%$.

The map of the magnetic field was used in numerous Monte Carlo simulations that we ran for different purposes. As it will be seen in Section 3.2.3, one of the tasks for which we used Monte Carlo simulations was to determine the changes in the parameters of the track depending on the polar angle Θ of the track. We will explain the reason why such a dependence takes place.

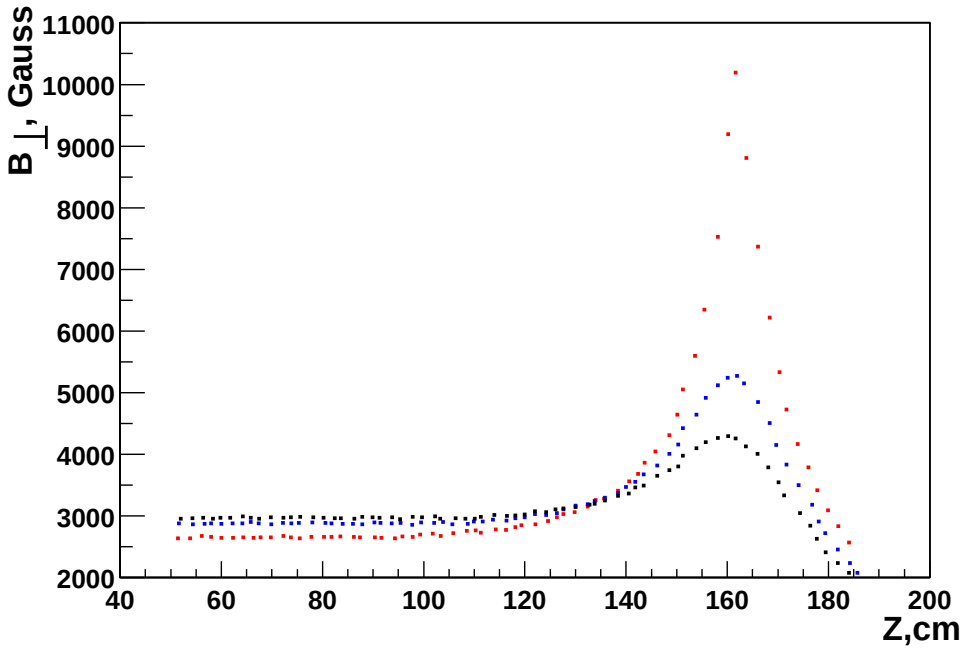

Figure 2.2: The perpendicular to the track component of the magnetic field for tracks with different θ angles.

One can see in Figure 2.2 the component of the field perpendicular to the track. When the Θ angle of the track becomes small, the track passes close to the pole piece. In red we plot the $B_\perp$ for a track that has the smallest θ angle. It passes at the smallest distance from the pole piece. The track that has the largest θ angle is drawn in black. It passes the farthest away from the pole piece. The pole piece starts at Z=157cm. In the region close

to the pole piece, the component of the magnetic field perpendicular to the track becomes very large. This effect takes place because the pole piece is collecting the magnetic flux and creates inhomogenity on it's very edge. The effect of the inhomogenity on the trajectory of the particle is described in Section 3.2.3.

2.2.2 Scintillating Hodoscopes and Level 1 trigger

Scintillating Hodoscopes are sets of fan-shaped counters that surround two (C3 and C4) of our chambers. There are two sets of counters with 256 individual detectors in each set. The sets were named H1 and H2. H1 is being hit first by particles coming out of the targets. H1 hodoscopes surround the C3 chamber. They are smaller then the H2 counters (surrounding C4) in all three dimensions. H2 hodoscopes surround the C4 chamber.

Both types of hodoscopes consist of organic scintillators and photo-multipliers. When a charged particle passes through an organic scintillator, it excites and ionizes the molecules of the scintillator. The excitation propagates inside the counter. De-excitation of the molecules takes place shortly thereafter. It produces the light (luminescence). The light propagates toward the photo-multiplier. In order to provide better light collection and eliminate noise from outside sources of light, the scitillator is covered by reflecting foil and dark tape. The process of the excitation, propagation and luminescence takes place in $1 - 10ns$.

The short reaction time allows us to use the hodoscopes in the trigger system for preliminary selection of the events. The geometrical structure of the sets of hodoscopes also serves this purpose. One can see in Figure 2.3 that each H2 hodoscope is overlapping with the adjacent elements. In some situations a particle can hit two adjacent counters. Effectively this structure enables us to have 768 detecting volumes instead of 256. The same approach

is not realized in the H1 counters. The layering of the hodoscopes increases multiple scattering and deteriorates the resolution in P_t. The H2 hodoscope is the last detecting part of the apparatus. We don't care what happens to the particle after it passes the H2 hodoscope.

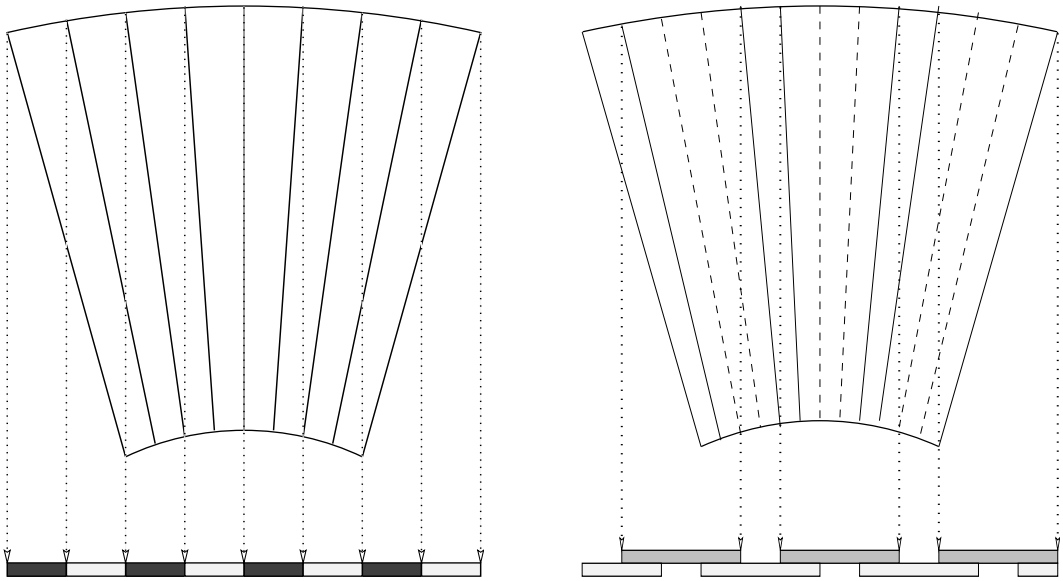

(a) The bins of the H1 hodoscope. The view in the plane and the section of the plane.

(b) The bins of the H2 hodoscope. The view in the plane and the section of the plane.

Figure 2.3: Examples of several bins of H1 and H2 hodoscopes.

One can see from Figure 2.3(b) the sandwich-like structure of the H2 system. It effectively (using electronics logic [22]) creates three times more fine grid in the azimuthal angle than the side-by-side scintillators. As we mentioned, the hodoscopes are part of the trigger system because of the very fast response time. They are included in the Level 1 trigger.

The Level 1 trigger is designed to select trajectories of particles with certain constraints on the momentum and charge of the particle. Because of the effect of the magnetic field on the trajectory of charged particles, the hits in H1 hodoscopes do not have the same azimuthal

angle as hits in H2 hodoscopes. The difference in the angles is related to the momentum of the particle in the transverse ($R\Phi$) plane. The smaller the transverse momentum the larger the difference between the Φ angle of the hit H1 element and the Φ angle of the hit H2 element. The momentum selection procedure of the Level 1 trigger is based on this property of the trajectory of the particle.

Using the Level 1 trigger we can require a certain $\Delta\Phi = \Phi_{H_1} - \Phi_{H_2}$ between the azimuthal angles of the hits in the hodoscopes. The trigger is more restrictive for a small $\Delta\Phi$. It selects the tracks with the large transverse momentum.

There are several levels that can be set in the Level 1 trigger. The gradation is in the logical bins of H2. The level of restriction corresponds to the number of logical bins of H2 by which the hit in H2 deviates from the hit in H1 [22]. In Figure 2.4 one can see the interpretation of the Level 1 trigger.

The blue regions signify by how many logical bins can the hit in H2 be away from the hit in H1 (red). The darker blue region corresponds to the trigger condition that is more restrictive on the P_t of the passing particle. This representation is shown for the positively charged particles. The same principle works for the negatively charged particles.

During the data aquisition with the positively charged beam, we opened the trigger on the right side and closed it on the left side. This setting eliminates the possibility to trigger on the negatively charged particles. For the runs taken with a negative beam we had both sides opened. We were accepting tracks that had P_t higher then a certain bounding value (running conditions in Section 2.3).

The semantics for the Level1 trigger is established in the following way. There are three letters A,B,C with corresponding numbers. For example, combination A1 means that

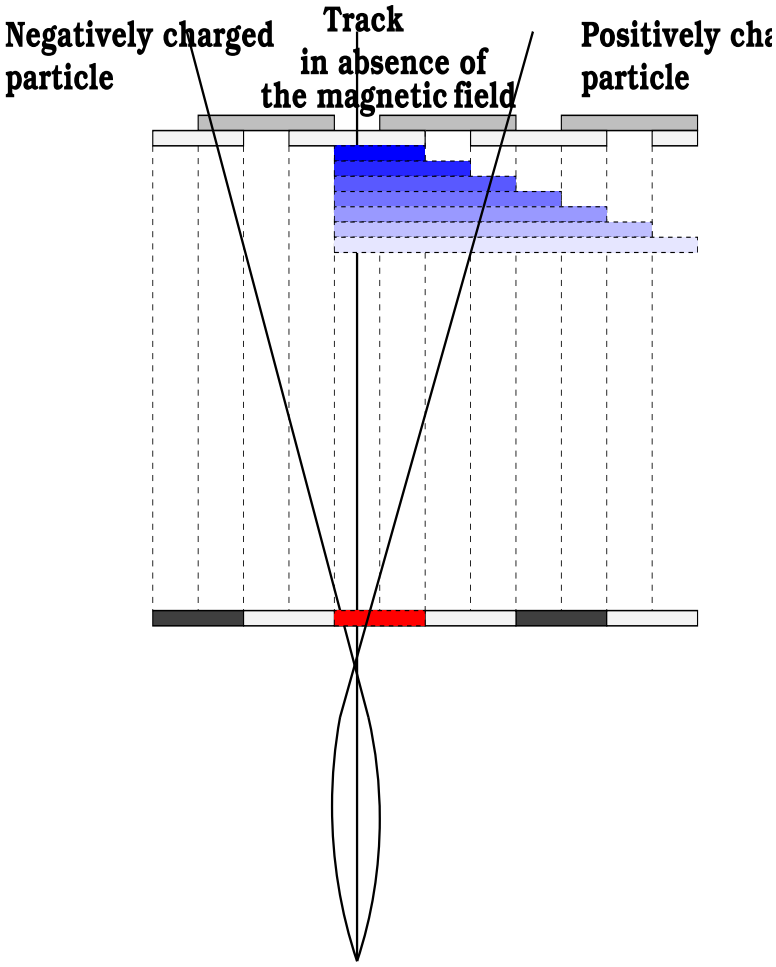

Figure 2.4: The schematic representation of the Level 1 trigger.

a track is allowed to deviate by 1 logical bin of H2 to the left side (negatively charged particle) from the hit in H1. Letter B is dedicated to the trigger effecting positively charged particles. Letter C serves as a veto for the particles that have a deviation of 0 logical bins in the hodoscopes. We represent a trigger condition as a sequence of letters and numbers.

A combination A3B3C1 was used for a negative beam of particles with 6 GeV energy. It means that the Level1 trigger is accepting both positively and negatively charged particles. The P_t of the particles has to be high enough so that the track deviates from a straight line by 3 or less logical bins of H2. Tracks with the deviation of 0 logical bins are accepted.

We use single and double settings for the Level1 trigger. Single Level1 requires the trigger condition to be satisfied for at least one particle. Double Level1 requires the trigger condition to be satisfied for at least two particles. The two particles have to be in different hemispheres.

2.2.3 Straw Tube Chambers

The Straw Tube Chambers [23] are the heart of the EVA detector. All the parameters of the tracks were reconstructed from the straw tube's signals. This information was used to calculate the physical variables (section 3.2).

The detector has four straw tube chambers. They are named C1,C2,C3 and C4. Each chamber has four layers of straw tubes. The tubes are arranged in cylinders. Each layer is shifted by $\frac{1}{2}$ tube radius in azimuthal direction with respect to the adjacent layers. We provide the parameters of the straw tubes in the table below (Table 2.1).

The straw tube is made of Aluminized Mylar. It is created by spirally rolling and gluing

Chamber Name	Chamber Radius	L_{tube}	R_{tube}	Tube's wall Thickness	Operating Voltage	N_{tubes}	$N_{sectors}$	TDC avail.	ADC avail.
C1	10cm	100cm	.25cm	.0012	1500V	512	4	YES	NO
C2	44cm	200cm	.5cm	.0025	1900V	1024	8	YES	YES
C3	98cm	200cm	.5cm	.0025	1900V	2048	16	YES	YES
C2	178cm	200cm	1cm	.005	2000V	2048	32	YES	YES

Table 2.1: Table of straw tube dimensions and other parameters.

a Mylar strip on a rod of the appropriate diameter. The straw tube has a high voltage wire running through the center of the tube. The surface of the aluminized mylar is grounded.

Straw tubes work on a mixture of 50% Argon (Ar) and 50% Ethane (C_2H_6) gases. Each sector has it's own gas supply line and a gas flow monitoring station. The choice of the gas mixture is based on the studies of the straw tube performance [24].

Let us briefly describe how the straw tube works. The straw tube produces a current pulse after a charged particle passes through. The current pulse is formed in the follwoing way.

A charged particle ionizes the molecules of Argon. Electrons and ions move toward the wire and the walls under the influence of the electric field. In the close vicinity of the wire electrons are accelerated in the fast increasing electric field. They ionize more Argon molecules and produce a mini-shower moving toward the wire [25, 26]. The Ethane molecules serve as a quencher. They have many rotational and vibrational degrees of freedom and can absorb the energy from the excited Argon molecules. The quencher helps to stop the secondary showers and discharges in the straw tubes.

The current signal, produced by a charged particle, propagates along the resistive wire. On both ends of the tube it is collected by the electronics. In Figure 2.5 we provide the routing of the signals. As the signal reaches the ends of the wire it is directed through the

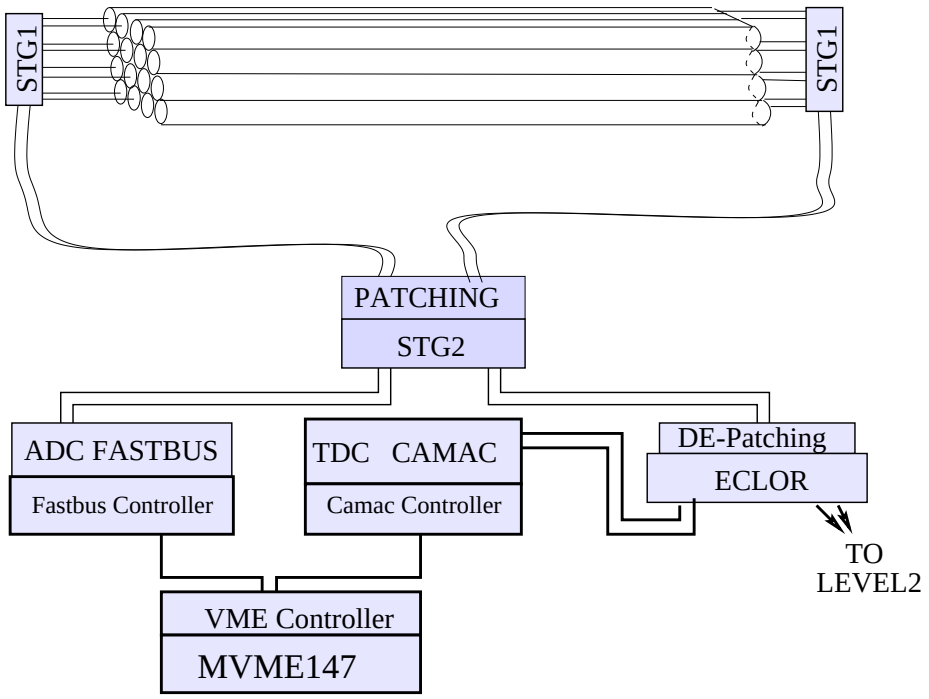

Figure 2.5: The routing of the signal through the straw tube electronics.

STG1 cards. These cards have pre-amplifiers for every tube. From the STG1 the signals travel over the long coaxial ribbon cables to the STG2 cards. The STG2 cards amplify the signals and direct them to the ADC FASTBUS and the TDC CAMAC.

The ADC is an analog-to-digital convereter board. It converts the analog pulse into the integral of the pulse. It's output is the total charge collected from a tube. We have 16 bit ADC boards. The ADCs are used to determine the position of the hit in the tube along the wire (Figure 2.6). A detailed description is given in Section 3.1.2.

The TDC is a time-to-digital converter board. Its output is the time passed between arrival of the straw tube signal and the trigger signal. We have 10 bit TDC boards. It allows us to measure time intervals up to 512 ns. The TDC signals are used to determine the distance from the track to the wire - drift distance (Figure 2.7). A detailed description

is given in Section 3.1.1.

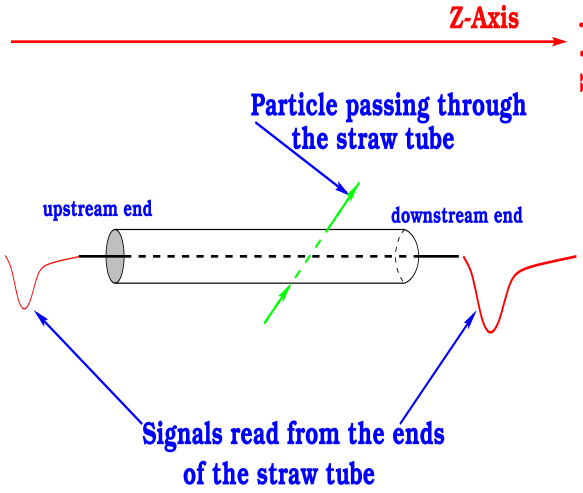

Figure 2.6: Particle passing through the tube. XY-plane section.

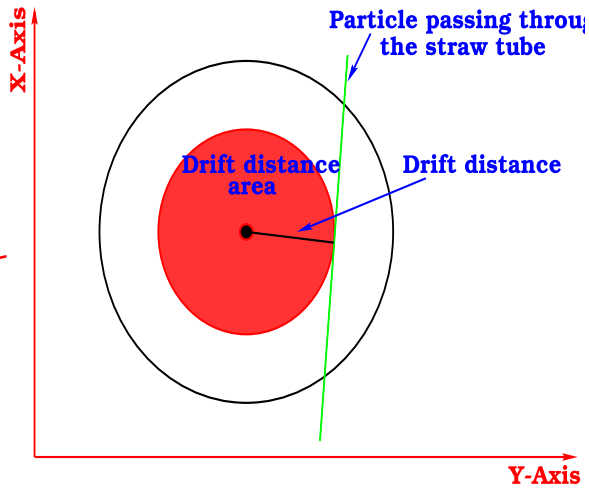

Figure 2.7: Particle passing through the tube. RZ-plane section.

We have a total of 5632 TDC channels and 1280 ADC channels. The number of ADC channels is smaller because of the high cost of the ADC boards. Signals from eight straw tubes are combined in one ADC channel. The eight tubes are chosen in such way that the probability of having a hit in more then one of those eight tubes is the smallest [27]. The TDC signals from the two ends of the tube are of the same value. They are logically summed.

During the data analysis we found a mistake in the wire connections for some sectors of C1. We fixed it by modifying the database EVA_CONST.rz. It is described in detail in Appendix A.

2.2.3.1 Level 2 trigger

The tubes of chambers 2,3 and 4 are part of the Level2 trigger. The Level2 trigger is designed for P_t selection. It makes more accurate decisions than the preliminary P_t selection of the

Level1 trigger (section 2.2.2).

We describe below how the Level2 trigger works. The information from the two inner layers of the straw tubes is directed to the Level2 trigger boards (Figure 2.5). There are 32 trigger boards. Each board carries eight custom designed TEVA chips [28]. A single TEVA chip is covers $\frac{1}{256}$ of the 2π azimuthal angle. It corresponds to 8 tubes in rows two and three of C3. The TEVA chips have the ability to communicate with the adjacent chips. The goal of the Level 2 trigger is to look for hits in the chambers that satisfy a certain map. This RAM map is loaded by the software. It determines the tightness of the transverse momentum cut (Figure 2.8).

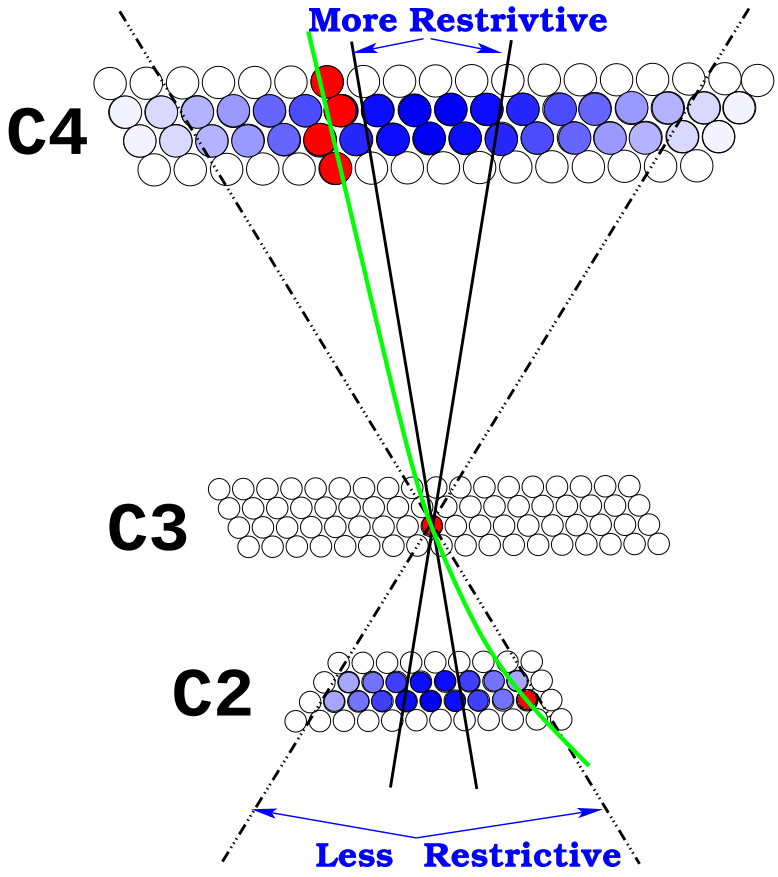

Figure 2.8: An example of the selectivity of the Level 2 trigger.

In Figure 2.8 we present an example of the cuts by the Level2 trigger. The depth of the blue color signifies the tightness of the cut. A more restrictive trigger accepts only the particles that pass between the black solid lines. A trigger condition that accepts the particles with smaller P_t embraces the lighter color of blue. The green line is an example of a track. The particle hits several tubes. They are depictured as red circles. One can see that this track would not pass a more restrictive trigger cut.

We used a set of tag names to describe the strength of the trigger.

Trigger name	P_t allowed	Trigger name	P_t allowed
T2Early	$\geq$ .73GeV	T2even	$\geq$1.21GeV
T2Easy	$\geq$.85GeV	T2evil	$\geq$1.33GeV
T2Enjoy	$\geq$.97GeV	T2Exact	$\geq$1.58GeV

Table 2.2: Table of trigger conditions.

The Level2 trigger can be set as single and double. A single Level2 trigger requires at least one particle to satisfy the condition on P_t. A double Level2 trigger requires at least two particles to satisfy the condition on P_t.

The settings of the Level 2 trigger that we used during the 1998 run are tabulated in Section 2.3.

2.2.3.2 Rigidity improvements

We completed several improvements to the rigidity of the straw tube chambers in preparation for the 1998 run.

The straw tubes were made in 1993. Over several years the wires and the walls of the tubes deformed. The tubes of the C2 and C3 chambers were sagging on the old chamber frames. The old frames were made of carbon based endplates and support pipes. New

aluminum endplates and aluminum support pipes were made and installed. They greatly improved the rigidity of the chambers. However, the individual sectors were still showing the signs of sagging.

We designed and installed an additional support structure. It was based on a thin rohacell ring fastened to the support pipes. Each sector had a rohacell attachment glued to the outter layer. We connected the ring and the sector attachments with special non-magnetic adjustable bolts. The bolts were made in such a way that we could move a sector with respect to the rohacell ring.

Rohacell was the optimal choice based on a combination of several factors. It was not a significant source of multiple scattering. It was very light and easy to machine. It had a relatively good expansion factor under humidity changes. It almost does not expand.

We installed the rohacell ring for C2 on the outside and for C3 on the inside of the chamber.

2.2.3.3 Gas mixture and Efficiency studies

We studied the gas mixture and the tube efficiency during the preparation for the 1998 run. The objective of the studies was to determine the best conditions for operating the straw tubes. We used a ^{106}Ru (Ruthenium) source for the studies. The ^{106}Ru undergoes β decay. The energy of the e^- is 6.55 MeV. A special unit was assembled to study the signals from the straw tubes. There were two different techniques.

In one case we have chosen four tubes positioned in the way of the emmitted e^-. Three of the tubes served as a trigger (Figure 2.9). We sent the signals through discriminators and shapers. The coincidence unit logically added the step-shapped signals (Figure 2.10).

The output was a number of the tripple coincidences from the trigger and a number of the quadrupole coincidences from the set of four tubes. The efficiency of tube 4 was calculated

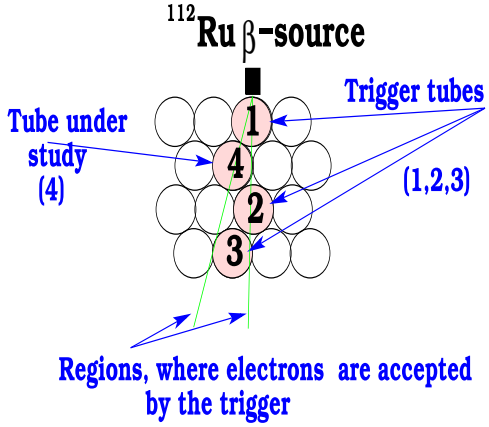

Figure 2.9: Efficiency studies. Tubes setup. Case 1.

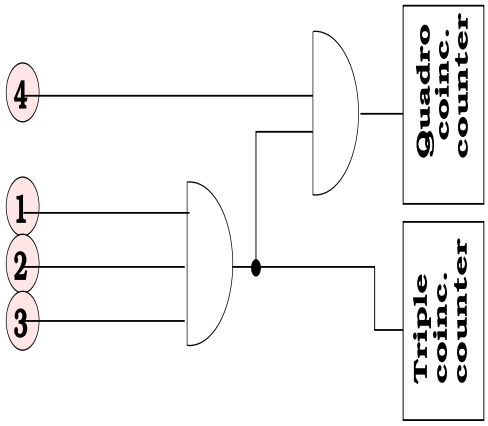

Figure 2.10: Efficiency studies. Electronics setup. Case 1.

using equation 2.1.

$$\epsilon_4 = \frac{N_{quadr.coinc.}}{N_{triplecoinc.}} \tag{2.1}$$

In the second case we have chosen five tubes that are in the way of the e^-. Two of the tubes were used as a trigger (Figure 2.11). The efficiency of the other three tubes was studied. It was an analog to studying the efficiency of the layer of tubes. As in the first case, the signals were processed by the discriminators and shapers. The logic unit was different (Figure 2.12) than in the previous case.

We calculated the efficiency of the layer of three tubes using equation 2.2.

$$\epsilon_{layer} = \frac{N_{triplecoinc.}}{N_{doublecoinc.}} \tag{2.2}$$

We performed a study of the background of accidental double and triple coincidences. It was done using the method of the curve of the accidental coincidences. We chose two

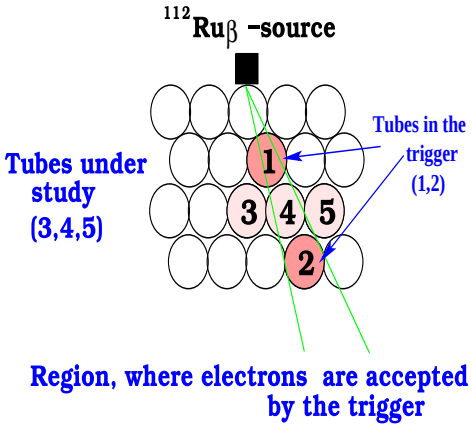

Figure 2.11: Efficiency studies. Tubes setup. Case 2.

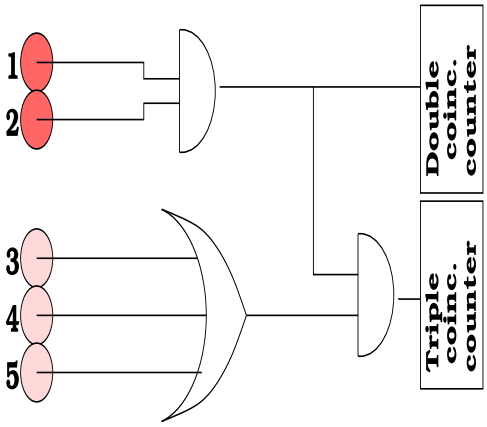

Figure 2.12: Efficiency studies. Electronics setup. Case 2.

trigger tubes. For these tubes we measured the dependece of the number of coincidences on the delay between signals from the tubes (Figure 2.13).

When the delay is smaller than the length of the signal, we count both real and accidental coincidences. As the delay became longer than the length of the signal, there are only the accidental coincidences left. The estimates of the accidental coincidents are used in the calculations of the tubes efficiencies.

The efficiency of the straw tubes depends on the operating voltage. We determined the high voltage region which is optimal for straw tubes. We measured the dependence of the number of counts in the straw tube on the applied voltage (Figures 2.14,2.15).

Properly operated straw tubes should have a 'plateau' on the 'counts versus voltage' dependence curve. 'Plateau' is a special high voltage region. In this region the number of counts in the straw tube does not depend on the applied high voltage.

One can see in Figure 2.15 the dependence of this characteristic on the mixture of the gas in the straw tube of C3. The larger fraction of Argon leads to the longer 'plateau'. It allows one to operate the tubes at a lower voltage, farther from the breakdown voltage,

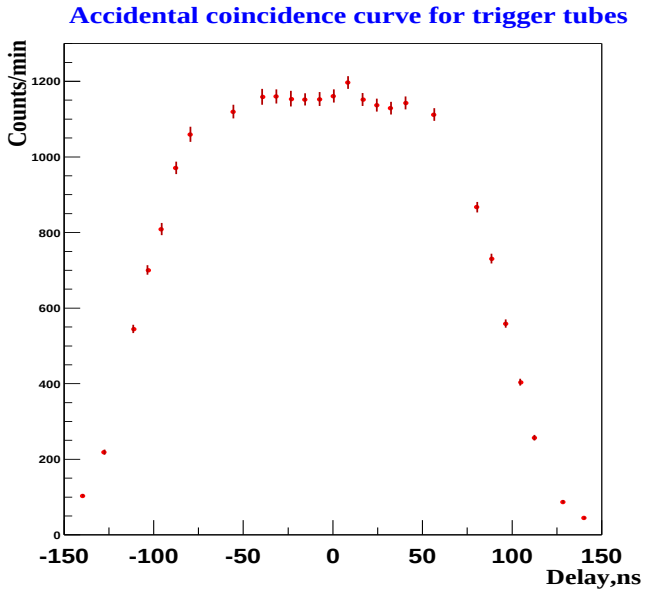

Figure 2.13: The curve of the accidental coincidences.

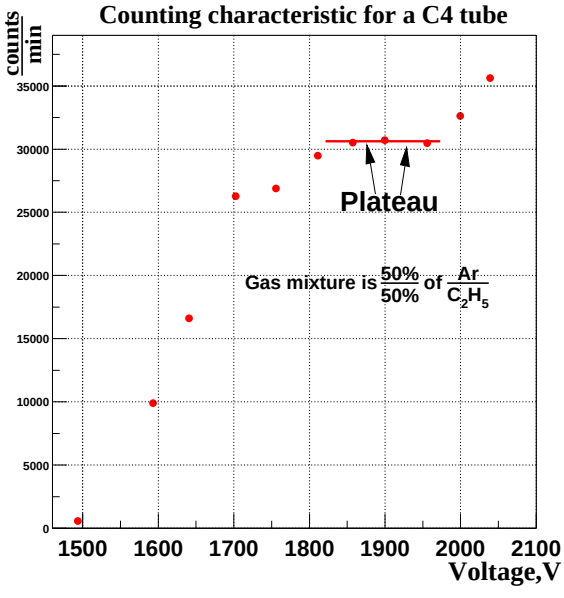

Figure 2.14: The counting characteristic of a C4 tube.

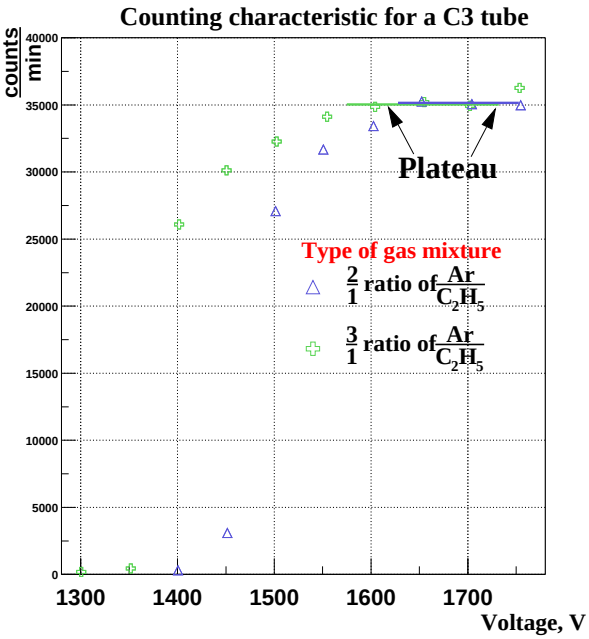

Figure 2.15: The counting characteristic of a C3 tube.

without loss in the efficiency of the tube.

A higher fraction of Argon in the gas mixture leads to a larger amplitude of the signal. There is a limit on the amount of charge an ADC can collect without overflow. ADC overflow does not allow to determine the Z-position of the hit. To make sure that the straw tubes do not operate in the regime of a large number of overflows, we studied the dependence of the amplitude of the signal on the gas mixture.

The amplitude was measured using the ^{55}Fe source. It decays via electron capture into ^{54}Mn (stable). The energy of the produced γ is 5.9 keV. The amplitude dependence is given in Figure 2.16. It is plotted as a function of the breakdown voltage fraction for two gas mixtures.

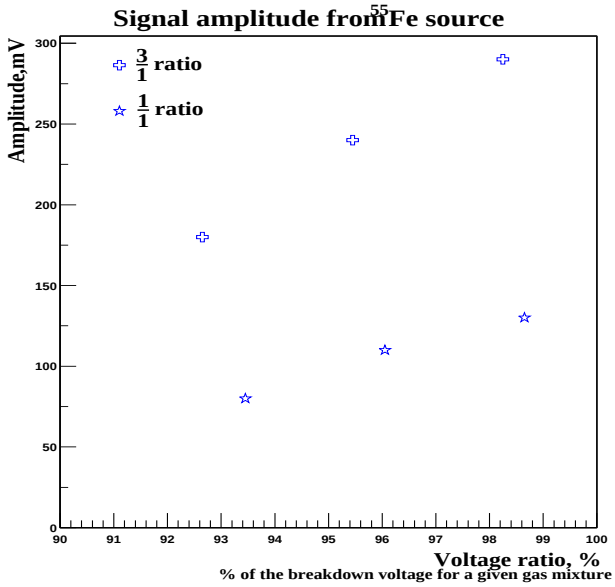

Figure 2.16: The dependence of the amplitude of the signal in a tube of the C3 chamber on voltage. The data is for a $\frac{3}{1}$ and $\frac{1}{1}$ ratio of $\frac{Ar}{C_2H_6}$ gas mixtures.

For an optimized operation of the straw tubes we used the $\frac{1}{1}$ mixture of $\frac{Argon}{Ethane}$.

2.2.4 Targets

A carbon target was chosen to study the effects of the particle's interactions in the nucleus. For calibrating and for normalization purposes we used the hydrogen nucleus. The hydrogen nucleus is contained in the CH_2 target. We extracted the hydrogen signal by subtracting the carbon signal from the CH_2 signal. We used different combinations of the C and CH_2 targets (Section 2.3).

For the ADC calibrations, as described in Section 3.1.2, we used a very small Cu target. It was small in order to provide a point like target. Then the tracks used in calibrations are coming from one point at a very well defined position.

At high energies we used only one C or CH_2 target. An additional Al target was used for beam normalization. It was positioned in front of the main target. The distance between them was large enough for good target resolution.

The dimensions of the targets are provided in Table 2.3. For high energies we combined the two targets in one. For example, we used $13.2cm$ long target for 11GeV.

Target	Symbol	Length	Width	Height	Density
Carbon	C	$6.6cm$	$5cm$	$5cm$	2.43 g/cm^3
CH_2	CH_2	$6.6cm$	$5cm$	$5cm$	0.96 g/cm^3
Aluminum	Al	$.5cm$	$5cm$	$5cm$	2.70 g/cm^3
Copper	Cu	$1cm$	$1cm$	$1cm$	8.96 g/cm^3

Table 2.3: The table of the parameters for the targets.

A complete list of the target combinations is provided in section 2.3.

2.2.5 Beam Hodoscopes

Beam Hodoscope is a set of scintillating fibers positioned in the way of the beam, before the target. It serves as a beam counter. It is included in the trigger system. Signals from the Beam Hodoscope (BHod) determine the time when particles enter the targets. We use the information from the BHod for beam normalization in the offline analysis.

The Original BHod has a set of 23 vertical and 48 horizontal scinitillating fibers. The width of each fiber is 2mm. Overlapping horizontal and vertical scintillators produce $2.5 \times 5cm$ active area. The Beam Hodoscope is designed to handle beam rates of $\sim 10^8$ particles per spill.

An Additional Beam Hodoscope (THod) is installed $1.5m$ upstream from the BHod. THod has two vertical and two horizontal scintillating fibers of $\sim 1cm$ width. Each fiber has a very fast photo-multiplier attached to each end. The response time of the additional beam hodoscope is $1 - 3ns$. The THod is designed to handle beam rates up to $\sim 10^9$ particles per spill. This hodoscope is also included in the trigger and is used for beam normalization in the off-line analysis. The schematic pictures of both hodoscopes are in Figure 2.17.

The counting characteristic of the hodoscopes is given in Figure 2.18. It is plotted as a function of the counts in the Ion Chamber. The Ion Chamber is used to monitor the beam. It is positioned right after the THod. The dependence of the counts in the Ion Chamber on the beam intensity is provided in Figure 2.19.

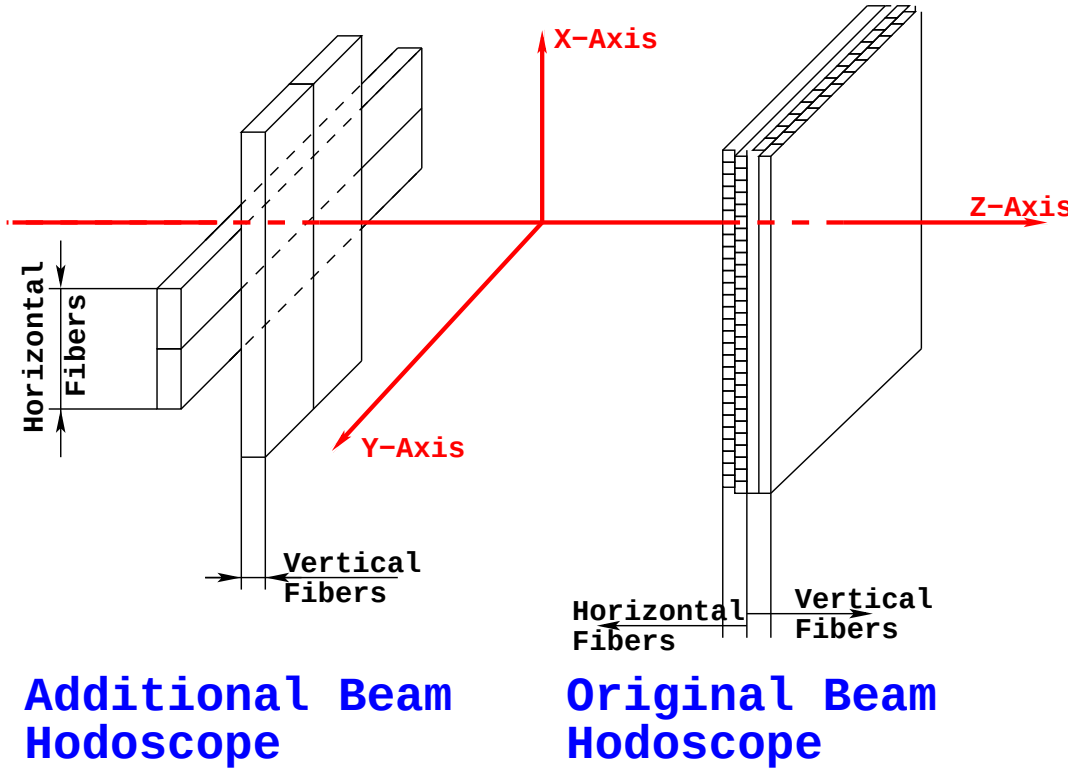

Figure 2.17: The schematic picture of the Original and Additional Beam Hodoscopes.

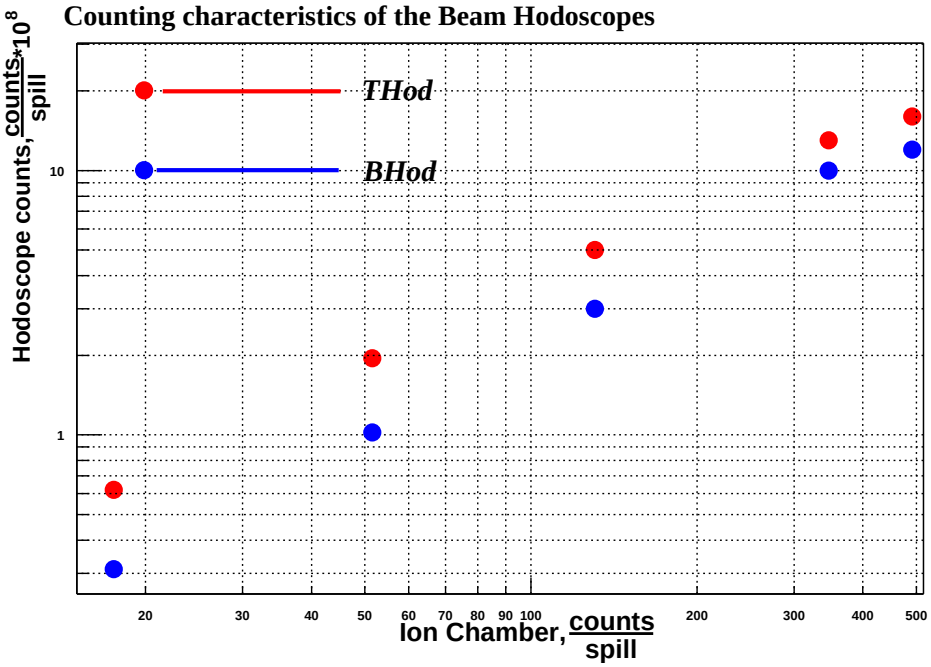

Figure 2.18: The counting characteristic of the THod and BHod.

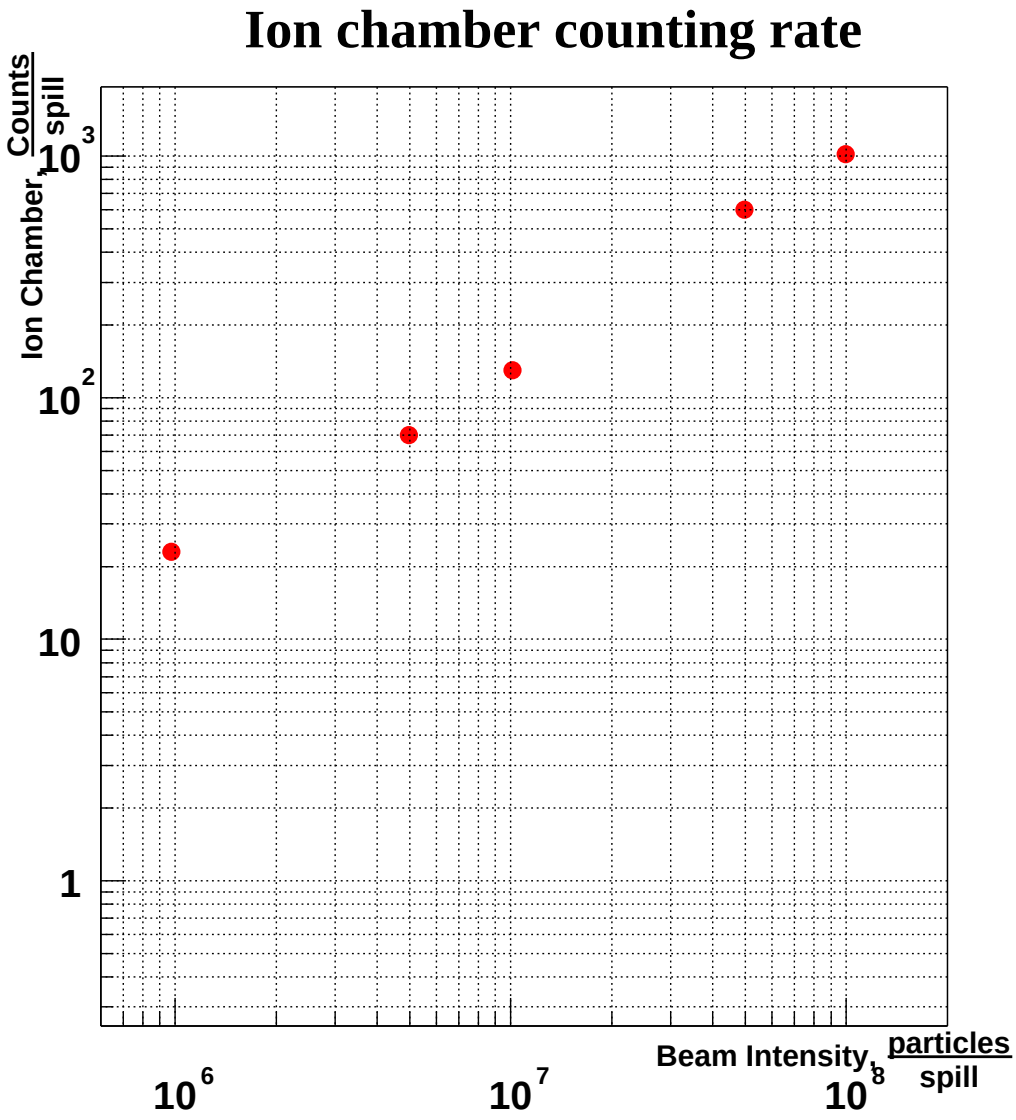

Figure 2.19: The counting characteristic of the Ion Chamber.

2.2.6 *Čerenkov* counters

We use two *Čerenkov* counters to determine the type of beam particles interacting in our targets. One of the counters is set up to detect protons. Another one is for tagging pions. Each counter has six photo-multipliers forming a light detecting ring on the upstream endcap and a spherical mirror on the downstream endcap (Figure 2.20). The ring and the mirror are centered around the beam axis.

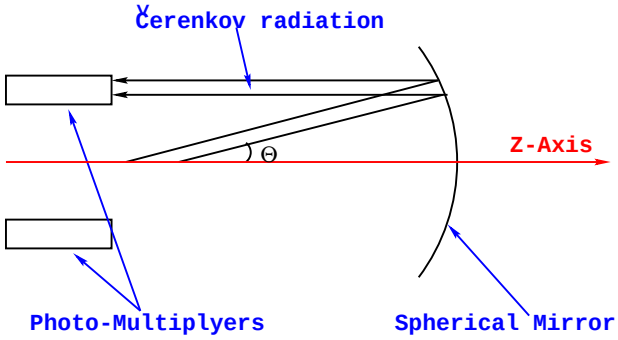

Figure 2.20: The schematic picture of the *Čerenkov* counter.

The beam particles produce *Čerenkov* radiation when passing through the CO_2 gas inside the counters. The radiation propagates along the cone with an opening angle Θ. This angle is determined by the coefficient of refraction of the gas n and the speed v (or $\beta = \frac{v}{c}$) of the particle [25].

$$cos(\Theta) = \frac{1}{\beta n} \tag{2.3}$$

The available range of angles is constrained by the geometry of the *Čerenkov* counters. Radiation is detected when it is emitted in the range $4.8° - 8°$. The protons and the pions in the beam have different β. To insure that the *Čerenkov* radiation is emitted in the correct angular region (Eq. 2.3), the coefficient of refraction is set seperately for each counter. It is done by varying the gas pressure. The gas pressure is different for every beam energy

because β of the beam particle changes with energy. Dependence of the number of counts in the $\check{C}erenkov$ counter on the pressure of the gas was checked for every new set up (Figure 2.21).

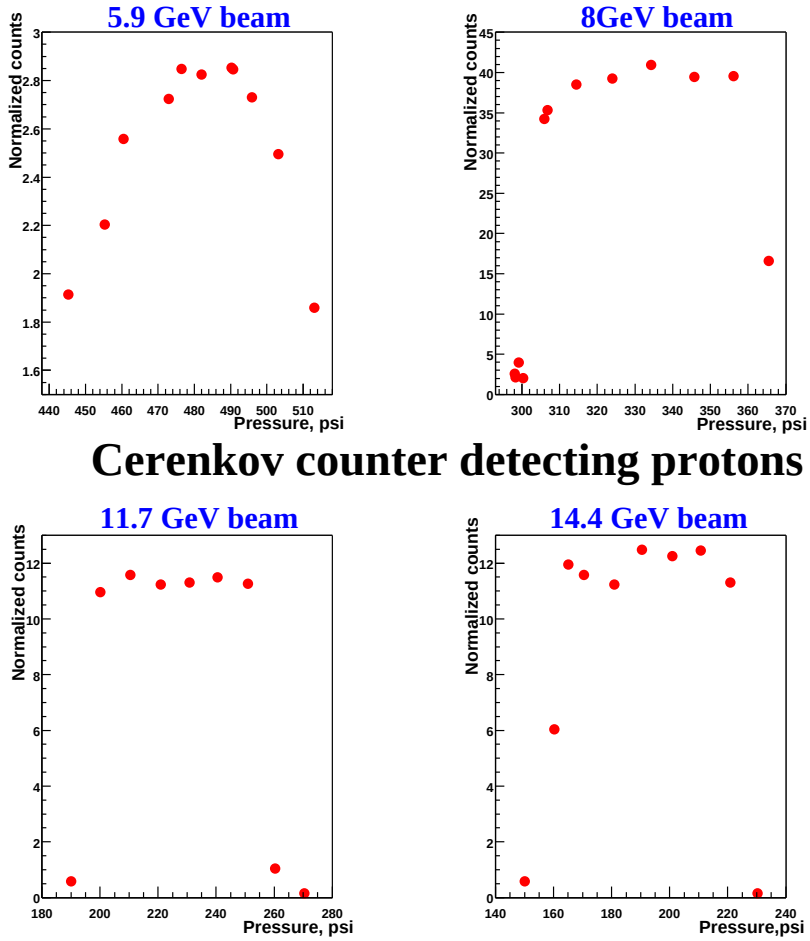

Figure 2.21: The Pressure Curves for the $\check{C}erenkov$ counter at different beam energies. The counter is set up to detect protons.

2.2.7 Scintillating $'noodle'$ counters

A set of four scintillating fibers ($'noodles'$) with photo-multiplyers is used for detector calibration (section 3.1.2) in the RZ plane. Each $'noodle'$ is $1.5cm$ wide , $.5cm$ thick and

320cm long. We wrap the $'noodles'$ around the outter chamber (C4) like a belt (Figure 2.22).

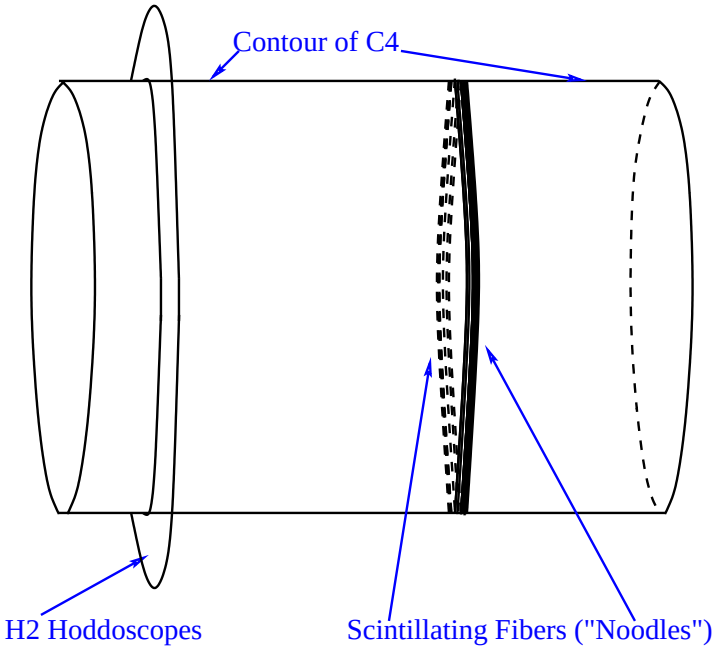

Figure 2.22: The schematic picture of the $'noodle'$ counter.

For the special magnet-off calibration runs, the trigger is set to accept events with a coincidence of H1,H2 and one of the $'noodles'$. This condition determines a straight track coming from the target and passing through the $'noodle'$. Because of the small thickness and width of the fibers, we obtained good spatial information about the points where particles pass through C4.

2.2.8 Data Aquisition System

The Data Aquisition System (DAQ) is split into three parts. User starts data collection via program that is called ZPROG. It is running on a Silicon Graphics computer, located in the counting house. ZPROG was written for the 1994 run and has the capabilities of

running data collection as well as several types of chambers diagnostics. We use ZPROG for data collection and for ONLINE diagnostics of the chambers breakdowns and malfunctioning electronics. After ZPROG is started, it sends a set of commands to the MVME147 computer. MVME147 is located in the experimental hall. It is set up as a DAQ server and collects data from the CAMAC and FASTBUS controllers at the end of every event. The CAMAC and FASTBUS controllers read digitized signals from the CAMAC TDCs and the FASTBUS ADCs.

Because of the significant magnetic field created by the EVA solenoid we are not able to store the data on the MVME147 computer. It's memory buffer can hold only several events. Data is piped over the ethernet cable to the Silicon Graphics computer. There it is stored on the hard drive. It is later recorded onto the 8mm tapes.

2.3 Running Conditions

In this section we provide a table of the main parameters of the different data sets. We explain the meaning of the columns in the table.

The first column contains the energy of the beam for a set of runs. The range of the run-numbers for every set is given in the second column.

The third column has the conditions of the Level1 and Level2 triggers. Level1 trigger is shown first. A number in front of the trigger condition means that the trigger was double if it is II and single in case it is I. A description of the trigger conditions is given in sections 2.2.2 and 2.2.3.1.

The fourth column is for target configurations. If the two targets were combined to form

one long target, we denote it by brackets. For example, (CC) stands for two 6.6cm long targets joined to give one 13.2cm long carbon target.

The positions of the targets are in the fifth column. Their order corresponds to the order of the targets in the previous column. Positions are measured at the middle of the target.

The last column has the numbers of the tapes, on which the data files are stored.

Energy	Run Numbers	Trigger	Target Configurations	Target positions	Tapes
6GeV	8310-8524	II A0B3C1,I T2Early	CH_2	+10	7,11
		II A0B3C1,I T2Early	CH_2	-11	7,8
		II A0B3C1,I T2Early	C C CH_2	-35 -10 +12	8,9,10,12
		II A0B3C1,I T2Early	C CH_2 C	-35 -10 +12	8,9,10,12
		II A0B3C1,I T2Early	C C C	-35 -10 +12	8,9,10,11,12,13
		II A0B3C1	CH_2	+10	11
		II A0B3C1,I T2Early	C C C	-45 -22 0	13,14
		II A0B3C1,I T2Early	C C C	-55 -32 -10.5	14
9GeV	8536-8643	II A0B2C1,I T2Even	CH_2 C	-8.4 -34.4	15
		II A0B3C1,I T2Even	CH_2 C	-8.4 -34.4	15,16,17
		II A0B3C1,I T2Even	C CH_2	-8.4 -34.4	17
		II A0B3C1,I T2Even	Al C CH_2	-47 -27 -5	17,18,19,20
		II A0B3C1,I T2Even	Al CH_2 C	-47 -27 -5	17,18,19,20
6GeV Negative Beam	8669-8745	II A3B3C1,I T2Early	C CH_2 CH_2	-35 -10 +12	21
		II A3B3C1,I T2Early	Al C CH_2	-35 -10 +12	21,22,23,24,25,26
		II A3B3C1,I T2Early	Al CH_2 C	-35 -10 +12	22,23,24,25,26
		II A3B3C1,I T2Early	CH_2	-5	24
8GeV	8755-8782	II A0B2C1,I T2Early	(CH_2CH_2)	-6.6	26
		II A0B2C1,I T2Even	Two targets		26
		II A0B2C1,I T2Exact	combined into		26
		II A0B2C1,I T2Evil	one 13.2 cm long		26
6GeV	8791-8844	II A0B3C1,I T2Early	C C CH_2	-35 -10 +12	27,28,29
		II A0B3C1,I T2Early	C CH_2 C	-35 -10 +12	27,28,29
		II A0B3C1,I T2Early	C C C	-35 -10 +12	27,28,29
		II A0B3C1,I T2Early	C C C	-40 -18 +7	29
8GeV	8899-8905	II A0B1C1,I T2Evil	Al (CH_2CH_2)	-31 -6.6	31
		II A0B2C1,I T2Evil	Al (CC)	-31 -6.6	32
		II A0B1C1,I T2Evil	Al (CH_2CH_2)	-45 -6.6	32
		II A0B2C1,I T2Evil	Al (CC)	-45 -6.6	32
14.4GeV	8909-8942	II A0B1C1,I T2Evil	(CH_2CH_2) Al	-45 0	32
		II A0B2C1,I T2Evil	(CC) Al	-58.5 -10	32,33,34,35
		II A0B1C1,I T2Evil	(CH_2CH_2) Al	-58.5 -10	32,33,34,35
11.7GeV	8944-8973	II A0B1C1,I T2Evil	(CH_2CH_2) Al	-45 -10	35,36,37
		II A0B2C1,I T2Evil	(CC) Al	-45 -10	35,36,37
8GeV	8974-8976	II A0B1C1,I T2Evil	Al (CH_2CH_2)	-45 -6.6	37,38
		II A0B2C1,I T2Evil	Al (CC)	-45 -6.6	38

Table 2.4: The table of the running conditions for 1998 E850 run.

Chapter 3

Detector Calibration and Event Reconstruction

Introduction

In this chapter we describe the calibration of the EVA detector and the event reconstruction procedures.

We use the spacial coordinates of the hits in the detector for event reconstruction. As described in Chapter 2, the detector has a cylindrical symmetry. In the analysis, the trajectories of the particles are projected onto the $R\Phi$ and the RZ planes. The EVA spectrometer has separate electronics for collecting the spatial information in these two projections.

In the $R\Phi$ plane we calculate the transverse momentum of the particles. We use the distances from the tracks to the tube's wires for these calculations. The distances are calculated from the TDC signals (Section 2.2.3). The transverse momentum enters the calculations of almost all the physical variables found indirectly in our analysis. It is important to have a small error in the measurement of the transverse momentum. Thus, we need good TDC

calibrations. In Section 3.1.1 we will familiarize the reader with the calibration parameters and the methods used for TDC calibrations.

In the *RZ* plane we calculate the Θ angle (the polar angle) of the reconstructed tracks. The Θ angle is calculated in a fit over all the *RZ* plane coordinates of the hits in the straw tubes that belong to the trajectory of a particle. The Z-coordinates are calculated from the positions of the hits along the wire of the straw tubes. We extract the positions using the ADC signals (Section 2.2.3). We achieve a better angular and target position resolutions by decreasing the errors in the Z-coordinates. We explain the calculation of the Z-coordinates in Section 3.1.2. It covers several methods of the ADC calibration that we implement.

The TDCs and ADCs are calibrated for every straw tube. We combine the tubes into the groups of tubes to form a track. We use the coordinates of the tubes relative to each other for this procedure. Calibration of the the relative positions of the straw tubes is the main goal of the detector alignment process. It is covered in Section 3.1.3.

In Section 3.2 we describe the event reconstruction. Event reconstruction is the most important part of the analysis. The parameters of the reconstructed tracks are used for the detector alignment (section 3.1.3) and in the calibration process (section 3.1.2.2 and 3.1.2.3).

An event is formed in the program called *WZOFF*. *WZOFF* controls the reconstruction from reading the Raw-Data and until the output is created. The output format can be chosen by users.

The *WZOFF* first reads the raw information from the data file. The raw information is decoded and stored as blocks of information. Then, preliminary tracks are formed in the hodoscopes. The separate tubes are united into the bunches of tubes. The bunches are

united into the tracks.

After the tracks are formed, the reconstruction for every single track takes place. The parameters $P_t, \Phi, \Theta, Z_{vertex}$ are calculated. The parameters are used to calculate the global variables of the event such as 3D-Vertex coordinates, missing energy and missing momentum. This information is written out in several user-defined ways.

Section 3.2 covers the steps of the track formation, calculation of the parameters of the trajectories and the information output.

3.1 Detector Calibration

3.1.1 TDC calibration

In this section we describe the TDC calibration parameters and the calibration procedure.

The TDCs operates with signals from the straw tubes. A straw tube is a tube with an aluminized mylar wall. The tube has a wire in the center (section 2.2.3), which is connected to a positive high voltage source.

When a charged particle passes through the straw tube, the electrons and ions are created in the process of gas ionization. The products of the ionization drift in the electric field toward the wire and the wall. This motion creates a current pulse. The pulse travels along the resistive wire. It is collected by the electronics at the ends of the straw tube.

The drift time depends on the distance from the wire to the trajectory of the charged particle. The electrons produced near the wall of the straw tube travel for the longest time and the electrons produced near the wire of the straw tube have the shortest drift time. The other trajectories have drift times between these limits. The time when the particle

passes through the straw tube is measured relative to the trigger signal.

The drift velocity of the electrons is a constant, to a good approximation, along the radius of the straw tubes. We use this approximation to calculate the point of the closest approach of the charged particle's trajectory to the straw tube's wire (Equation 3.1).

$$DD = R_{tube}\frac{T_{signal} - T_0}{T_1 - T_0} \tag{3.1}$$

Here R_{tube} is the radius of the straw tube and T_{signal} is the time when the signal is collected by the electronics. T_1 is the smallest of all T_{signal}. It corresponds to the trajectory of the particle near the wall of the straw tube. T_0 is the largest of all T_{signal}. It corresponds to the trajectory of the particle near the wire of the straw tube.

T_1 and T_0 are the two calibration parameters. We calculate them for every straw tube. These parameters determine the edges of the timing distributions (Figure 3.1) for the straw tubes. Any charged particle that hits the tube has a T_{signal} between T_0 and T_1. These calibration parameters vary from tube to tube because of the slight differences in the length of connecting wires, internal parameters of the TDCs and other electronics for every channel.

To determine the calibration parameters T_0 and T_1, we collect the signals from the straw tube. We do not impose any restrictions on the tracks. The tracks pass through the straw tube at random distances from the wire. The result is a distribution of T_{signal} - time differences between the end of the event and the time when the signal reaches the straw tube's electronics. The T_{signal} distribution has a rectangular form (Figure 3.1) for a good tube.

The T_{signal} is plotted on the X-axis of Figure 3.1. The 10-bit TDCs have a time range of 512 ns. One can see (Figure 3.1) that T_0 is larger then T_1. This is because of the specifics

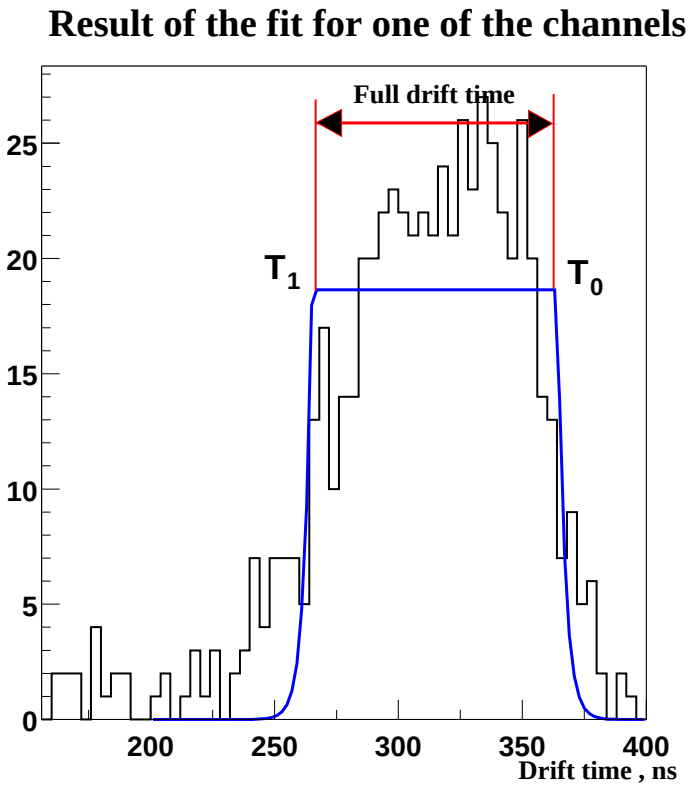

Figure 3.1: The fit of the TDC distribution for one channel.

of the trigger. We use 'common stop technique' in the trigger. We calculate the time of the signals from the end of the event backwards. Hits with the small drift times are farther away from the end of the event. Thus T_0 is larger then T_1. The smaller T_{signal} means that the particle passes farther away from the tube's wire.

The TDC calibration is repeated on a run by run basis to account for the time dependence in the TDC distributions.

Based on these (Figure 3.1) distributions we extract another piece of information. We compare the accumulated number of hits in the tube with the average number of hits per tube in a sector or a chamber. This is how we find the tube's efficiency. Having ten times fewer hits than average means that the tube has only about 10% efficiency. If a tube fires ten times more often than it's neighbors, then it probably has a high voltage problem or a problem with electronics. The information from such tubes is less reliable. We determine the efficiency and reliability of the tubes along with the calibration parameters of the TDC channels .

We calculate two calibration parameters from the rectangular TDC distribution. T_0 is the high edge of the distribution and T_1 is the low edge (Figure 3.1).

We obtain T_0 and T_1 from the rectangular fit of the distribution (Figure 3.1). There are preliminary estimates of the calibration parameters. We find the areas of the TDC channels with approximately the same timing information. The initial parameter for the lower edge is set for these areas (Figure 3.2). We use a constrain in the fit. It is the maximum drift time for the straw tube of a given radius running at given conditions. It is set to the proper value to improve the fitting procedure. The fitting is performed for every separate TDC channel (every tube). The flow chart for the fitting procedure is provided below (Figure

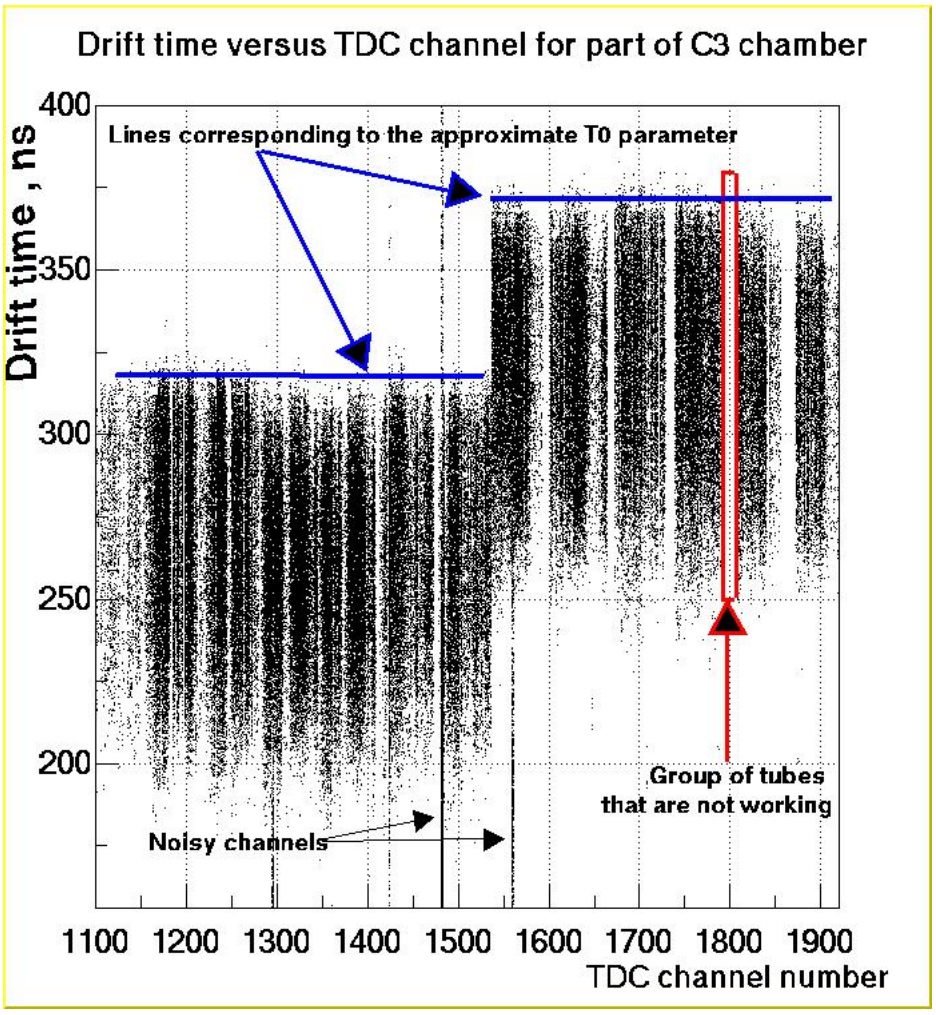

Figure 3.2: The T_{signal} versus TDC channel number for a part of the C3 chamber.

3.3).

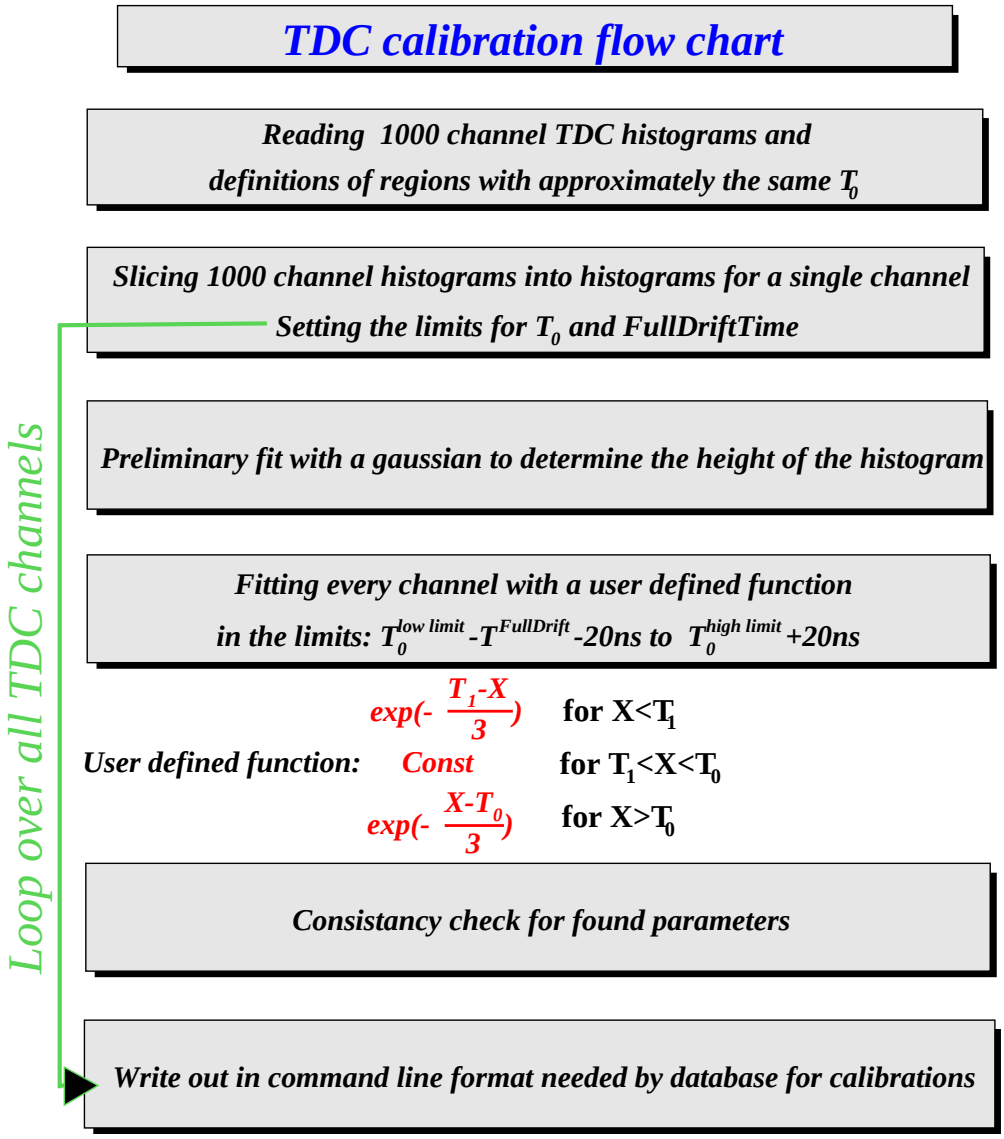

Figure 3.3: The flow chart of the TDC calibration routine.

As a result of the good calibration, we see great improvement in the reconstruction of a track. In Figure 3.4, there are two pictures corresponding to a part of a track in chamber C4. It is reconstructed before (Figure 3.4(a)) and after (Figure 3.4(b)) the calibration of TDCs.

An interpretation of the Figures 3.4(a),3.4(b) follows: the black edges of the circles correspond to the physical walls of the tubes. The red circles represent the actual drift areas inside the tubes. The green line traces the reconstructed (using all chambers and hodoscopes) track of the particle. It has a local derivative (blue line) in the shown region of C4.

Without TDC calibrations the local derivative is not in very good agreement with the particle's trajectory. It worsens the resolution of the reconstructed parameters P_t and Φ of the track. Good TDC calibration brings the local derivative in a much better agreement with the global track reconstruction. It makes the errors on P_t and Φ smaller.

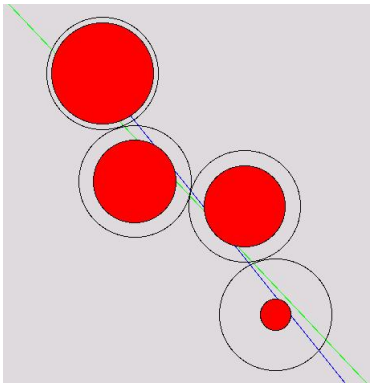

(a) Reconstructed local derivative to a trajectory. Bad TDC calibration

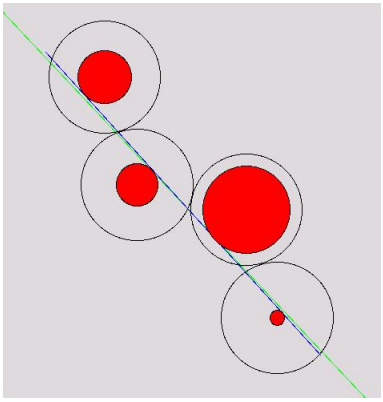

(b) Reconstructed local derivative to a trajectory. Good TDC calibration

Figure 3.4: Examples of straw tubes with bad and good TDC calibrations

3.1.2 ADC calibration

We use the Z-coordinates of the straw tube hits to reconstruct the Θ angle of the track. The coordinates are calculated from the ADC signals. The calculated hit position is not the same as the real hit position. It is related to the slight differences in the electronics at the ends of the straw tubes. A set of calibration parameters is used to adjust the calculated hit position to be equal to the real hit position. We find these parameters via ADC calibration.

The process of the ADC calibration has two stages. During the first stage, we collect data using a special 'noodle' counter. The 'noodle' counter is a very long organic scintillator of 1.5 cm width and about 0.5 mm thickness. We have four of these counters. They are wrapped around the outer chamber (C4). They are long and they become a continuous thin detecting stripe (Figure 2.22). We can include it in the trigger.

Before every large set of data, we collected data without a magnetic field and with the 'noodle' counter included in the trigger. The conditions for accepting events were quite loose. We required that the particle came out of the target, went through all the chambers and hit the 'noodle' counter.

We use a very small target for calibrations. It is a $1cm^3$ Cu target. The tracks have a point-like vertex with this target. The tracks, accepted by the trigger, travel in a cone that has about $1.5cm$ distance between the inner and the outter wall.

To explain the methods of the ADC calibration, we, first, describe the principles of Z-tracking in the straw tube and the parameters of the calibration process.

A charged particle leaves the clusters of electrons and ions as it ionizes the gas. The clusters drift under the influence of the electric field. The signal is induced by the propa-

gation of the ionization in the gas. It travels along the wire toward the ends of the tube. There, it is collected by the electronics.

The resistance of the wire is an attenuator for the propagating signals. The longer the distance that a signal travels along the resistive wire, the smaller the amplitude of the signal at the end of the wire. Calculation of the Z position of the hit in the straw tube involves a comparison of the collected charge at the two ends of a straw tube. The output of the ADC is an integral of the charge, collected from the end of the straw tube.

We can calculate the Z-position of the hit along the tube using the following Equation :

$$Z = \Big(\frac{ADC_{down} - ADC_{up}}{ADC_{down} + ADC_{up}}\Big)\frac{L}{2} + \frac{L}{2}. \tag{3.2}$$

Here L is the length of the tube and ADC_{up}, ADC_{down} are the ADC signals coming from the upstream and the downstream (with respect to the direction of the beam) ends of the straw tubes. The ADC signal can be written in terms of the gain of the STG1 amplifier and the pedestal of the ADC channel:

$$\begin{aligned} ADC_{up} &= \int GAIN_{up} RawSignal_{up} dt + PED_{up} \\ ADC_{down} &= \int GAIN_{down} RawSignal_{down} dt + PED_{down} \end{aligned} \tag{3.3}$$

A straw tube's wire has capacitance and inductance. These are additional sources of the difference in the signals from two ends of a wire. We modify the Equation 3.2 introducing special parameters:

$$Z = \Big(Z_{factor}\frac{ADC_{down} - ADC_{up}}{ADC_{down} + ADC_{up}} + Z_{offset}\Big)\frac{L}{2} + \frac{L}{2}. \tag{3.4}$$

The Z_{factor} and Z_{offset} are the calibration parameters. We implemented several methods of calibration based on Equations 3.3 and 3.4. The calibration procedures for chamber C4 are different from those for C2 and C3. We use runs with noodle counters for C4 calibrations. The calibration for other chambers is done differently. We created two methods. The choice of the method depends on the target configurations.

First, we can find parameters Z_{factor}, Z_{offset} by minimizng the deviation of the hit positions in the straw tube from the real hit position along the track. Second, it is possible to use the edges of the spectrometer's acceptance and the orientiers for calibration. Both of these ways are explored to a great degree.

Before we explain these procedures in details, we will demonstrate the state of the chambers without the calibration. In Figure 3.5 we plot the accumulated distributions of the hit positions for half of chamber C4. The 'noodle' counter is included in the trigger. It wraps C4 chamber as a belt of about $1.5cm$ width.

The center of the distribution (Figure 3.5) for the forth row of C4 should be right at the position of the 'noodle' counter. The 'noodle' was placed at $-.4$ for the data shown in Figure 3.5. The tracks have small θ angle ($\sim 27^{\circ}$).

Because of the angle the hit position differs slightly from the 'noodle' position. The center of the distribution for row 4 has to be at $-.42$ for the properly calibrated channels. The distribution is not at the correct position. However, the important detail is that the relative distances between the distributions for rows 1,2,3 and 4 are quite stable through the entire half of the chamber. The widths of the distributions are also reasonably good. They are $\sim 6cm$ for the entire half of C4 (256 tubes per raw). The ideal width is equal to the width of the 'noodle', about $1.5cm$. We calculate the calibration parameters that bring

the centroids of the distributions toward the real positions of the hits.

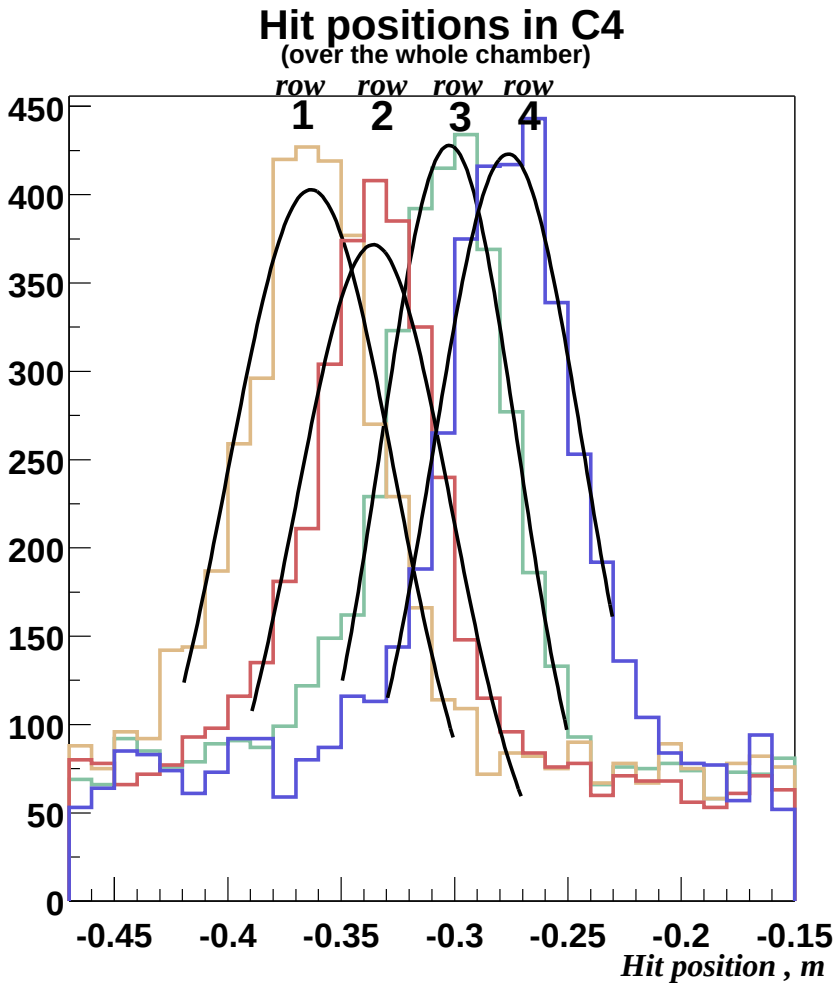

Figure 3.5: The hit positions in the chamber C4. The hit position can vary from -1. to +1. Every peak corresponds to the accumulated distribution of the hit positions for all the tubes in a row of the chamber C4.

The situation with other chambers is worse. In Figure 3.6 we plot the distributions of the hit positions in chambers C2 (Figure 3.6(a)) and C3 (Figure 3.6(b)) for row 2. The width of the distributions is about the half of the length of the straw tube. We cannot use the "noodle" data to get a good calibration for C2 and C3.

The C2 and C3 distributions have such a large width because there is an additional,

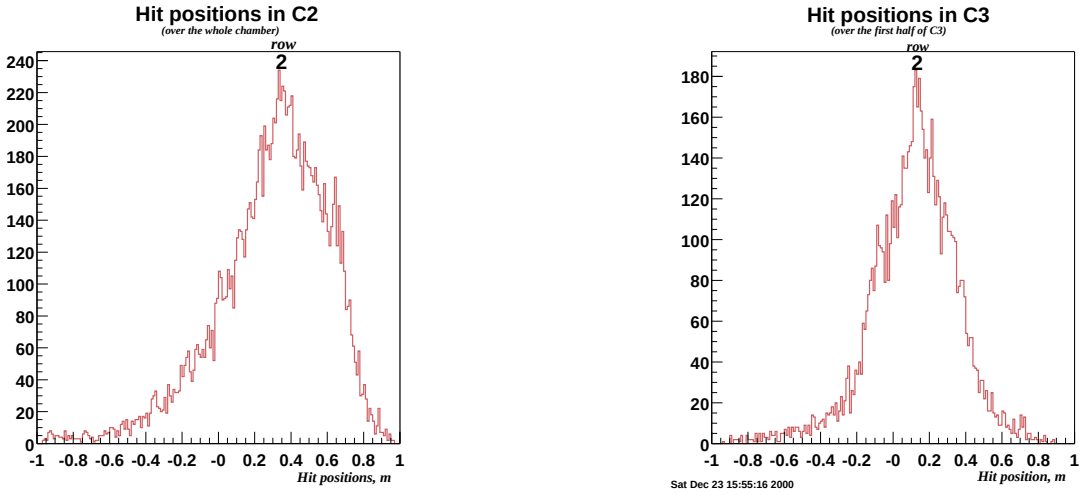

(a) Hit positions in C2 chamber

(b) Hit positions in C3 chamber

Figure 3.6: The hit positions in C2 and C3 chambers. The hit positions can vary from -1. to 1. LEFT: The accumulated distribution (over 256 tubes) of the hit posisitons in row 2 of the C2 chamber. RIGHT:The accumulated distribution (over 256 tubes) of the hit posisitons in row 2 of the first half of the C3 chamber.

indirect, target - Beam Hodoscope. It is used in the trigger and it serves as a beam counter. The target positions are incorrect without good ADC calibration. It is difficult to separate the Cu target from the Beam Hodoscope.

There are interactions in the Beam Hodoscope during the non-calibration runs. These events occasionally satisfy the trigger. The fraction of these events is quite small. In the calibration runs the Cu target is small and the trigger conditions are relaxed. The events from the Beam Hodoscope satisfy the trigger at the same rate, if not more often, as the events coming from the calibration target (Figure 3.7).

The accuracy of the calibrations for C2 and C3 with these conditions is unsatisfactory. The target overlap (Figure 3.7) does not effect C4 to such a degree. C4 is right next to the "noodle". The spread in Z-coordinate of the hits in C4 increases by $\sim 1cm$ from the target

overlap. In C2 the spread is $\sim 50cm$.

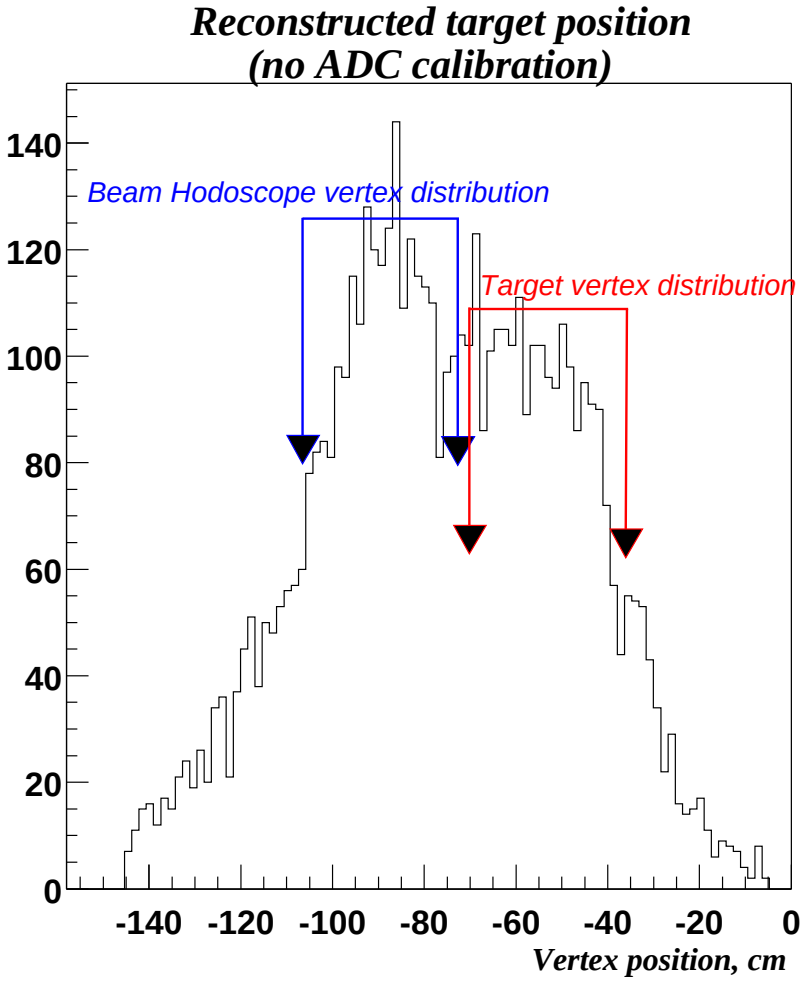

Figure 3.7: Target positions for the non-calibrated ADCs. The real position for the Beam Hodoscope is $Z - tgt = -85$cm and for the Cu target it is $Z_{tgt} = -20$cm.

3.1.2.1 C4 calibration using the 'noodle' counter

We calibrate C4 separately from other chambers. We use the 'noodle' counter for the calibration. We calculate the two calibration parameters for every tube. The 'noodle' data is collected for different conditions. There are runs with the 'noodle' at different places along C4 and runs with different target positions. There is enough information to find the

two unknown calibration parameters.

RUN Numbers	Target position	Noodle position 1 half	Noodle position 2 half	Magnetic field
8253-8255	-10.	-.405	-.305	NO FIELD
8256-8259	-40.	-.405	-.305	NO FIELD
8278-8295	-20.	.330	.365	NO FIELD
8296-8297	-20.	.000	.035	NO FIELD
8298	-60.	.000	.035	NO FIELD
8299-8300	-60.	-.405	-.305	NO FIELD
8301	-20.	-.405	-.305	NO FIELD
8302	-60.	-.405	-.305	NO FIELD
8570-8573	-20.	-.405	-.305	80 kGauss
8574	10.	-.405	-.305	80 kGauss
8591,8594	0.	-.405	-.305	80 kGauss
8657-8668	0.	-.405	-.305	NO FIELD
8857-8862	0.	-.405	-.305	NO FIELD
8864-8868	-20.	-.405	-.305	NO FIELD
8869-8874	-40.	-.405	-.305	NO FIELD

Table 3.1: Table of the 'noodle' positions and other conditions for the ADC calibration data runs.

We rewrite the equation for the hit position in terms of the real and calculated hit positions in the chamber:

$$Z_{real} = \left(Z_{factor} Z_{calculated} + Z_{offset} \right) \tag{3.5}$$

Here Z_{real} is a point, at which the particle passed through a straw tube. The $Z_{calculated}$ is the calculated (Equation 3.2) point, at which, we think, the particle passed through the straw tube. One can see from Equation 3.5 that it is enough to have the 'noodle' at two different positions to find Z_{factor} and Z_{offset}.

The flow chart of the C4 calibration procedure is given below (Figure 3.8). There are two parts to this procedure. In the first half (boxes 1 through 4 of the flow chart in Figure 3.8), we fit distributions for the parts of the sectors. Parts of the sectors are united

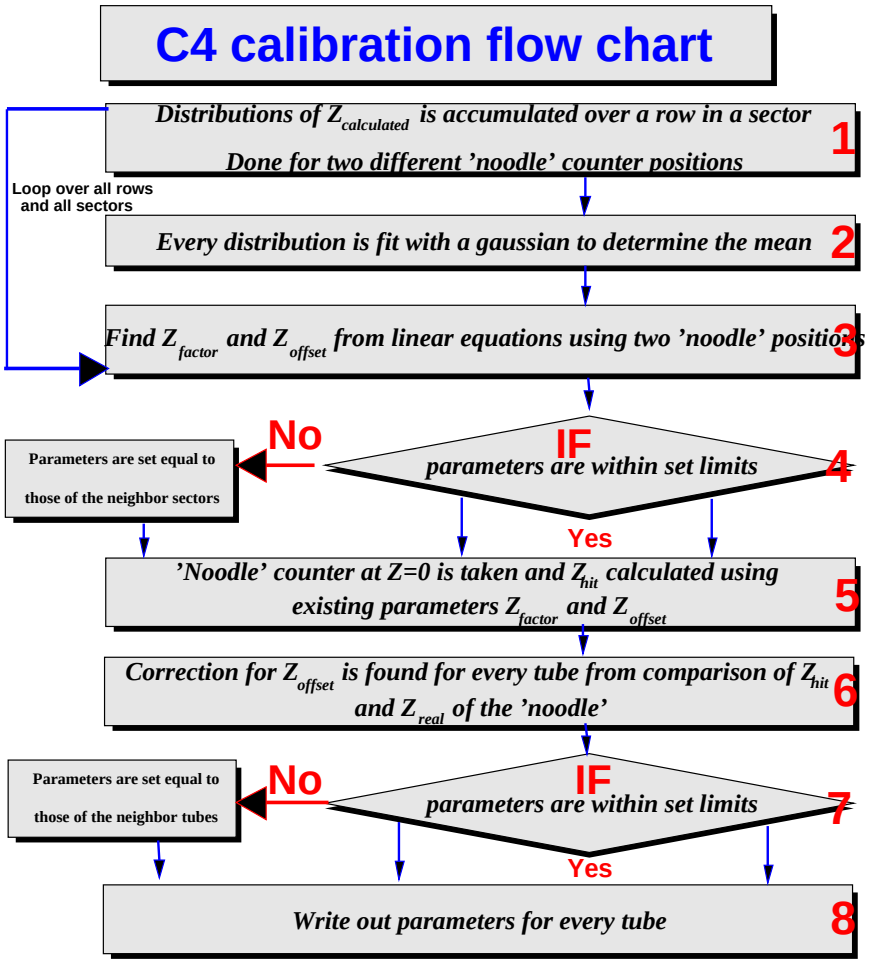

Figure 3.8: Flow chart for the C4 ADC - calibration routine.

to improve the statistics. We combine the groups of tubes from the same row. The real position of the hit is the same for all the tubes in the same row. The positions are not the same for the tubes from the different rows.

The second half of the routine (boxes 5 through 8 of the flow chart in Figure 3.8) is devoted to the fine tunning of the calibrationi parameters of the individual tubes. We use runs with the 'noodle' at the center of the C4 for that. The scintillators are very close to the center of the chamber. At this "noodle" position the effect of the Z_{factor} is very small compared to the situation when the hit is close to the end of the straw tube. We use this property to fine tune the second parameter - Z_{offset}.

The calibrations for C4 are stable through out the data aquisstion period. We have several sets of calibration runs. We used the same C4 calibrations for two 'noodle' runs with 'noodles', that are more then 500 runs apart (more than two months of running). We observed a very good agreement between the real and the calculated hit positions (Figure 3.9).

We calculate the calibration parameters using the runs 8295-8301. We use this calibration to reconstruct the 'noodle' position for run 8839. The reconstructed positions (Figure 3.9) are where they should be according to the measurements. There are about two months of data acquisition time between the runs 8301 and 8839.

The top two pictures in Figure 3.9 show the reconstructed position of the hits in row 4 of C4. The bottom pictures show the reconstructed positions of the hits in all rows. The centroids of the neighboring peaks must be $\sim 4.5cm$ appart. It is correct with good accuracy.

The stability of chamber C4 provides us with the flexibility to use different methods for

calibrating C2 and C3 chambers. There is an option in the reconstruction program to add extra weight to the hits in C4. We can also tie a track to the middle of the target. The constrain on a track to come from the middle of the target and to pass through the hits in C4 introduces a small error in the calibration of C2 and C3.

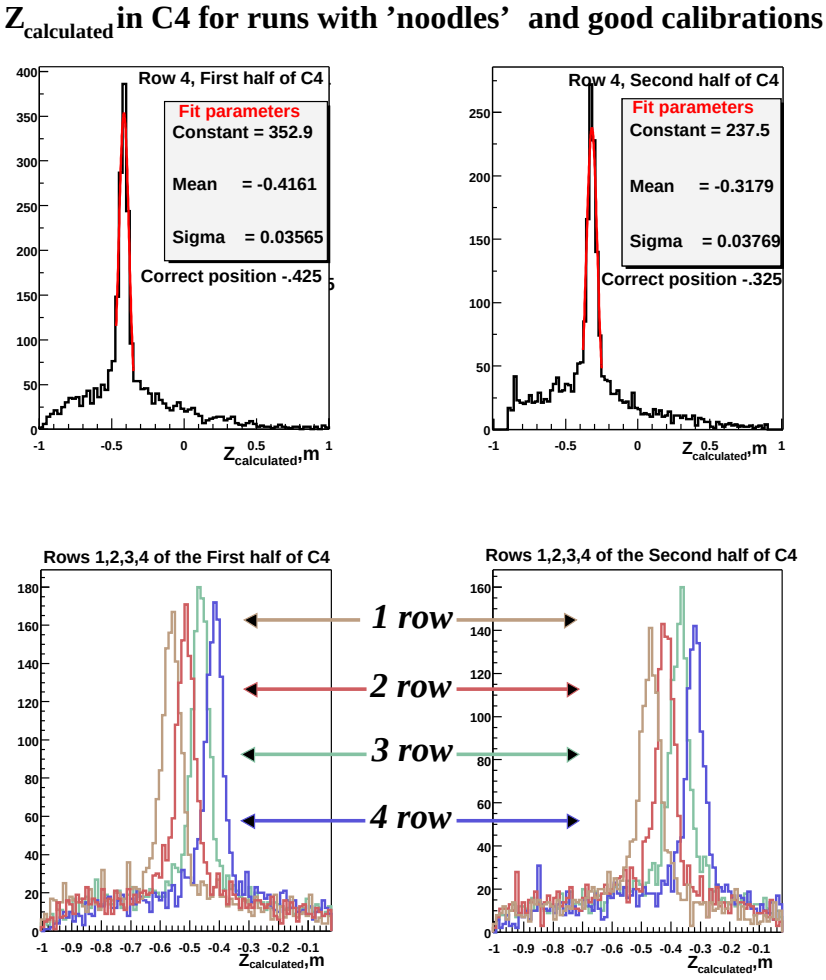

Figure 3.9: Reconstructed 'noodle' position for chamber C4. The calibration parameters, calculated using the runs 8295-8301, are applied in the reconstruction of the run 8839. TOP: The fit of the accumulated distribution of the hit positions in row 4 of the chamber C4. BOTTOM: The accumulated distributions for all rows of the chamber C4.

3.1.2.2 Z_{factor} and Z_{offset} calibration via the deviations from a track

This calibration method can be used for the regular datafiles with one target. We reconstruct a track using C4 and the middle of the target. We then calculate the deviation of the Z-coordinate of the hit, in a straw tube of C2 chamber, from a point where the trajectory of a particle passes through this tube.

We construct a sum of the squares of the deviations of the $Z_{calculated}$ from Z_{track}. The Z_{track} is the coordinate of the intersection of the constrained fit of the trajectory with the calibrated tube.

$$\chi^2 = \sum (Z_{track} - Z_{calculated})^2 = \sum (Z_{track} - Z_{offset} - Z_{factor} R)^2 \tag{3.6}$$

$$R = \frac{ADC_{down} - ADC_{up}}{ADC_{down} + ADC_{up}} \tag{3.7}$$

By minimizing χ^2 we calculate the calibration parameters Z_{offset} and Z_{factor}. After taking a derivative of χ^2 with respect to Z_{offset} and Z_{factor} we obtain the following system of linear equations:

$$\begin{aligned} Z_{factor} \sum R^2 + Z_{offset} \sum R - \sum (R Z_{track}) = 0 \\ N Z_{offset} + Z_{factor} \sum R - \sum Z_{track} = 0 \end{aligned} \tag{3.8}$$

It is not difficult to solve this system of the linear equations and get the equations for the calibration parameters of every tube.

This method of the C2 and C3 calibrations works only for the runs with one target. The good C4 calibration is not enough to distinguish between the two targets that are

close together. It is impossible to determine the magnitude of the deviation from the track (Figure 3.10).

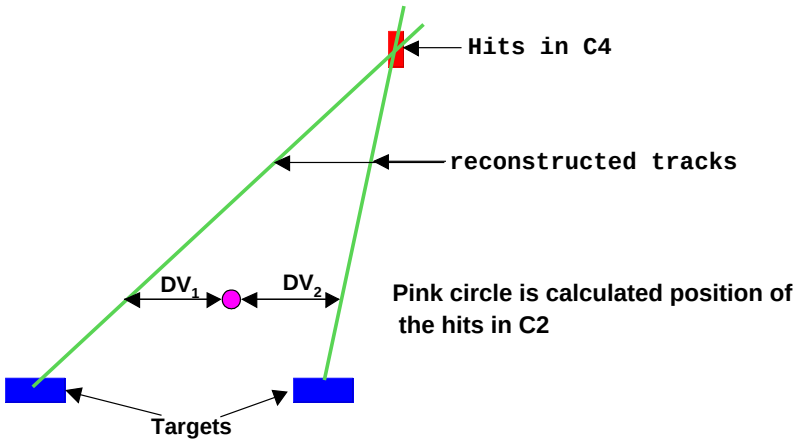

Figure 3.10: A schematic picture of the deviation of the hit from the track for calculations with two targets.

Without good calibration for C2 and C3, we cannot decide accurately from which target the particle came out. We can have two possible particle trajectories instead of one for the events with two targets (Figure 3.10). particle. The magnitude of the deviations DV_1 and DV_2 depends on the chosen target. Mixing deviations from the correctly recognized target with the ones, calculated using the wrong target, makes calibrations inaccurate. The same is true, even to a larger degree, for the three target configurations.

To get good calibrations for C2 and C3 via this method we need good calibrations to start with. It is a 'closed circle'. We choose a different method for calibrations with two and three targets. It is covered in the next section.

3.1.2.3 Z_{factor} and Z_{offset} calibration via the detection of the acceptance edge

We designed a new method for the data with multiple targets. We use the fact that the particles are accepted by the trigger only if their trajectories are in a certain angular range in the RZ-plane (Figure 3.11).

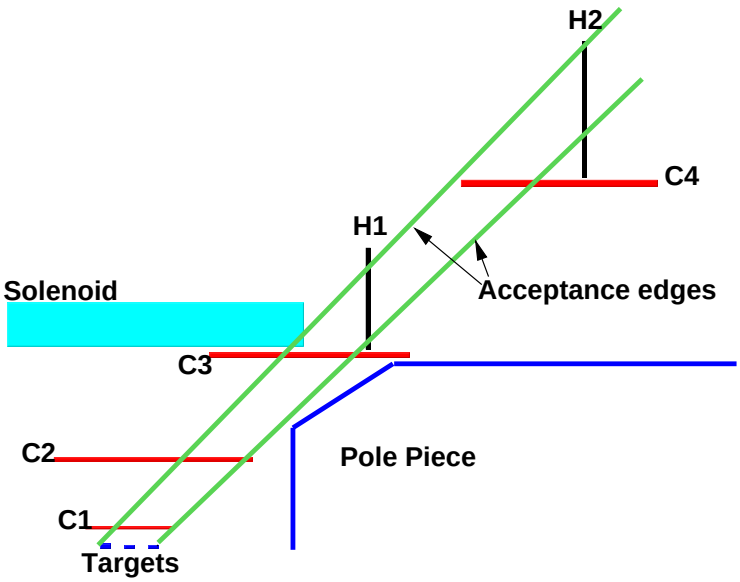

Figure 3.11: The RZ-plane section of the detector. The acceptance edges are shown with green lines.

The Level1 trigger accepts events in which the particles are detected in the H1 and H2 hodoscopes. The tracks with hits in the hodoscopes are restricted in Θ angle by the size of the hodoscopes. The two green lines in Figure 3.11 are the boundaries within which the trajectory should lie. The acceptance creates the regions of the hits (Figure 3.12) in the chambers C2 and C3. The calculated hit positions should be accumulating in these regions. There are two imaginary boundaries in the RZ-plane. We obtain two equations for the $Z_{calculated}$ distributions using the edges of the acceptance. The calibration parameters Z_{factor} and Z_{offset} are calculated from the system of two equations.

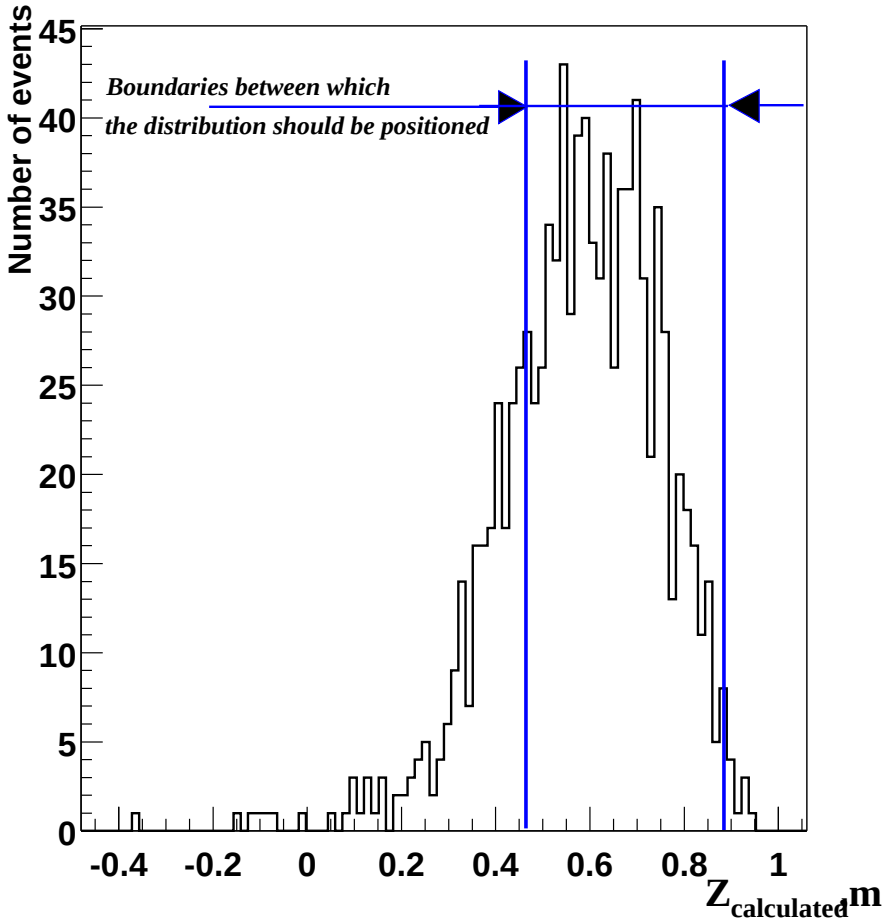

Figure 3.12: A distribution of $Z_{calculated}$ for row 1 of one of the sectors in C2. The tracks come from the three targets. The ADCs are not calibrated.

We calculate Z_{factor} parameter for accumulated distributions in a row of a sector. Prior to the calculations we move the $Z_{calculated}$ distributions for the individual tubes. The centers of the distributions are shifted to the same position. The Z_{factor} and Z_{offset} are calculated for the whole row at once. Afterwards, the Z_{offset} is adjusted for the individual tubes.

The equations for the calibration parameters are as follows:

$$Z_{factor} = \frac{Z_{left}^{edge} - Z_{right}^{edge}}{Z_{left}^{calculated} - Z_{right}^{calculated}} \tag{3.9}$$

$$Z_{offset} = Z_{left}^{edge} - \frac{Z_{left}^{edge} - Z_{right}^{edge}}{Z_{left}^{calculated} - Z_{right}^{calculated}} Z_{left}^{calculated}$$

Here $Z_{left,right}^{edge}$ are the acceptance limitations on the Z coordinates of the trajectories for the chamber C2 or C3. The $Z_{left,right}^{calculated}$ are the edges of the distribution of the calculated coordinates in C2 or C3. The coordinates are calculated using Equation 3.2.

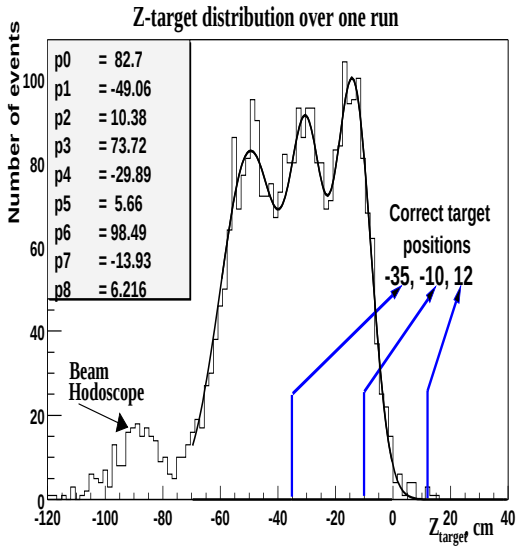

Figure 3.13: The target positions. Reconstruction is done without ADC calibrations. The data of one run.

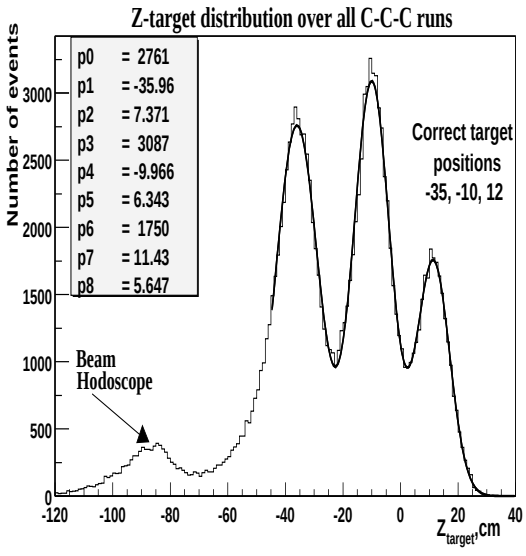

Figure 3.14: The target positions. Reconstruction is done with good ADC calibrations. The data of all C-C-C runs.

3.1.3 Detector alignment

The 3D-alignment of the chambers is a very important part of the EVA spectrometer calibration. The proper positions of the chambers are crucial for an accurate reconstruction of the track's parameters. The 3D-coordinates of the parts of the spectrometer were surveyed by the team of professionals from BNL. It was done every time we moved the chambers. Their measurements were of a very good accuracy. However, further alignment was performed before we started data analysis.

The task of alignment is greatly simplified by the design of the chambers. The straw tubes are united into sectors. They are secured at both ends on the rigid brass endplates. The endplates are themselves tightened to the aluminum frame. The frame sits on the stainless steel rails.

A rohacell ring is installed to insure the additional support for the middle of the $200cm$ long tubes. The positions of the tubes in the sectors and sectors in the chambers are know from the construction blue-prints. The main concern in the spacial alignment is the relative position of the chambers.

The EVA spectrometer has the cylindrical symmetry. There are two unknown parameters in the chamber alignment. The first parameter is the vector of the shift of the centers of the chambers with respect to each other. The second parameter is the angle Φ of the rotation of the chambers in the $R\Phi$ plane. Special runs were taken during the data acquisition to gather information for the chamber alignment.

We explain the calibration in more detail. A reconstructed track has bunches of tubes (Figure 3.4) in the chambers. The hit coordinates in the bunch are fit with a straight line.

It is called a stub (blue line in Figure 3.4). The stub is the tangential to the track in the vicinity of the bunch. The stubs of a straight track should be aligned exactly along the track. For the detector alignment, we collected the data without the magnetic field. In the absence of the magnetic field the tracks are straight.

A stub has an important property. It points back to the vertex of interaction for straight tracks. A collection of the stubs in a chamber points toward the place where the beam was hitting the target during the run.

This property is used to find the shifts of the centers of the chambers with respect to the Z-axis of the detector. The stubs are analyticaly continued as a line in the XY-plane. We find the point of the intersection of the lines from the same chamber for the events with the two straight tracks. A distribution of the points of the intersection is found for each chamber. The coordinates of the centroid of this distribution determines the shift of the chamber in the XY-plane.

After the shift in XY-plane is calculated, only the rotation of the chambers with respect to each other is unknown. We calculate the rotations of the chambers with respect with the C2 chamber. The rotation of C2 is determined with respect to the hodoscope hits. It is small compared to the size of one hodoscope bin.

A more detailed explanation of the spectrometer alignment can be found elsewhere [3].

3.2 Event reconstruction

3.2.1 Hodoscopes pre-selection

Scintillating hodoscopes are part of the Level 1 trigger. During the reconstruction they serve as a crude selection tool. For example, to select events with two tracks, we impose a condition on the number of hits in the hodoscopes. It should be not more then two in H1 and not more then two in H2. It accounts for one hit in H1 and H2 for each of the two tracks. It is possible to check this condition right after the raw information is read from the datafile. It saves the time which would be taken by track formation and reconstruction using the straw tubes.

A list of tracks is formed to have a more efficient selection process. The list is based on the hits in the hodoscopes. It is correlated with the tracks that are formed using the hits in the straw tube chambers. A track in the hodoscopes is formed in the following way. We loop over the hits in H1. We search for the hit in H2 that is within 20 hodoscope bins or .5 radians from the H1 hit. These two hits form a track in hodoscopes. If there are no hits in H2 that satisfy this criteria, a combination of hits in H1 and H2 with the smallest difference in azimuthal angle is taken. If there are no hits in H2 that we can relate to a hit in H1, a track is formed from the H1 hit alone. The list of the hodoscope tracks is correlated with the list of tracks formed using the hits in the straw tube chambers.

Several methods are used to obtain the information about the number of hits in H2 and H1, the number of tracks formed in the hodoscopes and the quality of the tracks.

A cut can be used during the event processing. It's name is **CUTONHOD**. **CUTONHOD** is a pre-selection cut. It puts a constrain on the Φ angles of the two main high P_t

tracks. We check the following ocndition:

$$||\Phi_1 - \Phi_2| - \pi| < .7 radians \tag{3.10}$$

This cut is useful for selecting elastic and quasi-elastic events. For them $||\Phi_1 - \Phi_2| - \pi| \simeq 0$.

3.2.2 Straw tube grouping

At the begging of the reconstruction we have a list of the hit tubes. The tubes have the TDC and ADC signals. The ADC and TDC information does not have to be complete. Sometimes, a tube has good TDC information but the ADC information is not usable. A *chop_cut* method is used to temporary get rid of the straw tubes with incorrect information. We form bunches from the tubes with good ADC and TDC information.

A bunch is a group of tubes that belongs to a single chamber. It is produced by a particle passing through the straw tubes. In an ideal case a particle leaves four tubes in a special formation (Figure 3.4(b)). However, there are tracks with three, two, one or no tubes to form a bunch in a chamber.

We run a loop over the tubes in the event list to make a list of bunches. The tubes within 5° of azimuthal range from one of the tubes in the list form bunches. A track that passes through a bunch has a certain tangential. The tangential can be calculated from the hit information of the tubes in the bunch. We call this tangential a stub.

Stub (Figure 3.4a,b - blue line) is a line going through the bunch in the way a track would go. Parameters of this line are calculated using the least square deviations fit for all the hit positions of the tubes in the bunch. Stubs are local representations of the particle's trajectory. They are used in the reconstruciton of the track parameters.

3.2.3 Track formation and parameters reconstruction

We loop over the list of bunches to form track. The bunches that are within 25° of the first chosen bunch are written into the track list. Tracks with four or three bunches are undergoing the reconstruction of the trajectory. The tracks with two or one bunch do not have enough information. We are unable to extract all the parameters.

We sort the list of tracks based on the track parameters. First, we sort the tracks in the order of decreasing P_t. The two tracks with highest P_t are considered to be main tracks. They are sorted with respect to the Θ angle. Track number one has the smaller Θ angle.

The calculation of Θ angle is straight forward. The trajectory of a particle in the RZ-plane is a straight line, to a good approximation. It is not straight in the vicinity of the point of interaction when the vertex is away from the Z-axis. In this region we neglect the fact that it is not a straight line. We continue the line untill it intersects the Z-axis at the point Z_0.

We calculate the Θ angle and Z_0 by using the least square deviation procedure for the hits in the track. The Θ is the polar angle of the track and Z_0 is the Z-coordinate of the vertex.

There are two constrains that we can impose on the reconstructed track. We can add fictitious 'hits' in the middle of the target and weigh the hits in C4. Adding 'hits' in the middle of the target decreases the error on Θ angle. The error comes from the calibration of C2 and C3.

The tracks come from some point in the 6cm long target. We introduce a 3cm error on the Z-coordinate of the tracks by constraining the track to come from the middle of the

target. However, without the constrain, the tails of the distribution of the Z-coordinate for a single target go as far as $20cm$ from the middle of the target. It introduces a large error for the reconstructed angles.

Constraining the track by weighing the hits at C4 can improve the resolution, since calibration of C4 is very good (Figure 3.9).

Reconstruction in the $R\Phi$-plane is not as trivial. We can use two procedures to reconstruct P_t and Φ of the tracks. The trajectory of a charged particle depends on the magnetic field of the EVA spectrometer. There is a constant magnetic field along the Z-axis of the detector. The magnetic field is described in section 2.2.1.

In the magnetic field the trajectory of a charged particle in 3D is a helix. The projection of a trajectory on the $R\Phi$-plane is an arc. After a particle leaves the magnetic field, the trajectory is a straight line. The average raduis of the curvature of a charged track with P_t of 1.5 GeV is about $550cm$. We approximate the trajectory of a charged particle inside the magnetic field by a parabolic curve. The error in the calculations from this approximation is less then 100micron of deviation from the real trajectory.

We use three or four points to find the parameters for a good track. We transform the hit coordinates into a local coordinate system. It is shifted to have the origin at the first hit chamber. It is rotated to have the X-axis along the line connecting the first and the last chambers hit (Figure 3.15).

A set of variables is used in our reconstruction. One of the variables is called a sagitta (Figure 3.15).

$Sagitta_{KLM}$ is a deviation of the hit in chamber C_L from the line connecting the hits in chambers C_K and C_M. Another important variable is called R170 (Figure 3.15). It is

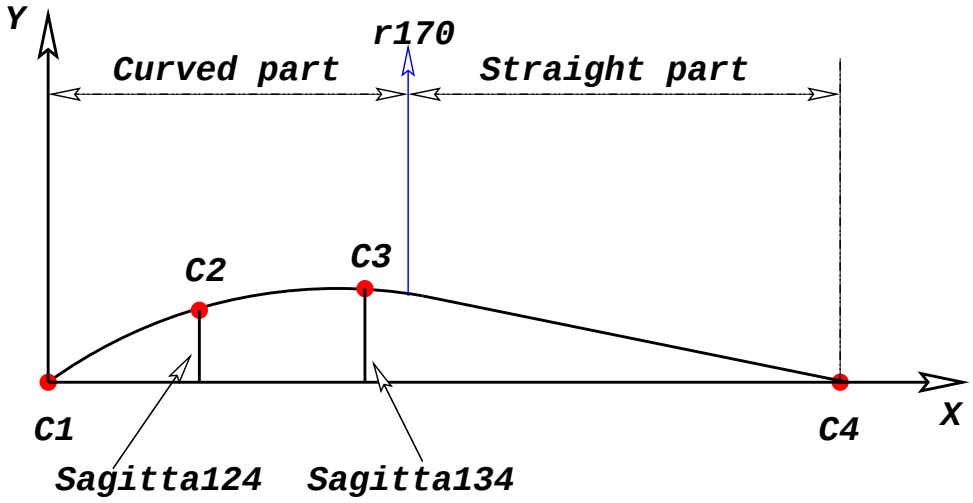

Figure 3.15: The new, rotated, coordinate system and examples of the sagittas.

defined as a distance R from the Z-axis at which the particle leaves the magnetic field. It is R_{track} if $Z_{track} = 170cm$ (Z=170 is the end of the magnetic field). A detailed explanation of the P_t and Φ calculations using sagittas is explained by A.Leksanov [3].

Another approach to the track reconstruction is to minimize the deviations of the hits from a function fitting the trajectory of the particle. The function is a parabole inside the magnetic field and a straight line outside. The straight line is a continuation of a tangential to the track at the point of exit from magnetic field.

The initial parameters of minimization are P_t and Φ. They are taken from the previously described algorithm. The P_t and Φ are changed by doing consequent iterations until the deviations of the hits from the track become minimal.

The shape of the trajectory depends on the point of exit from the magnetic field. We perfomed the Monte Carlo studies of the trajectories of the charged particles with $P_t = 1.55$ and different Θ angles in the presence of the magnetic field.

The dependence is a consequence of the changing magnetic field strength near the end

of the magnetic field. It affects the particle's trajectory depending on the Θ angle or R170 parameter of the track. The particle can stay in the homogenious magnetic field for a longer time, if the Θ of the track is large. It creates a dependence of the direction of motion of the charged particle on the Θ angle after exit from the magnetic field.

We generated tracks at a fixed $\Phi = 45^{\circ}$ angle in the $R\Phi$-plane and at fixed $P_t = 1.55GeV$. We varied the Θ angle and observed the changes in the trajectory of a particle. We define a tangential to the trajectory at the point C_i (see Figure 3.16). It is a local derivative of the trajectory at the point C_i.

In Figure 3.17 we plot the angle of the tangential to the track at the chambers C1 and C4. The scale is the same for the C1 and C4 curves. The C1 curve is shifted so that the average magnitude of the angle is the same.

The C1 is inside a homogenious field. We see no dependence of the angle of the tangential to the track on the Θ angle in the region of the homogenious field (Figure 3.19). The angle of the tangential to the track is the same for all polar angles.

The aperture of the detector is in the gap between the magnet and the pole piece. The field is not homogeneous in this region. The trajectory of a charged particle has a dependence on the Θ angle in the acceptance of the detector.

The C4 is outside of the magnetic field. The tangential to the track at C4 is determined by the tangential of the track at the point of exit from the magnetic field.

One can see in Figure 3.18 the change in the angle of the tangential to the track depending on the Θ angle of the track. The dependence can be approximated with a polynomial (Figures 3.18,3.19).

We parameterize the trajectory after all the variables are calculated. A particle is

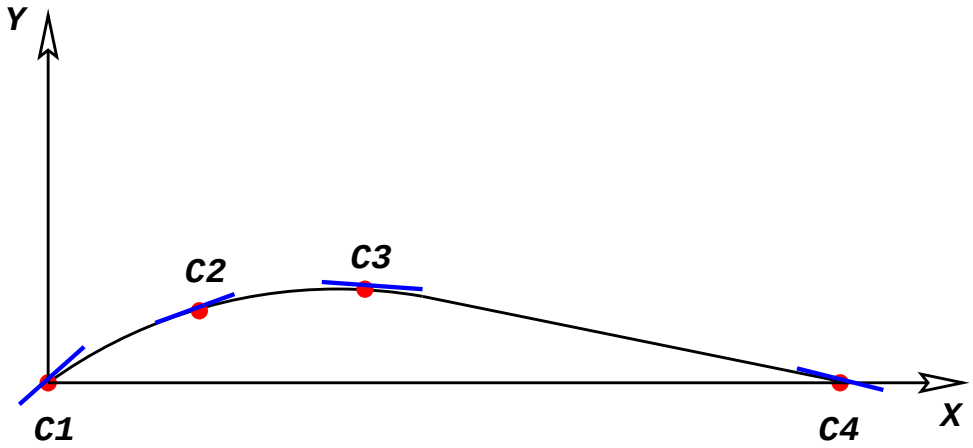

Figure 3.16: The tangentials (blue) to the track.

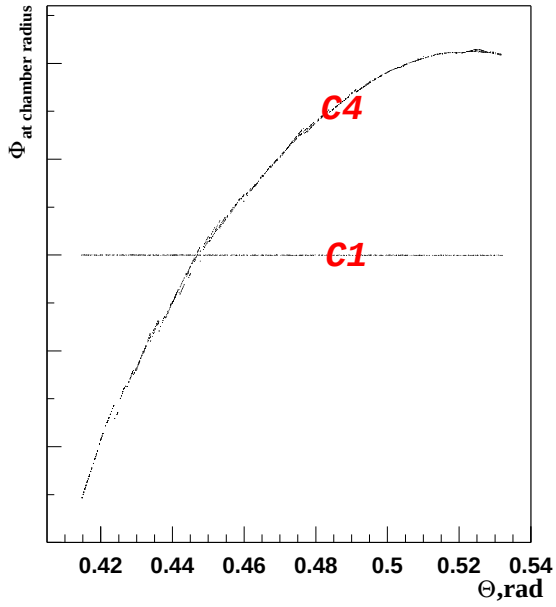

Figure 3.17: The dependence of the Φ angle of the tangential to the track on the Θ angle of the track. Comparison of the tangential to the track at C1 and at C4.

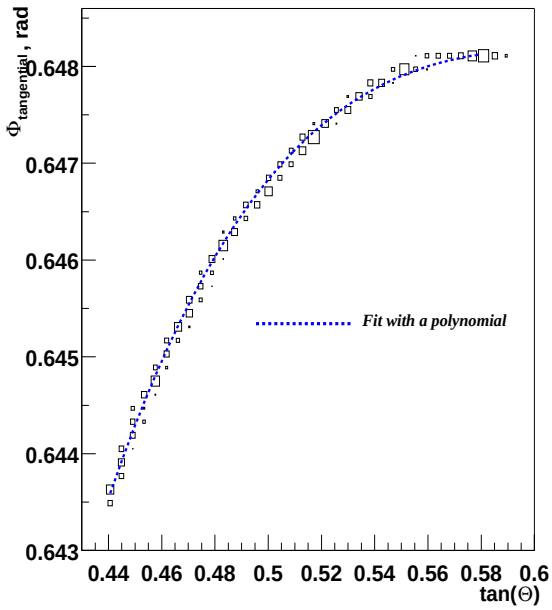

Figure 3.18: A fit of the Φ-angle dependence on Θ for the tangential at C4.

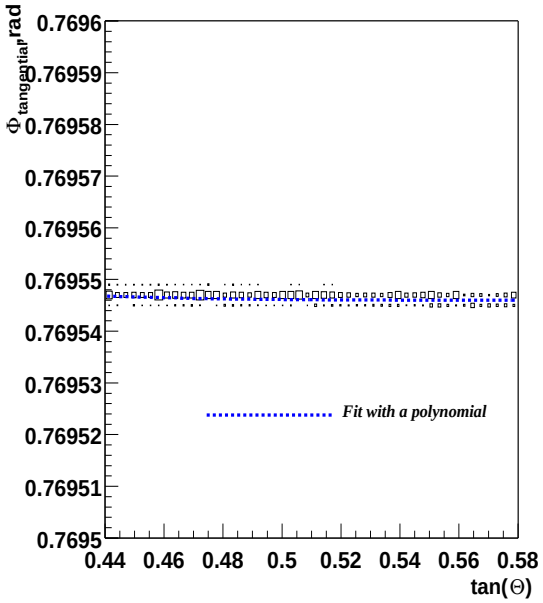

Figure 3.19: A fit of the Φ-angle dependence on Θ for the tangential at C1.

moving in the magnetic field along a helix. The helix is given by TrackPhase, TrackCenter, TrackRadius and InitialPosition. A particle is moving along the straight line after leaving the magnetic field. We calculate the helix parameters from the ones that describe the track in the $R\Phi$ and the RZ planes. The trajectory is defined as follows:

$$
\begin{aligned}
X &= X_{center} + R_{track} cos\Big(\Phi_{init} - \frac{Z - Z_{vertex}}{R_{track}} tg(\Theta_{track})\Big) \\
Y &= Y_{center} + R_{track} sin\Big(\Phi_{init} - \frac{Z - Z_{vertex}}{R_{track}} tg(\Theta_{track})\Big) \\
Z &= Z_{vertex} + V_{||} t
\end{aligned}
\tag{3.11}
$$

In these equations X_{center}, Y_{center} are the coordinates of the center of the circle with radius R_{track} along which a particle's trajectory is aligned. A 3D-parametrized trajectory is useful for calculating the vertex position of the interaction and for graphical representation of a

particle's motion. Detailed description of the helix parametrization can be found in the Appendix B.

The last calculated variable is the vertex position. We define a Z-coordinate of the vertex in the RZ-plane as $\frac{Z_1+Z_2}{2}$. $Z_{1,2}$ are the coordinates of the intersection of the trajectories with the Z-axis. We have two methods to calculate the 3D-vertex.

In the first method we find the point of the closest approach of tracks to the Z-axis. The average of the coordinates of these point is the crude definition of the vertex. In the second method we find the point of the closest approach of the two main tracks and use it as a 3D-vertex.

Both of these methods are incorporated in our reconstruction program. In these approaches, we use consequent iterations by going along the Z-axis and searching for the point, where the corresponding distance is minimal.

We are not looking for the intersection of the two trajectories. The errors in P_t or other variables lead to the situation when the two main tracks are passing next to each other but do not intersect.

In Figures 3.21,3.23 we show the quality of the vertex reconstruction using parametrized trajectories. We generate events with vertices in the region between two circles in XY-plane.

The two methods of the vertex reconstruction are used. In the left Figure 3.21, one can see vertex reconstruction using the point of the closest approach of the tracks to the Z-axis. The vertex position has filled the whole inner region.

The smearing is caused by the dependence of the trajectory on the Φ angle. The generated track has the vertex off the Z-axis. It can have such a Φ angle that analiticaly continued trajectory passes close to the Z-axis (Fig 3.20). The calculated vertex position

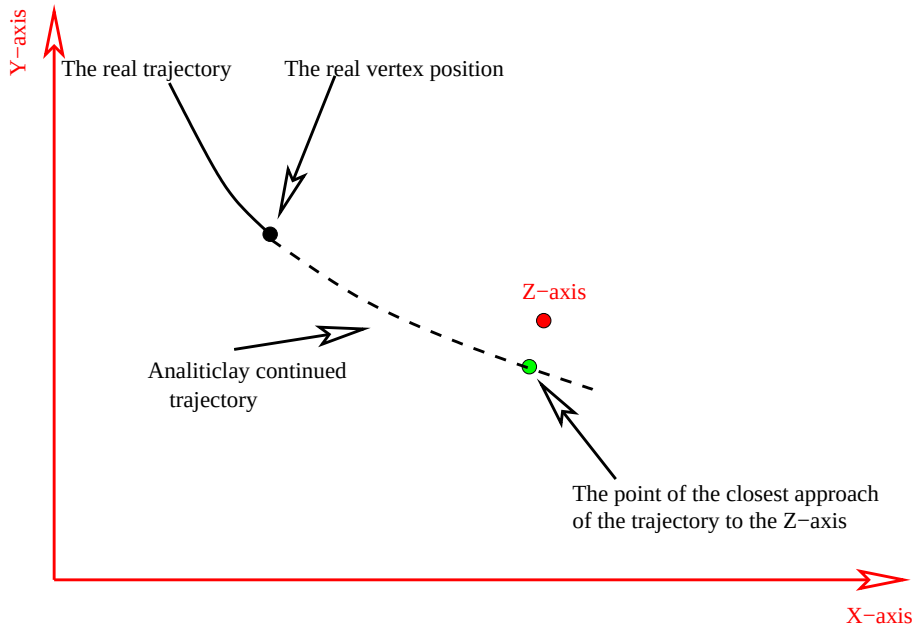

Figure 3.20: The smearing in the position of the reconstructed vertex.

depends on the Φ angle. The vertex can be calculated anywhere inside the circled region (Figure 3.21).

The method of the point of the closest approach between the two main tracks works with very good accuracy (Figure 3.23).

The vertex position is the last calculated variable. We write out the calculated parameters in different ways. The formats of the output can be controled by a user. We discuss the output in the next section (section 3.2.4).

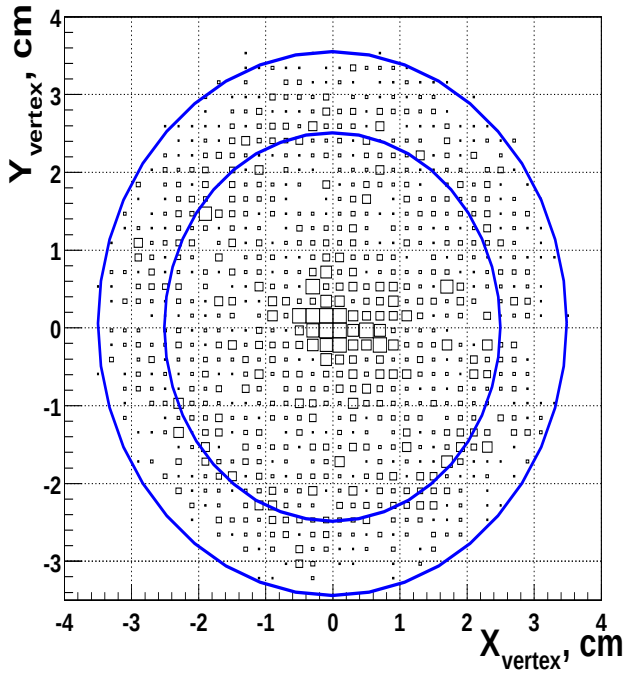

Figure 3.21: One track vertex reconstruction. The vertex is at the point of the closest approach of the track to the Z-axis. The points should be between the blue circles.

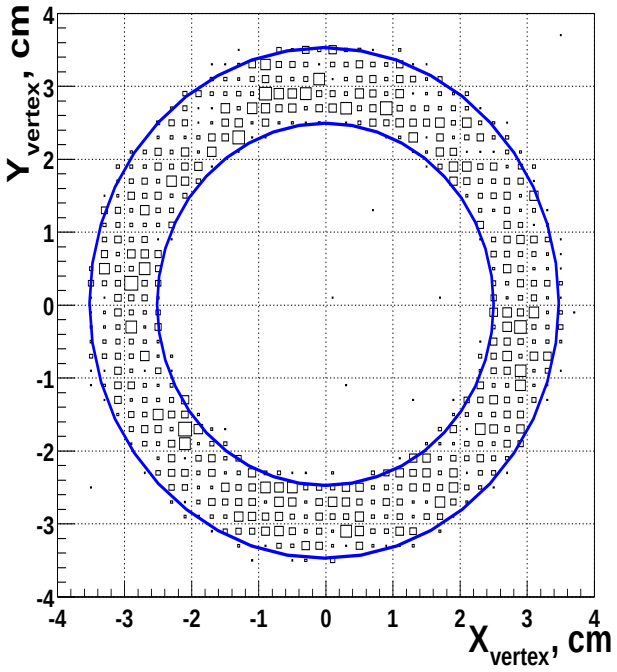

Figure 3.22: Two track vertex reconstruction. The vertex is at the point of the closest approach of the two tracks. The points should be between the blue circles.

3.2.4 Event output

The output format evolved over the years together with the reconstruction program ($WZOFF$). There are two modes in which *WZOFF* can be run: Run-by-run and BATCH. The run-by-run mode is for running one data file at a time. The BATCH mode lets a user to have a group of files analyzed without constant supervision and assistance.

At first the code was written in fortran. The analysis was performed using PAW (CERN). The output from the reconstruction program was written in the form of Ntuple. The Ntuple is a matrix of variables. In 1998 a part of the reconstruction program was re-written in C++ and the GUI was added as a convenient and useful tool. The recent appearence of ROOT - the C++ based analysis package from CERN (evolved from PAW) pushed us toward providing another, object-oriented, form of the output.

3.2.4.1 Fortran based output

The fortran based output is suited for use with PAW. There is a set of commands in *WZOFF*. The commands can read, operate and write any variable stored in the memory banks by *WZOFF*. The *WZOFF* reads the set of commands from a file at the beginning of the execution. The file has a **.cmd** extension. By following commands in **.cmd** file *WZOFF* creates an output in an ntuple form readable by PAW.

The **.cmd** files are created by users and have a set of variables for specific tasks. For example, for data analysis we create a **.cmd** file with physics variables $P_t, \Phi, XYZ_{vertex}, \Theta$. For ADC calibrations we write out $ADC_{up,down}, TDC_{channelnumber}$. Our colaborators, working on neutron analysis, added neutron variables to the ntuple.

The size of the ntuple depends on the number of variables. The ntuple can be quite big. We have a set of **.cmd** files targeting different needs to save space.

3.2.4.2 Graphical User Interface (GUI) - Event display

The GUI was added to *WZOFF* together with the C++ code. An interactive window is opened as *WZOFF* is executed. It is called the Event Display. It has menus to allow a user to open different types of datafiles, set analysis conditions and control the analysis via special command language ([27]).

One of the great options of the Event Display is that a user can look at the event on the screen. The user can see the hits in the detectors, reconstructed trajectories, parameters and all kinds related to the event information. This feature includes the display in the $R\Phi$ (Figure 3.23) and the RZ (Figure 3.24) planes. Event Display is a great addition to

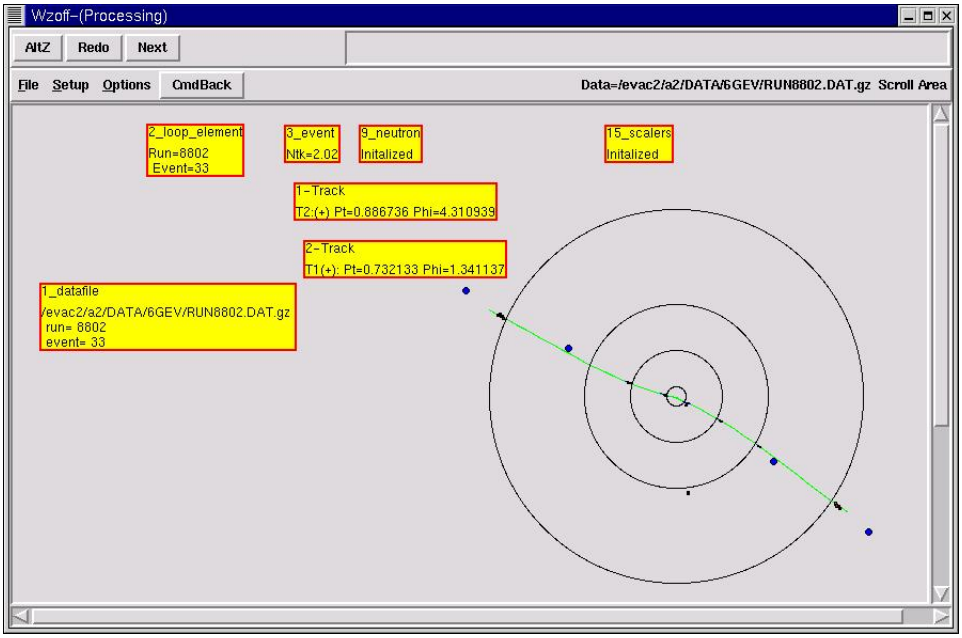

Figure 3.23: Example of the Event Display in the $R\Phi$ plane

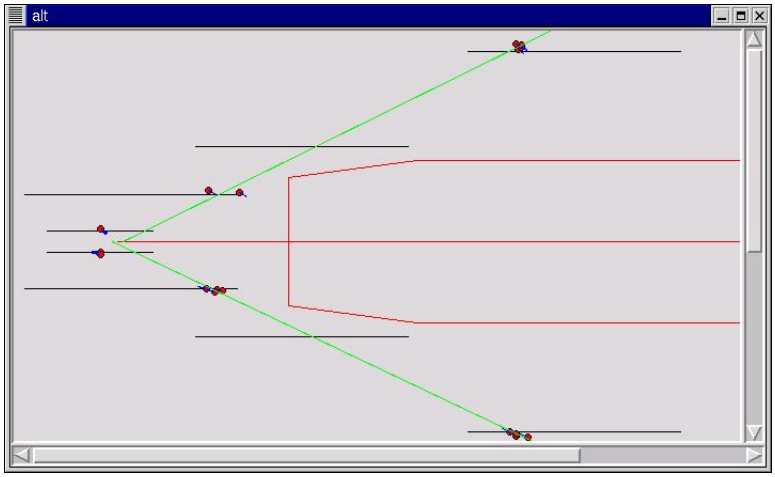

Figure 3.24: Example of the Event Display in the *RZ* plane

WZOFF. It helped us to find and eleminate a number of problems during the calibration and analysis.

3.2.4.3 C++ based output

Recently we upgraded our analysis package to ROOT (CERN). It is C++ based modification of PAW. It can work with the ntuple files. However, we create the output files in a form that makes analysis more efficient when using ROOT. The output is a Tree that has a hierarchy of an Event. The Event consists of objects such as Track, Bunch and Neutron. ROOT's interface is more user-friendly and graphically advanced then that of PAW. Most of the figures in this work are created in ROOT.

Chapter 4

Theoretical background

Introduction

In this chapter we will explain the theoretical basis for our research. As we pointed out in Chapter 1, the interest in hard semi-inclusive pp interactions arose from the results obtained in the **color transparency** analysis and the analysis of the backward neutrons. We give a characterization of semi-inclusive processes in the vicinity of the kinematic region of the quasi-elastic events.

In Section 4.1 we discuss in detail the processes of hard scattering. The cross section of the hard wide-angle scattering has a strong power law dependence on the CM energy. There is a qualitative description of the theoretical arguments for the existence of the power law in Section 4.1.1.

In Section 4.1.3 we explain the nature of the **color transparency** phenomenon and the special conditions necessary to observe it. We will show the new results of the energy dependence of the nuclear transparency.

We discuss the hard quasi-exclusive interactions that could produce the $pp \to pp\pi^0$ events used in the analysis in Section 4.2. We will investigate the possible channels of the $pp \to pp\pi^0$ interaction. For one of them we provide cross-section formula in the high-energy

approximation.

4.1 Hard Scattering

4.1.1 Energy Dependence of the Hard Elastic Hadron Scattering

The E850 experiment was intended to study the processes of exclusive hard scattering. A signature of the hard scattering is the large momentum transfer between the participants. It translates into the high transverse momentum (P_T) of the products of the reaction.

The large momentum transfer is obtained when the scattering is around 90° in the center of mass frame (CM) in the incoming channel. A standard set of kinematic variables is used

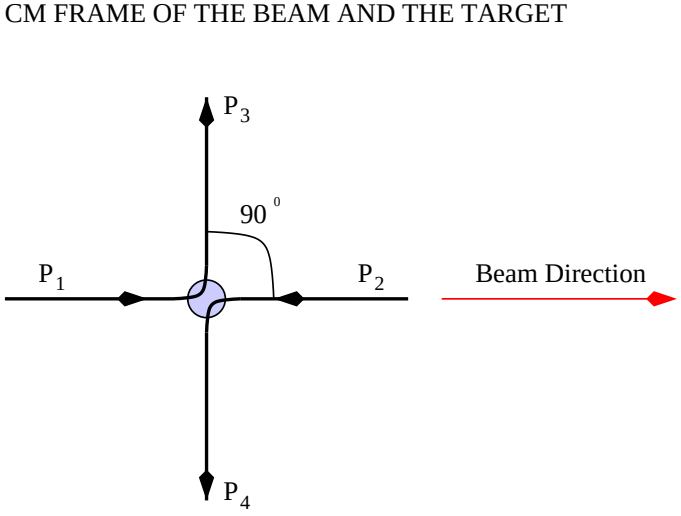

Figure 4.1: Scattering at 90 degrees in the CM frame.

in the calculations of the cross sections. These are Mandelstam variables.

$$s = (P_1 + P_2)^2 \qquad t = (P_1 - P_3)^2 \qquad u = (P_1 - P_4)^2 \tag{4.1}$$

Here by P_i we understand the four-vector of the momentum of the i-th particle. Momentum transfer Q is defined as $Q^2 = -t$. For the scattering at 90° in the CM frame, t is

approximately equal to $-s/2$. The beam energy should be large for a reaction with large momentum transfer.

At large energies the exclusive process can be described in terms of the scattering among the individual constituents of the participants. The pp elastic scattering is modeled as a scattering of three quarks on three quarks. Introducing additional scattering, for example, of the parts of the meson cloud, may suppress the scattering amplitude. Every additional scattering should be hard. Otherwise the condition of the elastic scattering will be lost.

The first calculation of the wide-angle elastic hadron-hadron scattering cross section in terms of quark scattering was carried out by Brodsky *et al* [29]. The cross section dependence was found to be $\frac{d\sigma_{CM}^{90^\circ}}{dt} \sim s^{-12}$ using the constituent interchange model.

In this model Brodsky *et al* treated hadrons as a two-component system. One of the requirements was that there is no gluon exchange between the constituents of the different hadrons. Mesons had a spin 1/2 parton and a spin 1/2 core. Baryons were introduced as a spin 1/2 parton plus a spin 1 or 0 core. The calculated cross sections for meson-meson and photon processes were in good agreement with data [29]. The baryon-baryon cross section did not describe well the s-dependence seen in the data.

There exists numerous data on hard elastic pp scattering with different beams and at different energies. The best fit to the data [30] of the s-dependence of the elastic cross section is $s^{-9.7}$ (Figure 4.2).

To accomodate the data, Brodsky and Farrar [4] proposed the phenomenological scaling law for the assymptotic energy dependence of the hadronic cross section at fixed CM angle.

$$\frac{d\sigma}{dt}(AB \to CD) \sim s^{2-n} f(t/s) \tag{4.2}$$

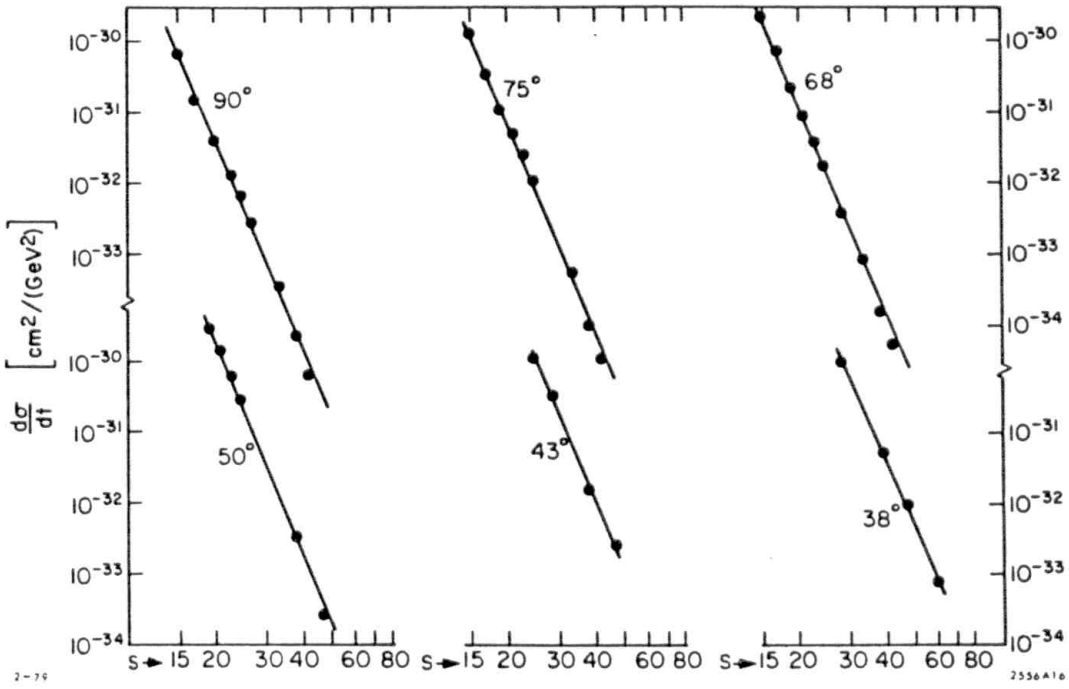

Figure 4.2: Elastic pp cross section at fixed CM angles with a fit. The linear fit has a slope of -9.7.

Here n is the minimum total number of the lepton, photon and quark fields carrying a finite fraction of the momentum in the particles A,B,C and D. The scaling law is universal for the hard processes at fixed CM angle. It is based on the dimensional analysis of the lowest order perturbative QCD scattering amplitude [31]. The scaling law fits the data very well (Figure 4.3).

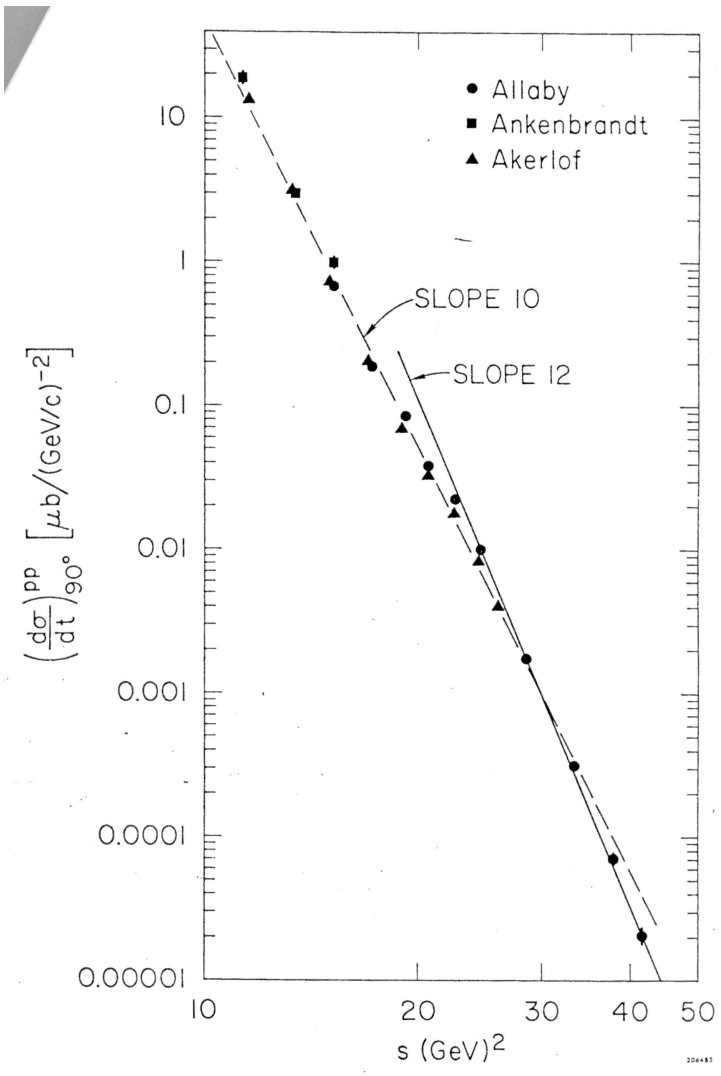

Figure 4.3: Elastic pp cross section at 90° CM angle. The dashed line is a linear fit with a slope of -10, according to the dimensional scaling law. The solid line is a linear fit with a slope of -12, according to the constituent-interchange model.

A class of Lowest Order perturbative QCD (LO pQCD) Feynman diagrams is used in the dimensional analysis of the scattering amplitude. An example of the LO pQCD diagram is shown in Figure 4.4(a). This is the lowest order of the quark exchange diagram. In the quark exchange diagram (Figure 4.4(a)) the momentum transfer occures when hadrons exchange quarks. There is an additional hard gluon exchange inside the out-going hadrons to preserve their structure. The other kinds of the LO pQCD mechanism are gluon exchange and quark annihilation.

A distinctive feature of the LO pQCD diagrams is the exchange of five hard gluons inside the interacting hadrons. These diagrams are also called the irreducable pQCD diagrams. The cross section for the wide-angle elastic pp scattering, calculated in pQCD, has the strong s^{-10} dependence.

A different scattering mechanism was proposed by Landshoff. The momentum transfer in the Landshoff type process (Figure 4.4(b)) is carried out via exchange of hard gluons among the quarks in participating hadrons.

The Landshoff mechanism has a less strong dependence for the proton-proton scattering $\frac{d\sigma^{90^\circ}_{CM}}{dt} \sim s^{-8}$ [32]. In the model the hadrons scatter at large angles by independent scatterings of the constituents of one hadron on the constituents of another hadron [33]. It was argued that the energy dependence of the amplitude is coming from the condition that the final momenta of the constituents must be aligned to preserve the hadrons [31]. The smaller power of the s-dependence of the cross section means that the Landshoff mechanism should dominate in the scattering. However, the predicted energy dependence did not agree well with the available data [32].

It was shown [34, 35] that in the Landshoff mechanism it is necessary to take into account

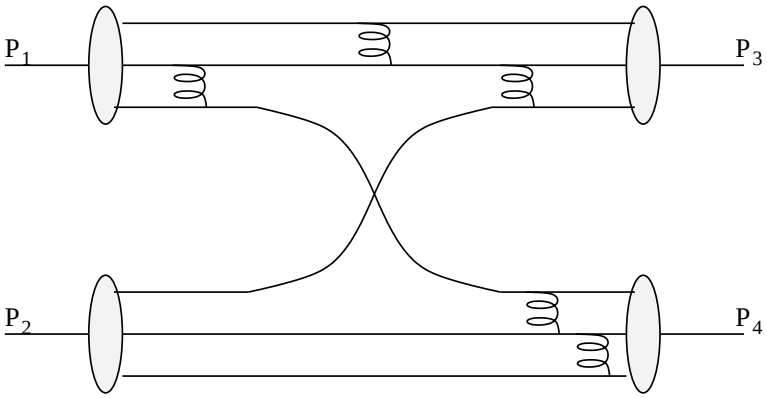

(a) The scattering via the Quark Exchange mechanism.

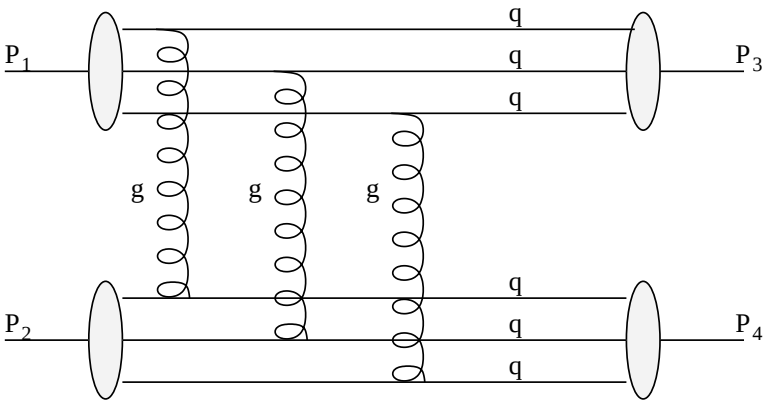

(b) The scattering via Landshoff mechanism.

Figure 4.4: Examples of the Feynman diagrams, describing the proton-proton scattering mechanisms in the leading twist.

radiative corrections. In the scattering the colored objects (quarks) are accelerated while turning. The acceleration is accompanied by the soft gluon radiation. It is analogous to the bremsstrahlung radiation in QED. If gluons are not re-absorbed, the reaction is inelastic.

The radiative corrections are needed to account for the soft gluon radiation. The corrections ('Sudakov' factors) include the sum over the soft gluon exchange diagrams inside the protons. The radiative corrections were originaly calculated in QED for electron scattering by Sudakov [36]. The corrections for hadron-hadron scattering were calculated by Mueller (meson-meson scattering) [35] and Sterman *et al* (meson-meson and baryon-baryon scattering) [34]. The 'Sudakov' factors tend to suppress the cross section for the hadron-hadron scattering. For a restricted interval in s, the suppression brings the power law for the Landshoff mechanism close to s^{-10} for pp wide-angle scattering.

In pQCD type of scattering the quarks are close together and form a local color singlet. The color singlet does not need to radiate gluons. There is no 'Sudakov' suppression in this case.

The pQCD processes and the Landshoff mechanism with radiative corrections, both, have a very strong s-dependence of the cross section. The cross section dependence is not a pure power law. The existing data [37] show cross section oscillations around the s^{-10} curve (Figure 4.5).

There are several theoretical works explaining the oscillations of the hadronic cross section. Bordsky and de Teramond [11] argue that the oscillations appear when the new channels become available in the hadronic scattering. It happenes when the CM energy becomes large enough to produce new resonances, for example, a ϕ-meson or J/ψ-meson. The prediction of this model [11] is shown in Figure 4.5.

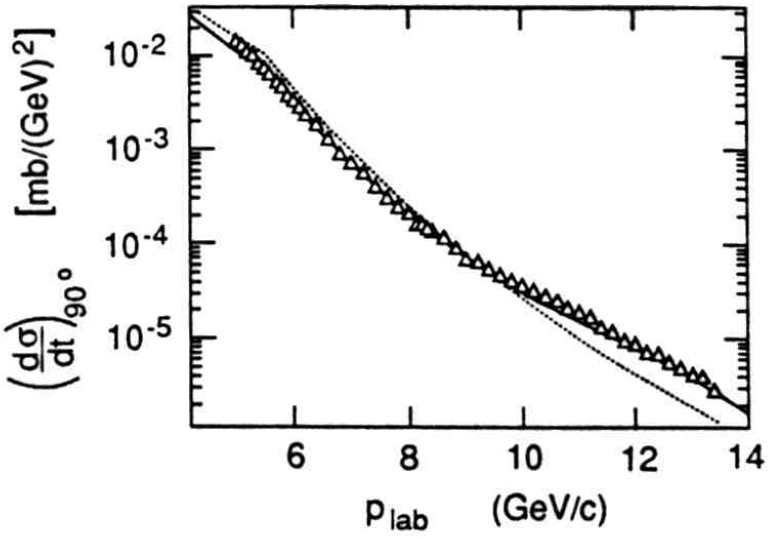

Figure 4.5: The *pp* elastic cross section at 90° CM angle by Akerlof *et al* and the prediction of the Brodsky-de Teramond model (solid line).

Ralston and Pire [12] propose that the cross section oscillations occur because of the interference between the pQCD and the Landshoff processes, modified by the radiative corrections. Ralston and Pire introduce the amplitude as a sum of these.

$$M = M_{QCD} + e^{i\delta + i\phi(s)} M_L \tag{4.3}$$

Here $\phi(s)$ is the energy depended phase and δ is uncalculable energy-independent parameter. The comparison of this model with experiment [12] is shown in Figure 4.6

These models explain well the oscillations of the cross section around the power law curve predicted from the dimension scaling. The dimensional scaling law is a consequence of the dominance of the exchange type processes.

The experimental results by A.S.Carroll *et al* [38] indicate that the quark exchange dominates the gluon exchange and annihilation amplitudes at 90° CM scattering. They

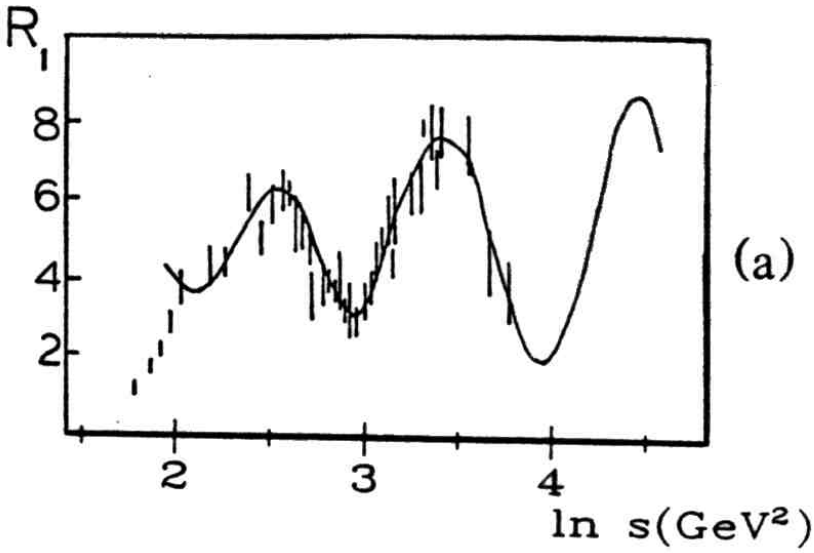

Figure 4.6: Energy dependence of the R_1(s) ratio in Ralston-Pire interference model. R_1(s) is the ratio of the cross section to the quark-counting prediction (s^{-10}).

quote the ratio of the $p\bar{p}$ to pp cross section to be $\sim 1/40$ at 90° CM. The quark exchange is allowed in pp scattering and not allowed in $p\bar{p}$. Similarly the K^-p to K^+p ratio is $\sim 1/12$ [38]. Again the quark exchange is not allowed in the former and allowed in the later. Other experiments [39] confirm the assumption of the quark exchange mechanism dominance.

4.1.2 Point Like Configurations

The scattering via the pQCD type mechanisms possesses an exciting feature. There is exchange by hard gluons inside of the out-going hadrons (Figure 4.7). Such exchange brings quarks close to each other. The characteristic distances are of the order of $\sim \frac{1}{Q}$ according to the uncertainty principle. This object has a size smaller than a usual hadron. It is called a Point Like Configuration (PLC).

The PLC is formed only in the scattering via pQCD diagram. In the Landshoff type

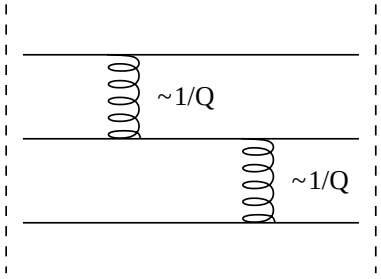

Figure 4.7: A piece of the quark exchange diagram.

process the quarks of the *different* protons are brought close together by the hard gluon exchange. The quarks of the *different* hadrons are at the distances of $\sim \frac{1}{Q}$. It means that the interaction region is small. However, inside the out-going hadrons quarks do not have to be at small distances and PLC is not formed.

From geometrical considerations a PLC component of the hadron wave function interacts with the surrounding medium less than the sum of all the components of the hadron wave-function (Figure 4.8).

(a) Normal size proton passing through the nucleus.

(b) PLC passing through the nucleus.

Figure 4.8: A qualitative representation of the difference in the cross section due to the difference in size.

An analogous effect is known in QED. It was observed by Chudakov in 1955 [40]. Conversion of the high energy photons was studied in emulsion films. Formed electron-positron pairs didn't leave a trace at the conversion point but were seen after they pass some distance

through the film.

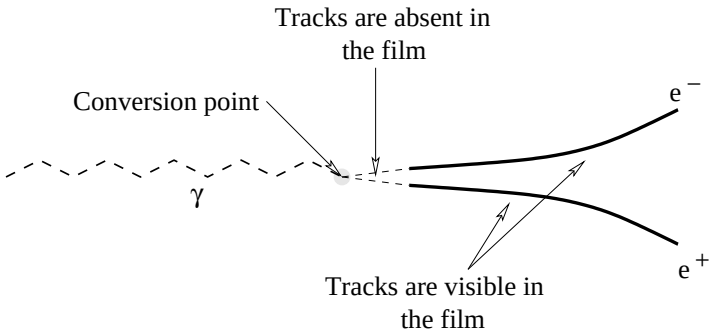

Figure 4.9: An example of the Chudakov effect in the emulsion film.

This effect is attributed to the small transverse separation of the e^-e^+ pair. The electron and positron charges are screened. The dipole moment of the pair is small. In the limit of the transverse separation of the pair $\rightarrow 0$ the interaction with surrounding atoms vanishes. The e^-e^+ pair does not leave a trace in the film. As the particles drift apart they interact with atoms separately. The tracks become visible.

Similarly, the color neutral PLC has a small color dipole moment. When it travels through the nucleus, PLC's interaction with the nucleus is suppressed. However, PLC expands as it propagates. At some point PLC reaches the size of a normal hadron.

The mechanisms of expansion are discussed in theoretical papers [41]. In one naive picture the transverse separation between the quarks is proportional to the distance from the interaction point of the PLC $D_t \sim z(\frac{E}{m})^{-1}$. The length at which the PLC reaches the hadron size is then $l_h = \frac{E}{m_h}$. In the other approach, called "quantum diffusion", Strikman *et al* [41] suggest that $D_t \sim \sqrt{z}$. In this model fluctuation to the normal size occurres over $l_h = 2P_h/(M^2_{PLC} - M^2_h)$. Here P_h and M_h are the momentum and the mass of the hadron. The M_{PLC} is the estimate of the mass of the PLC.

The cross section of the PLC-nucleus interaction is a function of the transverse size of the

PLC. Calculations of the nuclear transparency show the dependence on the PLC-expansion models [6].

Independent of the expansion mechanism, the existance of the PLC changes the energy trend of the nuclear transparency. Brodsky and Mueller [5] proposed to use a nucleus as a filtering medium to investigate if PLCs are created in the hard wide-angle scattering.

4.1.3 Color transparency

Suppression of the interaction in the nucleus because of the small size of a PLC modifies the nuclear transparency,an effect reffered to as **color transparency**. The **color transparency** was extensively studied theoretically over the last 15 years and there were five experiments that investigated CT.

There are requirements for existance of **color transparency** [7].

- A PLC is formed in a high-momentum-transfer reaction
- There is no or reduced interaction with the PLC

One can see that these requirements are tied to the existance of the PLC and its time evolution. The PLC starts expanding after being created in hard wide-angle scattering. The expansion rate of the PLC depends on the CM energy. A PLC, created in the interaction with nucleus, can expand to the size of a hadron before it leaves the nucleus. From this point on it interacts with the nucleus as a hadron. The transparency depends on the path over which the particle interacts as PLC, on the path where it interacts as a hadron and on the type of the hadron from which PLC is created. The transparency then changes with CM energy of the interaction, hadron type and the nucleus size.

Color transparency is defined through the quasi-elastic and elastic cross sections [13].

$$T = \frac{1}{Z} \frac{\frac{d\sigma_{hp}}{dt}(nucleus)}{\frac{d\sigma_{hp}}{dt}(elastic)} \tag{4.4}$$

This is the transparency of a target nucleus of charge Z to a beam hadron h.

Color transparency is usually compared to the transparency calculated using the Glauber method [42] (App. C).

The transparency, within the Glauber method, is independent of CM energy for the beam energies larger the 5GeV [8]. The deviation of the transparency from the Glauber energy dependence is predicted by **color transparency** due to the creation of a PLC.

The experiment E834 was the very first to study the **color transparency** [13]. It was conducted at the Alternating Gradient Synchrotron of the Brookhaven National Laboratory. It was a two arm detector. One arm of the apparatus had a magnetic spectrometer. It measured the momentum of the scattered protons. In another arm, there was a set of proportional chambers that measured the trajectories of the particles opposite to spectrometer.

The measurement was performed on several nuclear targets - H, Li, C, Al, Cu, Pb. The incident proton momenta were 6, 10 and 12 GeV/c. The experimentaly determined nuclear transparency is presented in Figure 4.10. In the absence of CT the Glauber model predicts almost constant transparency.

For example, for p(C,2p) reaction, the Glauber level is ~ 0.2 [9]. The expected behaviour of the **color transparency** is a smooth rise with energy [41]. The transparency in Figure 4.10, in contradiction, has a drop at 10 GeV/c. The fall off continues up to 12 GeV/c. A number of different models [10, 11, 12, 43] were proposed to explain the transparency

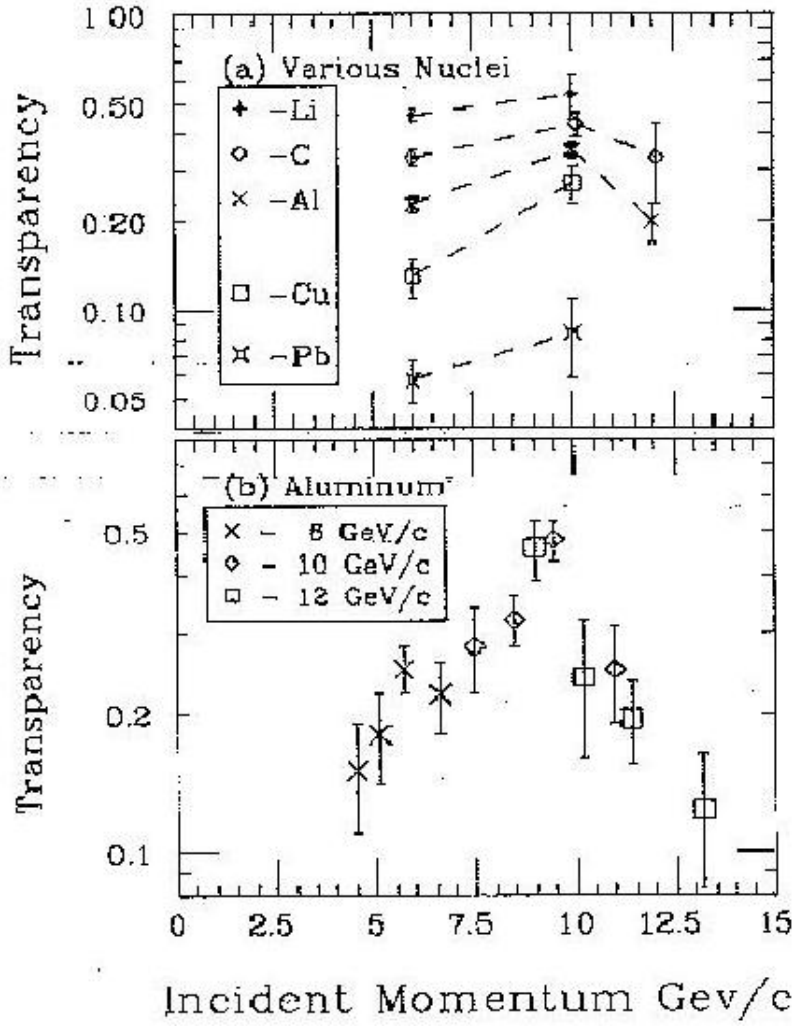

Figure 4.10: Transparency reported by E834.

reported by E834. Several of them [11, 12] predict the increase of the color transparency at about 16GeV/c.

The second experiment NE18 was performed using the electron beam at SLAC [44]. It studied the transparency using (e,e'p) reaction. The transparency was defined as a ratio of the experimental cross section for the nuclear target to the calculations of the nuclear cross section using the Plane Wave Impulse Aproximation.

The momentum transfered (Q^2) ranged from 0.64 $(GeV/c)^2$ to 8 $(GeV/c)^2$. The momentum transfer takes place via the virtual photon exchange between the beam electron and the target proton. The transparency is calculated for only one out-going proton propagating through the nucleus. In the E834, the transparency is calculated for three protons. There is one incoming proton and two out-going protons. The transparency in E834 experiment is, roughly speaking, the transparency of the NE18 to the third power. The results from the NE18 experiment [44] are presented in Figure 4.11. One sees no rise of the transparency that

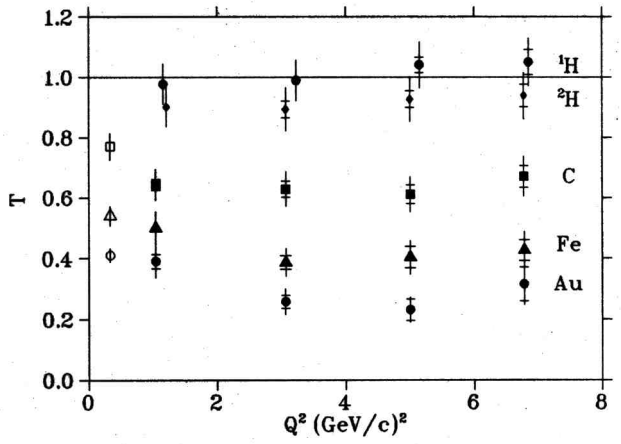

Figure 4.11: Transparency reported by NE18. The transparency is calculated for the (e,e'p) reaction.

could be associated with **color transparency** effect. However, in this region of Q^2 the pre-

dicted effect of **color transparency** is small [8, 45, 46]. Without the further investigation at higher Q^2 NE18 may not contradict to the existance of the **color transparency**.

The result of E834 was confirmed by our experiment E850 in 1994 and 1998 runs. We

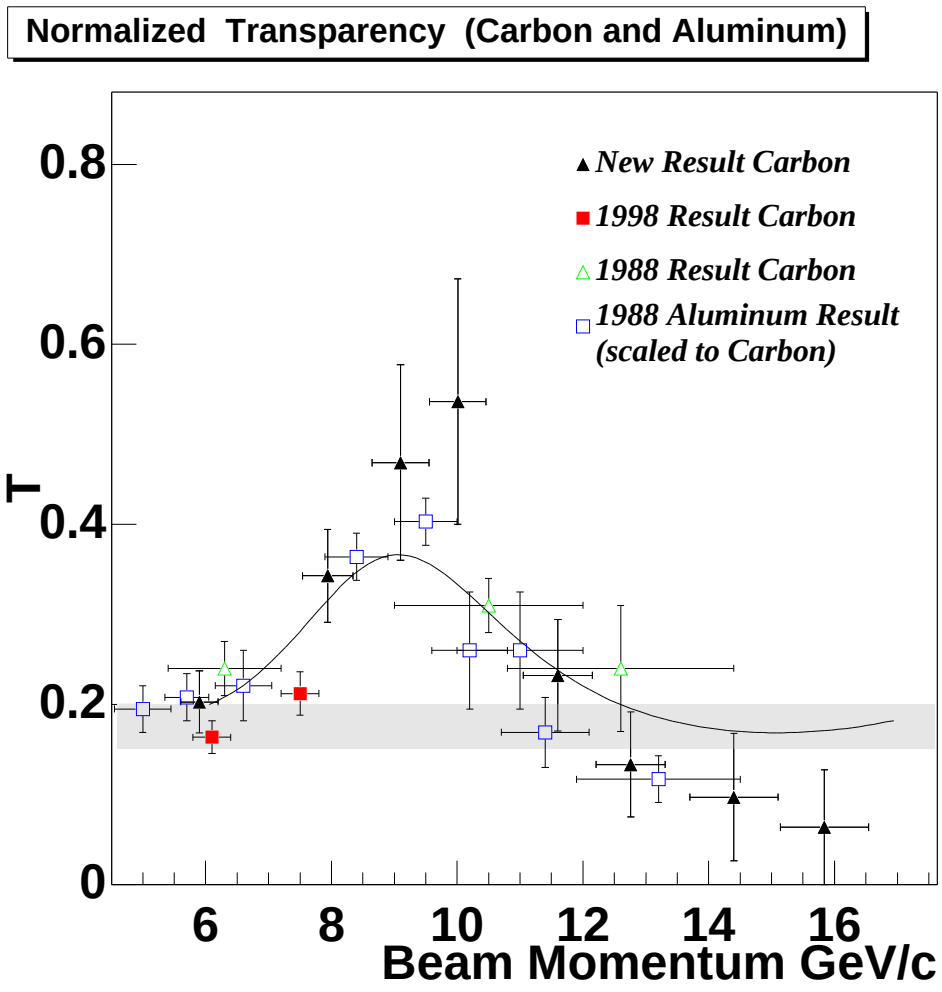

Figure 4.12: Transparency reported by E850. The solid curve corresponds to $R_1(s)$ function, proposed by Ralston and Pire and discussed in Section 4.1.1. The shaded band represents the Glauber calculations for Carbon [9].

studied the transparency of the Carbon nucleus. The energy range was extended up to 14.4 GeV. The analysis and extraction of the transparency can be found elsewhere [2, 3]. The results of the 1994 and 1998 runs are consistant and are in very good agreement with

the result of E834 [2]. The transparency grows with energy until 9 GeV. After 9 GeV it decreases and it reaches the Glauber level around 13 GeV (Figure 4.12).

The were other experiments that studied the nuclear transparency in reactions with large momentum transfer [14, 15].

4.1.4 Backward Neutron Production

The presence of the hard scattering is a part of a possible explanation of the another result from E850 experiment.

The analysis of the backward neutrons production on Carbon was carried out simultaneously with CT study [47]. Arrays of neutron counters were covering the large part of the backward hemisphere of the EVA spectrometer. The counters detected the backward neutrons in coincidence with two high P_T protons in the main spectrometer. The selection cuts did not constrain the events to be quasi-elastic.

A number of experiments with different beams, at different energies and on different targets studied the production of backward neutrons [18]. They reported an universal form for the momentum spectrum of the backward particles from inclusive reactions (Figure 4.13). The yield of backward particles was universal as well. About $(10 \pm 5)\%$ of events had coincident backward nucleons.

The form of the momentum spectrum in E850 experiment, within the uncertainties, is the same as in the other experiments (Figure 4.13). However, E850 reports a much greater yield of backward particles (Figure 4.14). The integrated neutron yield is about 30% per event in the acceptance of the detector. The extrapolation to the angular range of the other experiments increases the yield to $\sim 46\%$.

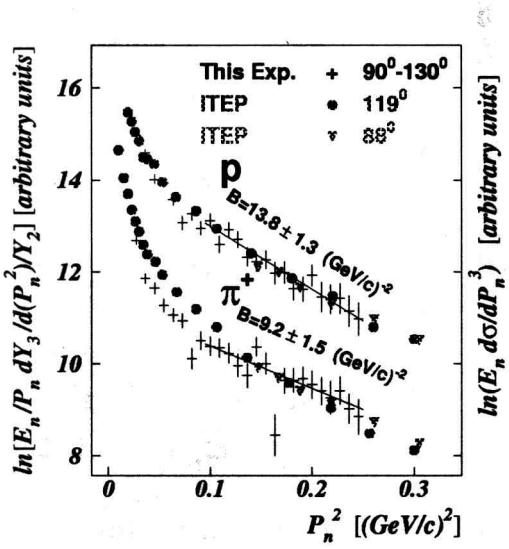

Figure 4.13: The backward neutron momentum spectrum.

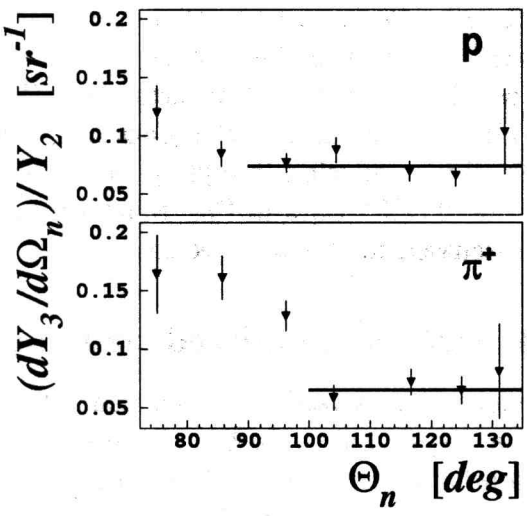

Figure 4.14: The yield of neutrons into the backward hemisphere.

The production of backward neutrons in quasi-elastic hard scattering can be discussed in light of the strong s-dependence of the hard quasi-elastic cross section. The cross section favors smaller s. The CM energy decreases when the incoming proton scatters from a forward-moving nuclear proton. The target nucleons, with large forward longitudinal momentum, are preferably selected in quasi-elastic wide-angle reactions. The large momentum component (above Fermi momentum) may be associated with the short-range correlated proton-neutron pair.

In the process of a nucleon knock-out, the nucleus recoils in the opposite direction. The recoil can be absorbed by a nucleus as a whole or by a correlated neutron partner. The correlated neutron emerges from the nucleus in the backward direction. A combination of the hard mechanism and the presence of the short-range correlations in a nucleus can provide a possible explanation for the large yield of backward neutrons in the quasi-elastic reaction.

However, the yield of neutrons was large not only for quasi-elastic events. It was a gross feature of the whole data sample. It was proposed that all events in the kinematic vicinity of the quasi-elastic events might have a hard scattering amplitude contribution in the cross section. Then, the same argument that was applied for quasi-elastic events should apply in the more inclusive case too.

An example of the inclusive reaction that can contribute to the data sample is discussed in the following section.

4.2 Pion production

One of the reactions that can contribute to the $pp \rightarrow ppX$ processes is the neutral pion production ($pp \rightarrow pp\pi^0$). The kinematics is still such that the final state protons have large transverse momentum. The pion does not have any kinematic constrains except for those imposed by the available phase space.

Under these conditions, there are four processes that can contribute to the pion production. These are 'star dust' type reactions, resonance decay, gluon bremsstrahlung and production of pions in the hard vertex. In the kinematic region of our detector little is know about these processes.

4.2.1 'Star dust' processes

In the 'star dust' process a virtual mesonic cloud of the nucleon plays an essential role [19, 20]. The proton scatters of the nucleon core with the pion as a spectator (Figure 4.15).

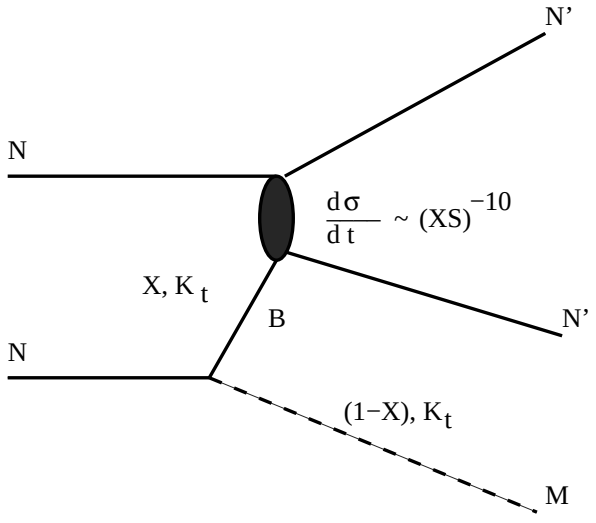

Figure 4.15: The 'Star dust' process diagram.

We cans see from the diagram what pieces are needed to calculate the cross section of the 'star dust' process. First, we need to know the probability of having a meson with the transverse momentum K_t and longitudinal momentum fraction (1-x) of the proton's momentum. This probability is called a splitting function $f_{\pi NN}$.

The second piece is the cross section of the $NB \to N'N'$ reaction. The cross section $\sigma_{NB\to N'N'}$ is the baryon-baryon cross section. The detailed calculation of the fragmentation cross section is provided in the Appendix D. The cross section of this process should be comparable to the hard two body elastic cross section.

It seems advantageous for the protons to scatter through the 'star dust' channel. During the fragmentation the pion takes away a fraction of the longitudinal momentum of the proton. It decreases the CM energy. The cross section increases because of the strong s-dependence. On the other hand form-factor and the nucleon structure function decrease the cross section near the endpoint.

In the reaction on the hydrogen target most of the 'star dust' cross section comes from the beam fragmentation kinematic region at $X_L < 0.95$.

4.2.2 Resonance production

A pion can be produced in pp scattering through the resonance formation and decay. For example Δ^+ can be formed in the pp scattering. The branching ratio for Δ^+ to decay into a nucleon and a pion is $> 99\%$. The products of the decay can be a proton and a π^0.

Very little data is available about resonance production in the kinematic region of interest. In this section, we provide the cross sections for several resonances, produced around 90° in the CM frame. We discuss the branching ratios for the $N^* \to p\pi^0$ resonance decay

mode.

A study of several N^* isobars was reported by Ankenbrandt *et al* [48] and Allaby *et al* [49]. The data of the reference [48] has the beam energy and the CM angle range the same as the ones used in E850 experiment. We summarize the cross sections in the table below (Table 4.1).

Values	$pp \to pp$	$pp \to pN^*(1238)$	$pp \to pN^*(1512)$	$pp \to pN^*(1688)$
Energy	6.07	6.08	6.08	6.08
-t,GeV^2	4.67	4.25	4.02	3.85
$\frac{d\sigma}{dt}$	$(3.2 \pm 0.1) * 10^{-3}$	$(4.0 \pm 2.0) * 10^{-4}$	$(6.4 \pm 0.8) * 10^{-3}$	$(8.0 \pm 1.0) * 10^{-3}$

Table 4.1: Cross sections(mb/GeV^2) of the Resonance production close to 90° in CM

To have a proper estimate of the cross sections for $pp \to pp\pi^0$, one has to take into account the branching ratios of $N^* \to p\pi^0$. The branching ratios make $\frac{d\sigma_{pN^*}}{dt}$ smaller than elastic cross section. For example, heavy N^* isobars decay into a $N\pi$ only in 50% of the cases. The rest of the decays go through $N\pi\pi$ or $N\eta$ channels.

Even in the case of a $N^* \to N\pi$ decay, the resulting nucleon can be a proton or a neutron. The ratio of $N^* \to p\pi^0$ to $N^* \to n\pi^+$ is the ratio of the Clebsh-Jordan coefficients. The isobar with the 1/2 isospin has a 2/3 probability of decaying through the $n\pi^+$ channel and 1/3 probability to decay through the $p\pi^0$ channel.

The cross sections for π^0 production through the decay of these resonances are less than the elastic pp cross section after all the factor are accounted for. The production via the light N(1238) resonance is suppressed by more than an order of magnitude. The cross section of the production through the heavier resonances is of the order of elastic cross section. There are contributions to the pion production cross section from the continuum

under the resonance peaks.

4.2.3 Direct production of π^0

There is one more possible mechanism of the pion production. It is the direct production in the vertex of the hard interaction (Figure 4.16). There are n=14 quark fields taking part

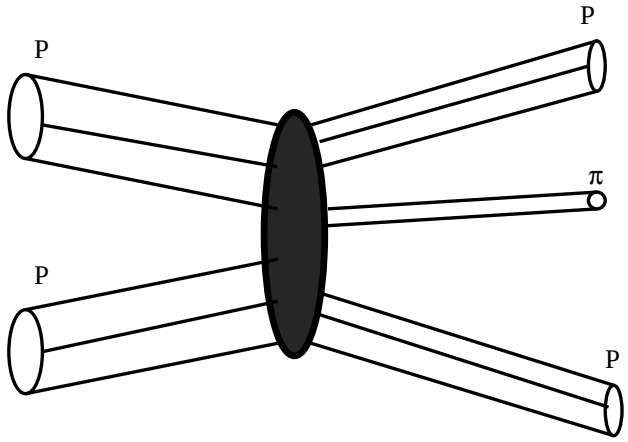

Figure 4.16: A diagram of the direct pion production in the hard vertex.

in hard interaction. According to the dimensional scaling law, the cross section of such process is

$$\frac{d\sigma}{dt} \sim s^{2-n} \sim s^{-12}. \tag{4.5}$$

This process is suppressed by two powers of s compare to pp elastic scattering. We are not aware of any data on $pp \to pp\pi^0$ with all three particles produced at wide angle in CM.

In the data of Abolins *et al* [50, 51] we see the regions where protons and pions where produced at large angle (90° CM). Unfortunately they present the integrated angular and momentum distributions. We are not able to conclude if they saw processes where all three final particles took part in the hard scattering.

4.2.4 Gluon Bremsstrahlung

A pion can be produced in the process of gluon bremsstrahlung by protons undergoing the hard scattering. In the wide-angle scattering quarks are accelerated in the direction transverse to their original direction of motion. The quarks are colored objects. Their acceleration is accompanied by the radiation of the color field - gluon. The analogy of this effect in QED is bremsstrahlung of the accelerating charged particle.

The gluon radiation by a proton is more complex than bremsstrahlung of a charged particle in QED. The proton is a composite system. There are three accelerated quarks inside the interacting protons in the leading order of the hard scattering amplitude. In Section 4.1 we discussed the leading diagrams for the wide-angle elastic scattering. In both processes the quarks are accelerated in the wide-angle scattering.

In the pQCD mechanism the quarks exchange the hard gluons (Figure 4.4(a)). The distance between the quarks is very small $\sim 1/Q$ as a result of hard scattering. The quarks screen one another's color fields. The radiation of color fields in the case of screened color charges is suppressed.

The scattering via Landshoff mechanism does not have the condition of the small inter-quark distances. The quarks may radiate gluons during the scattering. We discussed earlier (section 4.1) that the gluon radiation leads to the suppression of this diagram in elastic scattering.

However, we consider the case of the $pp \to pp\pi^0$ scattering. The radiation of gluons by quarks is allowed. The cross section for the Landshoff processes without the suppression of the gluon radiation is proportional to the s^{-8} for pp scattering. The exclusive selection of

the $pp \to pp\pi^0$ processes can lead to some suppression of the cross section. The Landshoff type scattering may be dominant for the semi-inclusive processes.

In the calculations of the Sudakov suppression in the Landshoff mechanism the fate of the gluons is not discussed after they are emitted and the process becomes inelastic. However, single gluons can not be seen in nature because they are colored objects. It is possible for gluons to softly re-interact with a proton in such a way that a single pion is produced. The kinematic characteristics of the emitted gluons may have an effect on the final state angular and momentum distributions of the pion. A single pion production by a gluon or a group of gluons without interaction with hadrons is prohibited because of the conservation of the isospin. Gluons have the isospin 0 and they can not produce the pion with the isospin 1.

The angular distribution of the bremsstrahlung radiation in QED is correlated with the direction of acceleration of the radiating particle. The radiation is directed along the momentum of the accelerated particle. It is, mostly, confined to the plane of the acceleration. The radiation is peaking at small frequencies with the consequent power law fall-off. The angular distribution of the gluon radiation is similar to the QED bremsstrahlung.

The relativistic protons have a small size in the scattering plane due to the Lorenz contraction. We speculate that the effect of the Lorenz contraction may modify the angular and momentum distributions of the gluon radiation. It is modified in the following way.

The component of the color dipole moment of the proton is small in the scattering plane because of the small transverse separation of the quarks. The radiation with the wave length larger than the transverse separation of the quarks is suppressed. It leads to the suppression of the small momentum part of the radiation spectra. The suppression of the

low momentum part of the spectra flattens the decrease of the momentum distribution.

In the future when we refer to the gluon bremsstrahlung, we imply that a pion is produced in the process of the soft interaction of the gluons with a proton. We speculate that the modified effect of the gluon radiation may be an explanation of the angular and momentum distributions that we observe for $pp \to pp\pi^0$ processes.

4.3 Conclusion

We presented a review of the hard scattering processes and described the phenomenological dimensional scaling law. The cross section of the hard interaction is proportional to the s^{2-n}, where n is the number of elementary fields that took part in the hard scattering.

We underlined the connection of the hard scattering amplitude to the existence of the PLCs (point-like configurations). The reduced interaction of the PLC with nucleus is one of the conditions for observation of the **color transparency** Phenomenon.

We discussed the possible explanation of the unexpected Backward Neutron Yield. The large yield is seen in the data of the E850 experiment. It is a gross feature of the wide class of inclusive processes.

We looked at some of the channels that can contribute to the inclusive spectra, namely $pp \to pp\pi^0$ process. The theoretical cross section for 'star dust' (proton fragmentation) reaction is provided.

We would like to make an emphasize on the mechanism of the pion production via gluon bremsstrahlung. The semi-inclusive $pp \to pp\pi^0$ reaction is inelastic. In the Landshoff type scattering, the radiation of the soft gluons is not prohibited anymore, as it was in the

case of the elastic scattering. The Landshoff type process has s^{-8} dependence of the cross section. It should dominate the 'star dust' and resonance decay mechanisms, that have s^{-10} dependence.

We will try to use the idea of the bremsstrahlung in the Landshoff type scattering to explain the observed effects for $pp \to pp\pi^0$ reaction in our kinematics.

Chapter 5

Data analysis

Introduction

In this chapter we describe in detail the analysis of our event sample.

In choosing this data sample, we were motivated by the results of the research on backward neutrons described in section 4.1.4. Malki *et al* [18] speculated that short range NN correlations, combined with a strong s-dependence of the underlying cross section for $pp \to ppX^0$ events on Carbon, may explain the anomaly in their distributions. We decided to investigate if indeed these events have a strong s-dependence in the cross-section.

This chapter is written in the following order.

We describe the event sample and the kinematics of the events in the section 5.1. A number of the distributions for our event sample is plotted for the pp scattering on Hydrogen. Hydrogen is a component of the CH_2 target. We explain the procedure of the Hydrogen signal extraction. A part of our analysis is performed with a tight cut on the mass of the missing particle. The discussion of the mass distributions for the $pp \to ppX$ reaction concludes the section 5.1.

The data analysis is covered in the sections 5.2 and 5.3.

In the section 5.2 we characterize the cross section of the $pp \rightarrow ppX$ reaction as a function of the variable X_L. X_L is a fraction of the total longitudinal momentum carried by the two out-going protons. In the limit $X_L \rightarrow 1$, the strong dependence of the cross section on the CM energy produces a shift in X_L distribution for the scattering on nucleus compare to the distribution on Hydrogen. We show and explain this shift.

In attempt to understand the s-dependence of the data sample, we study the ratio of the X_L distribution for Carbon to that of Hydrogen. We analyze the trend of the ratio and speculate about it's interpretation.

The inclusive differential cross section $\frac{d\sigma}{dX_L}$ is characterized as a function of $(1 - X_L)$ in the region of $X_L \sim 1$. This fit is based on the prediction of the cross section dependence for the hadronic fragmentation, discussed in section 5.2.4. We provide the power of the $(1 - X_L)^{\beta}$ polynomial fit and summarize the limitation of the fitting procedure.

In Section 5.3 we apply a strict cut to the data sample. It is a cut on the mass of the missing particle. The cut selects the events with a π^0 as an extra particle. The theory of the pion production is discussed in Section 4.2.

We see an almost flat dependence of the differential cross section on the square of the transverse momentum of the missing particle. In contrast, a variety of experiments on inclusive meson production see an exponential fall-off of the differential cross section.

We analyze the angular and momentum distributions and compare them with the ones generated using the Monte-Carlo program. The distributions we see in the data can not be explained by the known models described in Section 4.2. We propose an interpretation of this effect. We speculate that a bremsstrahlung by a proton, taking part in wide-angle scattering may explain the phenomenon in a restricted kinematic region.

5.1 Kinematics and extraction of hydrogen signal

In the first part (5.1.1) of this section we define the event sample for the analysis. The acceptance of the detector determines the kinematics of the collected events. We give the examples of the processes that can contribute to the data.

The section 5.1.2 is devoted to the procedure of the extraction of the Hydrogen signal. We used Carbon and CH_2 targets during the data acquisition. The distributions for the scattering on Hydrogen were obtained indirectly via the subtraction of the normalized distributions on the Carbon and CH_2 targets.

The calculation of the kinematic variables is explained in the section 5.1.3. The kinematics of the scattering on the nuclear target differ from the kinematics of the scattering on the proton at rest. The nucleons are in Fermi motion inside a nucleus. We discuss the Fermi momentum distribution in the nuclear target.

The section 5.1.4 has the analysis of the mass distributions for the missing particles. We study two types of the mass distributions - missing mass distribution and effective mass distribution.

5.1.1 Definition of the event sample

We study the reaction of the semi-inclusive pp scattering, $pp \rightarrow ppX$. The events in our data sample are defined by the acceptance of the detector. The schematic picture of the detector is given in Figure 5.1.

We define three different acceptances for the detection of the charged tracks. We refer to the them as $A_{P_T}(\Phi,\Theta)$,$A_{Charged}(\Phi,\Theta)$ and $A_{trig}(P_T)$.

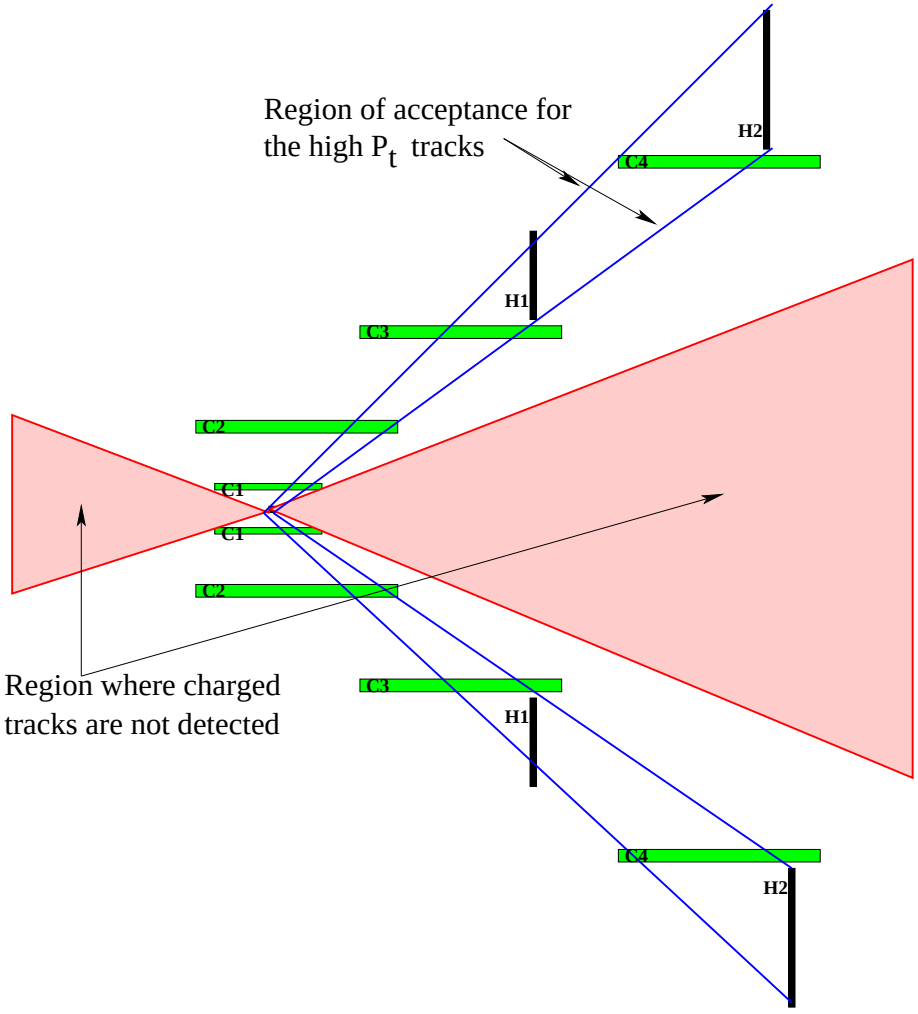

Figure 5.1: Schematic picture of the detector. The straw tube chambers are marked as C1-C4. The hodoscopes are marked H1 and H2.

The $A_{P_T}(\Phi, \Theta)$ is the acceptance of the detector associated with the momentum-angle reconstruction of the charged track. The detector has an aperture in the polar angle Θ for the reconstructed tracks. The aperture is marked as 'The region of acceptance for the high P_T tracks' in Figure 5.1. The charged particles that travel through this opening can be detected in four straw tube chambers and two hodoscopes. The $A_{P_T}(\Phi, \Theta)$ is defined over the 2π rad of the azimuthal angle Φ. In the Θ angle it is restricted to a slice of $\Theta \in (0.38; 0.5)$ rad.

The second acceptance function $A_{Charged}(\Phi, \Theta)$ refers to the detector coverage without momentum reconstruction. A charged particle can leave a trace in the C1 and C2 chambers (Figure 5.1). There is not enough information to reconstruct well all the parameters of the tracks that pass only through the C1 and C2 chambers. Nevertheless, we detect the presence of a charged particle. The acceptance for charged particles is 2π rad in the azimuthal angle Φ. In the polar angle we detect charged particles in the interval of $\Theta \in (0.351; 2.613)$ rad. The solid angle for detecting charged particles without momentum reconstruction is about 90%.

A third acceptance function, $A_{trig}(P_T)$, is associated with the trigger. Our trigger generally requires two charged back-to-back (in opposite azimuthal hemispheres) tracks that pass a P_T cut of the Level1 and Level2 triggers (section 2.2.2 and 2.2.3.1).

The global event sample that we study in the analysis contains events that have passed the trigger cut and have two back-to-back tracks with P_T above 0.73 GeV/c (condition is determined by $A_{trig}(P_T)$). We describe this final state kinematic region as in 'the vicinity of quasi-elastic scattering' because two back-to-back large P_T tracks look superficially similar to quasi-elastic scattering.

We also define a more restrictive two track data sample. It consists of the subset of events obtained with the requirement that no extra charged tracks are detected in the larger $A_{Charged}(\Phi, \Theta)$ acceptance. This final state can include the neutral particles.

The events in the two track data set, restricted by these cuts, have a missing mass in a wide range. It extends from the zero missing mass for elastic events to the missing mass of more than 1 GeV.

One of the reactions, in which the missing particle can be produced, is the decay of a baryon resonance. A light baryon resonance mostly decays through the $N\pi$ mode. For example, $\Delta(1232)$ decays into a nucleon and a pion in more than 99% of the decays. The $\Delta^+ - > p\pi^0$ decay would contribute to our data sample. In this example, the missing particle is a π^0.

The heavier resonances have such decay modes as $N\pi\pi$ and $N\eta$. In these cases the missing particle would be $2\pi^0$ and η correspondingly. The $N\pi$ decay constitutes only a small fraction for them.

5.1.2 Hydrogen signal extraction

We used two types of targets in the experiment. There was a Carbon target and a CH_2 target.

The extraction of the Hydrogen signal is performed in the following way. The distributions for Carbon and CH_2 targets are normalized with respect to the total beam and the proton density in the targets. We subtract the normalized distributions from the Carbon target from the distributions for the CH_2 target. The obtained distribution corresponds to the scattering of the beam particles on the proton of the Hydrogen nucleus.

The target configurations for the 5.9 GeV/c data sets (Table 2.4) are shown in Figure 5.2. Three targets were used in these runs, alternating the central target between Carbon

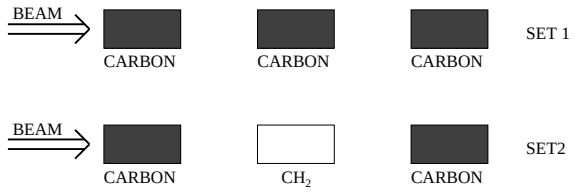

Figure 5.2: Target configurations for the analyzed data sample.

and CH_2. The Carbon in the first and third positions allowed us to normalize the beam exposure between the various run-sets.

The beam is attenuated in the targets. The coefficients of the beam attenuation depend on the target material. The coefficient of the beam attenuation on the Carbon target is 0.848. On the CH_2 target it is 0.961. The integrated proton flux on the targets is determined from the beam counter and taking into account the absorption for each target, we determine the average beam flux through each of the three targets.

We define the N_H to be the total number of events coming from the interactions on Hydrogen nucleus and refer to it as the Hydrogen yield. The Hydrogen yield is calculated using the following formula

$$N_H = (N_{CH_2} - B_{kin}\frac{F_{tgt}^{CH_2}}{F_{tgt}^{C}}N_C) * .5 \tag{5.1}$$

The target coefficients F_{tgt} depend on the Avogadro number (N_A), Mole weight of the target (M), the number of protons in the molecule of the target (Z), target length (l) and the target nucleon density ρ. The kinematic coefficient B_{kin} depends on the incident beam

(B_{beam}) and the beam attenuation factor (B_{att}).

$$F_{tgt}^{C} = N_A \frac{\rho^C l Z^C}{M^C} \qquad B_{kin} = \frac{B_{beam}^{C} B_{att}^{C}}{B_{beam}^{CH_2} B_{att}^{CH_2}} \tag{5.2}$$

The ratio $\frac{F_{tgt}^{CH_2}}{F_{tgt}^{C}}$ is equal to 0.4535 for our target configurations. We use Equation 5.1 to define the carbon subtracted CH_2 distributions, equivalent to distributions associated with a Hydrogen target.

5.1.3 Kinematic variables in the analysis

In this section we discuss the kinematic variables that are used in the analysis. The kinematics of the events in our data sample are rather simple. We have a beam of known momentum. It scatters off the targets. The target nucleon can be at rest (in hydrogen nucleus) or it can be moving (in carbon nucleus) with some momentum distribution.

The nucleon momentum distribution is characterized with a relativistic nuclear momentum distribution function. It specifies the differential probability density per unit four-momentum to observe a nucleon with a given momentum and energy.

The nuclear momentum distribution is usually presented as a function of the transverse and longitudinal components of the nuclear momentum. A recent parametrization of a spherically-symmetric carbon nuclear momentum distribution by Ciofi degli Atti *et al* [52] is used in the analysis of **color transparency** in our experiment [2].

In contrast to the distributions obtained with Hydrogen targets, missing final state momentum distributions measured with Carbon targets are smeared by motion of the target nucleon (Fermi-momentum). The motion of the struck nucleon in the nucleus is not directly observable.

The kinematics of the 'two-track' events in the analysis are determined by the acceptance of our detector. The two protons with large transverse momentum are detected in the spectrometer. The acceptance for these protons is A_{P_T}. We calculate the momentum of each proton $\vec{P}_i$. There may be any number of the neutral particles produced in the process. We do not detect them. They are denoted as missing particles. These particles have a total missing momentum and energy assigned to them.

The schematic diagram of the process is provided in Figure 5.2.1. There are three vectors

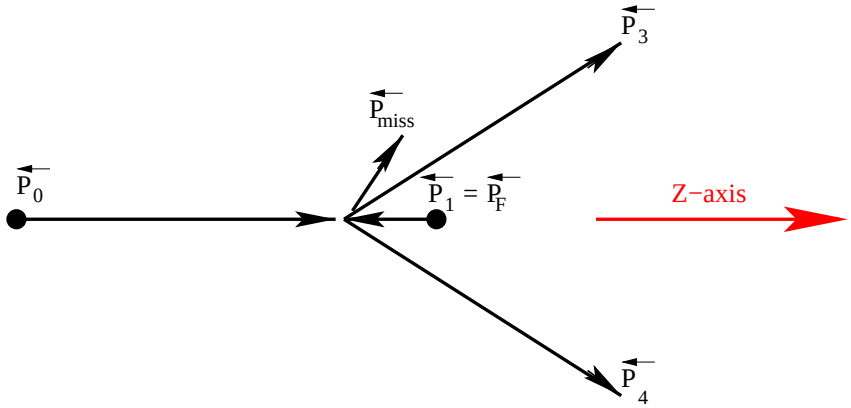

Figure 5.3: Definitions of the kinematic variables.

of the four-momentum that we know. These are $\hat{P}_{inc}$, $\hat{P}_3$ and $\hat{P}_4$. We calculate the missing variables using the following formulas

$$\vec{P}_{miss} = \vec{P}_0 - \vec{P}_3 - \vec{P}_4 \tag{5.3}$$

$$E_{miss} = E_0 + m_p - E_3 - E_4 \qquad m_p = 0.938$$

$$M^2_{miss} = E^2_{miss} - \vec{P}^2_{miss}$$

We assign index 4 to the proton with larger P_T. The proton with smaller P_T gets index 3.

In the case of quasi-elastic scattering the target nucleon has the momentum $\vec{P}_F$ and the energy E_F. They are related to the missing variables.

$$E_F = m_p - E_{miss} \qquad \vec{P}_F = -\vec{P}_{miss} \tag{5.4}$$

All the variables, that we use in the analysis, can be calculated using the three known four-momenta $\hat{P}_{inc}$, $\hat{P}_3$ and $\hat{P}_4$.

5.1.4 The analysis of the mass distributions

In the first part of this section we discuss the missing mass squared distribution for the inclusive reaction $pp \to ppX$. The distribution extends from the $M^2_{miss} \sim 0$ to the $M^2_{miss} \sim 1GeV^2$, where it is cut off by the acceptance of the detector.

The effective mass distributions are studied in the second part of the section. They are obtained for a semi-inclusive case of a single pion production.

5.1.4.1 The missing mass distributions

We use the formula of Equation 5.4 to obtain the missing mass squared distribution for our data sample. The event sample was defined in section 5.1.1. We plot the distribution of $\frac{dN_H}{dM^2_{miss}}$ for hydrogen events in Figure 5.4.

We see a significant peak in the missing mass distribution corresponding to the kinematic region of the elastic scattering and one pion production. The M^2_{miss} is equal to 0 for elastic events. For a missing π^0 the M^2_{miss} is equal to $0.018GeV^2$.

The region of the intermediate masses ($M^2_{miss} \in (0.0; 1.0)GeV^2$) does not have noticeable enhancements, that can be associated with meson resonances. We provide the general

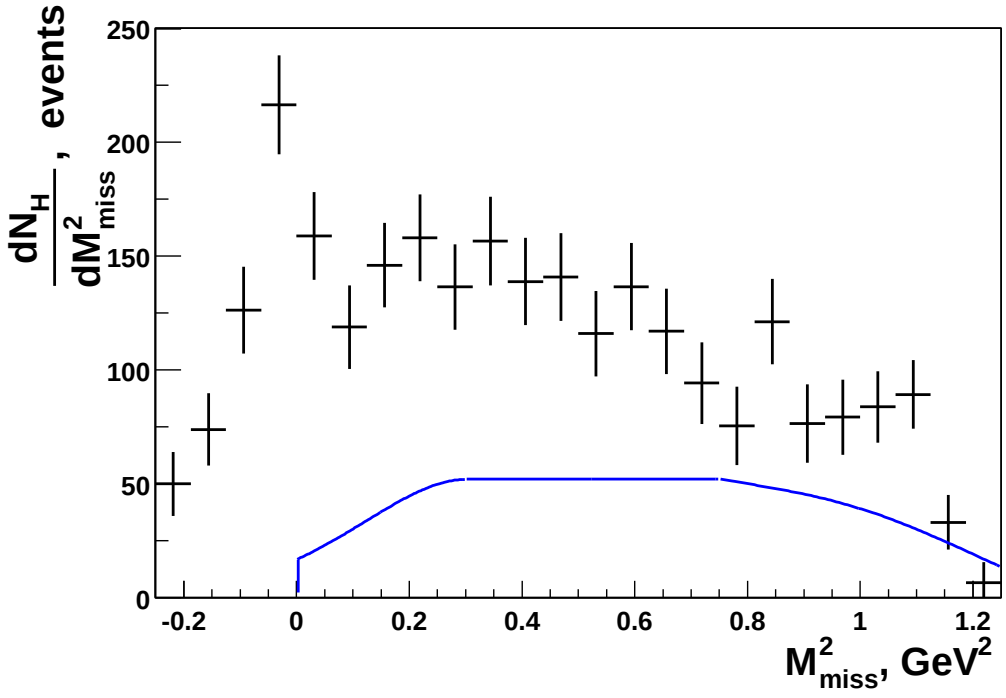

Figure 5.4: The $\frac{dN_H}{dM^2_{miss}}$ of the proton scattering on Hydrogen. The events have two and only two charged tracks. The Monte-Carlo generated acceptance for a flat distribution in $M^2_{miss} \in (0.0; 1.3) GeV^2$ is shown as a solid blue line.

information about the resonances that contribute to the featureless intermediate region of the missing mass distribution.

We do not expect a peaking in the missing mass spectrum of the non-resonant system of two π^0. The missing mass depends on the relative angle and momenta of the two pions.

$$M^2_{miss} = 2m^2_\pi + 2\sqrt{\vec{P}^2_1 + m^2_\pi}\sqrt{\vec{P}^2_2 + m^2_\pi} - 2\vec{P}_1\vec{P}_2 \tag{5.5}$$

The first meson resonance that decays to pions is the η ($M^2 = 0.3GeV^2$). It has about 70% probability of decaying through the neutral modes. The ρ/ω resonances have very close masses. The M^2 is $\sim 0.6GeV^2$ for both of them. The ρ decays into two pions ($\pi^+\pi^-$) at almost 100% rate. It does not contribute in our data sample. The ω meson has a branching ratio of about 8% for the neutral modes decay. The next existing resonance is η'. It has 14% branching ratio for neutral decays. The M^2 is $\sim 0.918GeV^2$ for this resonance.

In this inclusive region we may have contributions from the meson resonances, non-resonant multi-π^0 production and admixtures of the resonance+π^0.

A smooth extrapolation of the missing mass distribution in the intermediate region toward the edge of the detector acceptance indicates that there may be an enhancement in the region of the ϕ resonance mass. This resonance decays through the neutral mode with about 34% probability. It has a mass of 1.020 GeV. This mass corresponds to $M^2 = 1.04GeV^2$.

Such a large yield of ϕ-mesons is interesting to investigate. The ratio of the cross sections of the ρ/ω production to ϕ production is predicted by the Okubo-Zweig-Iizuka (OZI) rule [53] to be large. The production of strange and charmed resonances is suppressed by the factors ranging from 10 (ϕ decay) to a 1000 (J/ψ decay). The factors depend on the CM

energy. This predictions were confirmed in pp collisions at 24 GeV/c [54]. The production of the ϕ-meson was suppressed by a factor of 50 compare to the production of ρ/ω mesons. The strong suppression was also seen in inclusive meson production [54].

The breakdown of the suppression of ϕ production is predicted for exotic circumstances like the production of the quark-gluon plasma [55]. A large ϕ production in this case could also be an indication of an unusual interaction mechanism. Large ϕ production might, for example, suggest a role for gluon-gluon interactions in the scattering process [56, 57], leading to a decrease in the ρ/ϕ cross section ratio.

We do not speculate as to the mechanism of the ϕ production in this kinematic region although models have been introduced suggesting an important role for heavy quarks (s anc c) in the pp large angle scattering process near the threshold for quark-anti quark production [11].

5.1.4.2 The effective mass distributions

We look for the meson and baryon resonances using the effective mass distributions. The effective mass is calculated for the products of the resonance decay $pp \rightarrow pN^*$, $N^* \rightarrow p+\pi$. For example, for a decay $N^* \rightarrow p+\pi$ the effective mass is $M_{eff}^{N^*} = \sqrt{(E_p + E_\pi)^2 - (\vec{P}_p + \vec{P}_\pi)^2}$.

There are two ways to calculate the M_{eff} in the $P_1 + P_2 \rightarrow P_3 + P_4 + X$ reaction (Figure 5.2.1), we can construct either the invariant mass of P_3 and X or P_4 and X.

We do not measure the momentum and energy of the X particle. It is calculated indirectly (Equation 5.4). If X and P_3 are the products of the resonance decay, we calculate

the effective mass of the resonance M_{X+3} using the parameters of the P_4 (Figure 5.2.1).

$$M^2_{X+3} = (E_0 + m_p - E_4)^2 - (\vec{P}_0 - \vec{P}_4)^2 \tag{5.6}$$

In Figure 5.5 we plot the distribution of the effective mass for $pp \rightarrow pp\pi^0$ events. To select them we impose a cut on the missing mass to be small $|M^2_{miss} + 0.03| < 0.13$.

This cut is used to exclude the events with multiple pion production and to account for the effects of the fermi momentum for the scattering on Carbon. The cut $|M^2_{miss}| < 0.1$ can exclude the events with two or more π^0 produced in the scattering. The asymmetry in the missing mass cut appears because for the scattering on Carbon the fermi momentum decreases the missing mass. It is shifted toward the smaller values. We make the cut asymmetric to include the events from Carbon target with a shifted missing mass. The distribution of $M^2(\pi^0 P_4)$ is for the effective mass of a π^0 and a proton with larger P_T. A pion and a proton with smaller P_T are the products of the resonance decay with effective mass $M^2(\pi^0 P_3)$.

The resonances are formed in the hard scattering process in our kinematics. It is likely that a proton which is a product of an isotropic decay of the light resonance has a smaller P_T than the other out-going proton. The effective mass distribution of the π+Proton with smaller P_T should have the resonance peaks. As the mass of the resonance becomes large, the P_T can not be used to determine which of the protons is a product of the resonance.

We see little evidence for enhancements at the N^* masses of 1.44 GeV, 1.52 GeV and 1.68 GeV in the distribution for the $M^2(\pi^0 P_3)$ (Figure 5.5), corresponding to the masses of the resonances observed by Ankenbrandt *et al* [48].

The effective mass for a proton-pion pair in a non-resonant pion production depends on

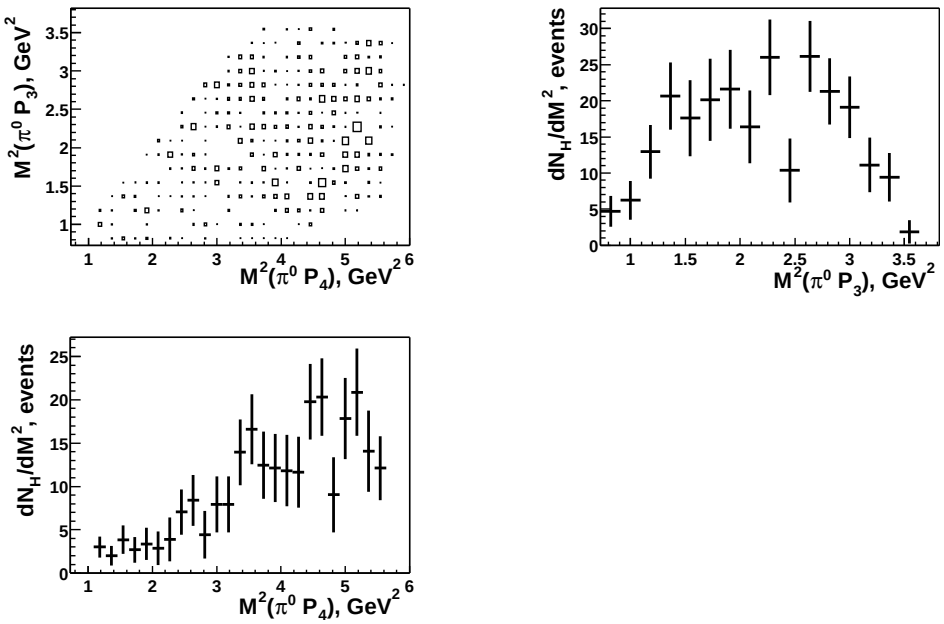

Figure 5.5: The effective mass distributions $M^2(\pi^0 p)$ for Hydrogen target (no elastic events).
TOP LEFT: Dalitz plot for $M^2(\pi^0 P_3)$ versus $M^2(\pi^0 P_4)$.
TOP RIGHT: Projection of the Dalitz plot on the Y-Axis. Distribution for $M^2(\pi^0 P_3)$.
BOTTOM LEFT: Projection of the Dalitz plot on the X-Axis. Distribution for $M^2(\pi^0 P_4)$.
The proton 4 has larger P_T than the proton 3.

the relative angle of the particles and their momenta.

$$M_{eff}^2 = m_p^2 + m_\pi^2 + 2E_pE_\pi - 2\vec{P}_p\vec{P}_\pi \tag{5.7}$$

The minimum M_{eff} is approximately equal to the proton mass.

The effective mass distributions for the carbon target are plotted in Figure 5.6. The

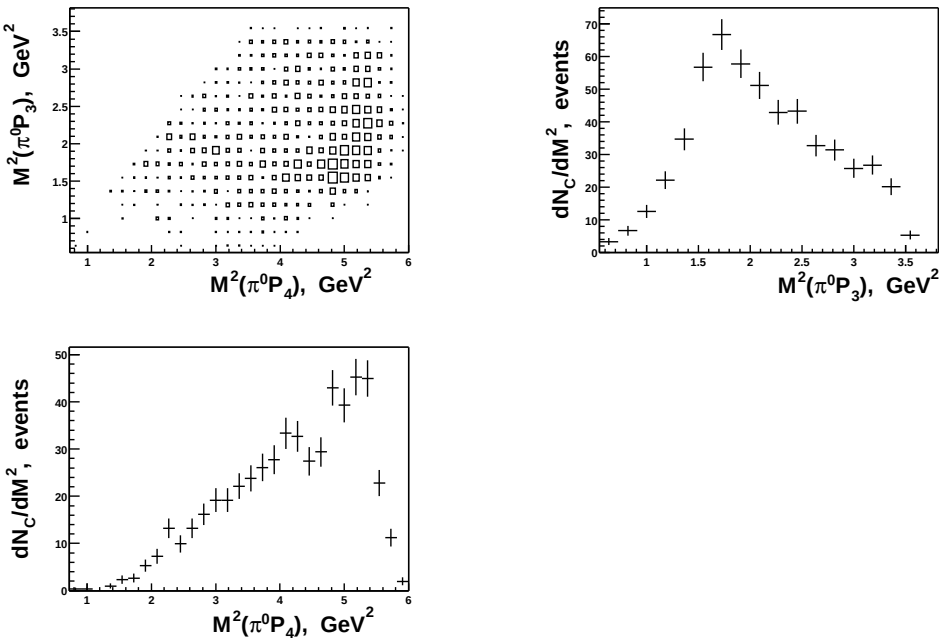

Figure 5.6: The effective mass distributions $M^2(\pi^0 p)$ for Carbon target (no quasi-elastic events).
TOP LEFT: Dalitz plot for $M^2(\pi^0 P_3)$ versus $M^2(\pi^0 P_4)$.
TOP RIGHT: Projection of the Dalitz plot on the Y-Axis. Distribution for $M^2(\pi^0 P_3)$.
BOTTOM LEFT: Projection of the Dalitz plot on the X-Axis. Distribution for $M^2(\pi^0 P_4)$.
The proton 4 has larger P_T than the proton 3.

distributions are smeared by the Fermi motion of the struck nucleon. In the case of the Carbon target it is difficult to make a conclusion about the presence of the resonance peaks in the data.

There is an enhancement at low effective mass ($M^2(\pi^0 P_3) \sim 1.7 GeV^2$) in the distribu-

tion for the Carbon target. The position of the enhancement corresponds to the mass of the $\Delta(1232)$ resonance. We do not know why such enhancement is present in the data on the Carbon target but it is absent in the data on the Hydrogen target.

We plot the effective mass distributions for the Monte-Carlo generated $pp \rightarrow pp\pi^0$ reaction in Figure 5.7. We generated the pion production via the resonance decay. The resonance was generated with the flat distribution for the M^2_{res} in the range of squared masses $M^2_{res} \in (1.0; 3.0) GeV^2$. In the simulation, the target proton had a momentum distribution for the longitudinal component. We used the parametrization of the momentum distribution function by Ciofi degli Atti *et al* [52].

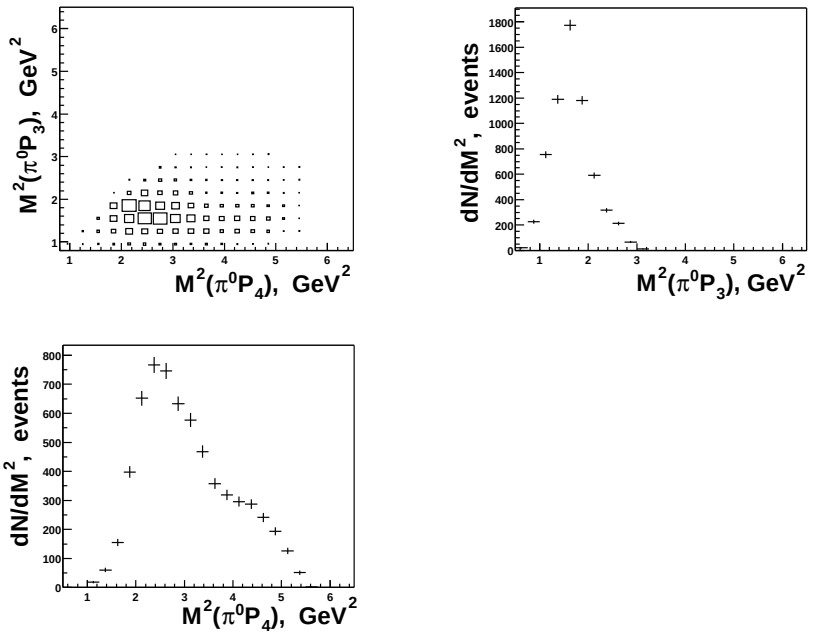

Figure 5.7: The effective mass distributions $M^2(\pi^0 p)$ for the Monte-Carlo simulated $pp \rightarrow pp\pi^0$ reaction.
TOP LEFT: Dalitz plot for $M^2(\pi^0 P_3)$ versus $M^2(\pi^0 P_4)$.
TOP RIGHT: Projection of the Dalitz plot on the Y-Axis. Distribution for $M^2(\pi^0 P_3)$.
BOTTOM LEFT: Projection of the Dalitz plot on the X-Axis. Distribution for $M^2(\pi^0 P_4)$.
The proton 4 has larger P_T than the proton 3.

5.2 The X_L distributions

In this section we analyze the semi-inclusive $pp \rightarrow ppX$ reaction using X_L distributions.

We define X_L in section 5.2.1 to be the fraction of incident momentum seen in the longitudinal component of the two-track final state. The shape of the X_L distributions for the elastic and quasi-elastic events is sensitive to the strong dependence of the elastic cross section on the CM energy. This can be observed as a shift in the X_L distribution for Carbon targets as compared to the corresponding distribution with Hydrogen targets. We explain this effect in detail in section 5.2.2.

The X_L-shift creates an excess, above some nominal level, in the ratio of the Carbon to Hydrogen distributions. We investigate the ratio of the X_L distributions for semi-inclusive scattering in the section 5.2.3.

In the last section (5.2.4) we explore the idea that most of the events in the data sample are the result of the hadronic fragmentation. The cross section of the fragmentation depends on X_L. We compare the behavior of our inclusive cross section with the prediction of the fragmentation model in the limit $X_L \rightarrow 1$.

5.2.1 Definition of X_L variable

We analyze the dependence of the differential cross section of the $pp \rightarrow ppX$ reaction (Figure 5.2.1) on the fraction of the longitudinal momentum that final state protons carry away. We introduce a variable X_L. It is the longitudinal momentum fraction of the two high P_T protons.

In the formula for X_L we use the proton momenta defined on the light cone ($P^+ =$

$E + P_Z$).

$$X_L = \frac{P_3^+ + P_4^+}{P_0^+ + P_1^+}. \tag{5.8}$$

The Z-axis in our experiment coincides with the direction of the beam. We always calculate X_L assuming that the target proton is at rest. We use this assumption for Carbon nucleus because we do not know the value of the Fermi momentum of the struck proton. When the beam scatters off a proton at rest the formula for X_L reduces to

$$X_L = \frac{E_3 + P_3^z + E_4 + P_4^z}{E_{beam} + P_{beam} + .938}. \tag{5.9}$$

We can express X_L in terms of the missing energy and momentum.

$$X_L = \frac{E_{beam} + P_{beam}^z + .938 - E_{miss} - P_{miss}^z}{E_{beam} + P_{beam} + .938} = 1 - \frac{E_{miss} + P_{miss}^z}{E_{beam} + P_{beam} + .938}. \tag{5.10}$$

5.2.2 The shift in X_L due to the s-weighting

In this section we analyze the influence of the strong s-dependence of the wide-angle scattering on the shape of the X_L distribution.

The value X_L is equal to 1 for elastic events but not for quasi-elastic events. There is a shift in the X_L distributions, calculated for the hard quasi-elastic scattering on the nucleus. Using conservation of energy and momentum we re-write Equation 5.8

$$X_L = \frac{E_{beam} + P_{beam} + E_F + P_F^z}{E_{beam} + P_{beam} + .938}. \tag{5.11}$$

Here E_F and $\vec{P}_F$ are the energy and momentum of the target nucleon. We see at once that X_L is equal to 1 for scattering on Hydrogen ($E_F = m_p = .938GeV$ and $\vec{P}_F = (0, 0, 0)$).

The nucleons in the Carbon nucleus are in motion, parametrized by a nuclear momentum distribution. In Ciofi's parametrization the shape of the nuclear momentum distribution is a combination of gaussian distributions [52]. The X_L distribution on Carbon is a convolution with the fermi momentum distribution. The result of the convolution is a smeared X_L distribution. Such a smearing leaves the center of the X_L distribution for the quasi-elastic scattering at $X_L = 1$. The shift in X_L distribution for quasi-elastic events comes from the strong s^{-10}-dependence in the cross section of the wide-angle quasi-elastic scattering.

This dependence favors the nucleons with a longitudinal component of the Fermi momentum along the beam direction. The CM energy for these nucleons is smaller than for the nucleons with smaller or negative P_F^z.

$$s = 2m_p^2 + 2E_0E_F - 2P_0P_F^z \simeq 2m_p^2 + 2E_0m_p - 2P_0P_F^z \tag{5.12}$$

The smaller s leads to a larger cross section for the nucleons with large P_F^z. The s-weighting of the cross section creates a shift of the X_L to the larger values.

We see this effect in the data. In Figure 5.8 we plot the $\frac{dN_H}{dX_L}$ for $pp \to ppX$ events on Hydrogen target. The enhancement at $X_L = 1$ is due to the elastic scattering. The fit of the distribution is shown as a solid line. The fitting function is

$$Fit = A(1 - X_L)^n + Be^{-\frac{(X_L - C)^2}{2\sigma^2}}. \tag{5.13}$$

The parameter C in the fitting function (Equation 5.13) corresponds to the center of the peak for elastic events. It is equal to one within the fitting error. The value of $X_L = 1$ for elastic events is smeared due to the resolution effects.

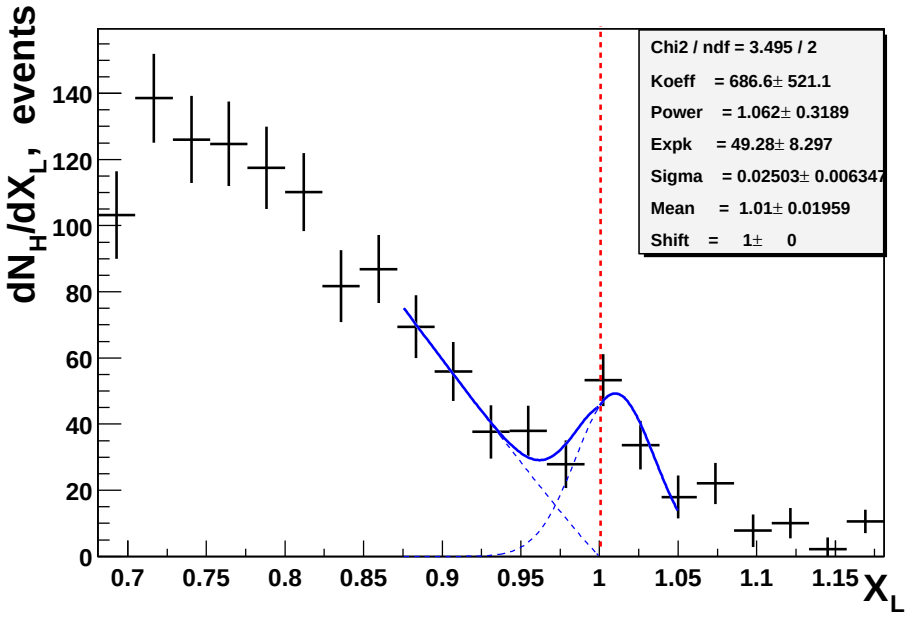

Figure 5.8: The X_L distribution for pp scattering on Hydrogen. The events with only two charged tracks are selected. The fitting parameters on the figure correspond to the parameters of the Equation 5.13: $Koeff$ corresponds to A, $Power$ is the polynomial power n, $Expk$ is the multiplier in front of the Gaussian B, $Sigma$ is the Half Width of the Gaussian - σ, $Mean$ is the center of the Gaussian peak - C.

The X_L distribution for Carbon is shown in Figure 5.9. We fit the $\frac{dN_C}{dX_L}$ to the same shape as for Hydrogen. There is a clear shift of the center of the quasi-elastic peak toward

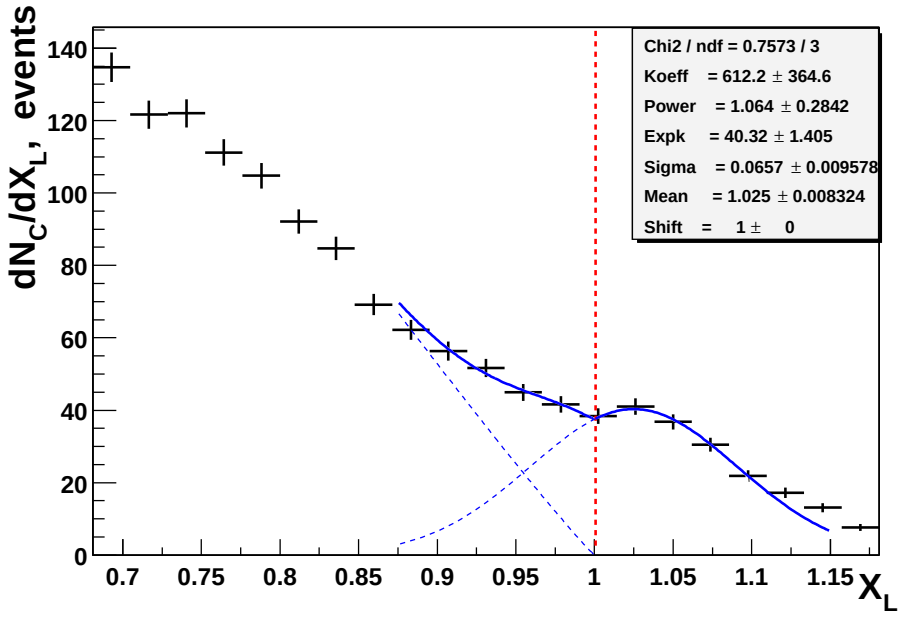

Figure 5.9: The X_L distribution for pp scattering on Carbon. The events with only two charged tracks are selected. The distribution is normalized to the beam on the Hydrogen target. The definitions of the parameters of the fit are the same as for the Hydrogen distributions.

the larger value of X_L. The parameter C is $C = 1.025 \pm 0.008$. We can use the approximate formula (neglecting E_F) for X_L for the quasi-elastic scattering to calculate the shift in the Fermi-momentum distribution due to the s-weighting.

$$X_L = \frac{E_{beam} + P_{beam} + E_F + P_F^z}{E_{beam} + P_{beam} + .938} \simeq \frac{2P_{beam} + .938 + P_F^z}{2P_{beam} + .938} \simeq 1 + \frac{P_F^z}{2P_{beam} + .938} \qquad (5.14)$$

Our fit for the Carbon quasi-elastic events has a peak at $P_F^z \simeq 0.3 GeV/c$.

The enhancement of the forward going nucleons in the conjunction with the presence of the short-range correlations in the nucleus is a proposed explanantion of the large yield of

the backward neutrons (section 4.1.4). We see the enhancement of the forward momentum for the quasi-elastic events in X_L distributions. It is clearly indicated by the X_L-shift.

This result validates the explanation of the large yield for the quasi-elastic events in Carbon. The large yield of backward neutrons is observed in a much wider class of events. The strong dependence of the cross section on the CM energy could be expected for these events.

5.2.3 The s-dependence of the inclusive events

The shift in X_L due to the strong s-dependence of the underlying cross section can be a tool to determine if there is a s-weighting of the events in the data sample. The X_L-shift creates an excess, above some nominal level, in the ratio of the Carbon to Hydrogen distributions.

We plot a ratio of the X_L distribution for Carbon to the X_L distribution for Hydrogen in Figure 5.10. We will refer to this ratio as T^{in}_{CH}. The T^{in}_{CH} is a transparency-like quantity, but it can not be directly related to the nuclear transparency. It is defined as

$$T^{in}_{CH} = \frac{6}{2}\frac{F^{H_2}_{tgt}}{F^{C}_{tgt}}\frac{dN_C/dX_L}{dN_H/dX_L}. \tag{5.15}$$

Parameteres F_{tgt} were defined in section 5.1.2, dN_H/dX_L is the Hydrogen yield and dN_C/dX_L is the Carbon yield per target proton, normalized to the beam on the Hydrogen target.

We see that in the range of X_L from 0.7 to about 0.9 the ratio is almost a constant. It is at the level of 0.3. There are changes in the ratio around the value of $X_L \sim 1$. The changes are due to the combination of the inclusive spectra with $(1 - X_L)^n$ dependence and the exclusive gaussian peaks.

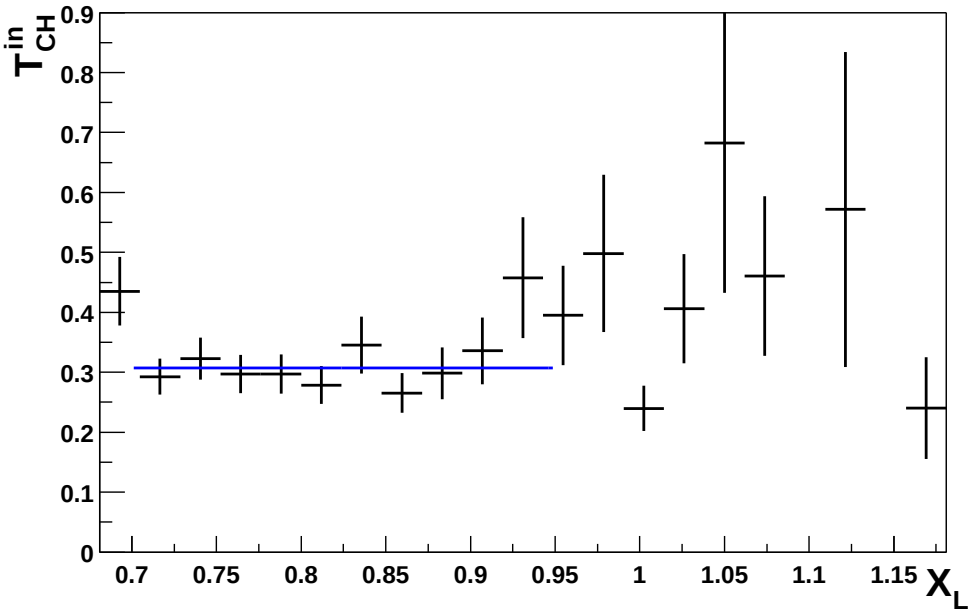

Figure 5.10: The ratio of the X_L-distribution on Carbon to the one on Hydrogen. The X_L-distributions are normalized to be per target proton.

The ratio of the distributions with a cut on the Θ_{miss} (polar) angle of the missing particle is shown in Figure 5.11. This Θ_{miss} cut ($cos(\Theta_{miss}) > .6$) effectively removes the elastic and quasi-elastic events. The sudden drop of the ratio at $X_L = 1$ is a consequence of the cut. The elastic events have an isotropic distribution in Θ_{miss} due to resolution effects only. There is a small number of elastic events left in the X_L distributions after this cut.

The distribution in Θ_{miss} for Carbon is not isotropic. The favoring of the forward moving nucleons in the hard scattering on Carbon creates an asymetry. Because of the s-weighting there are more events on Carbon with $P^z_{Fermi} > 0$. The P^z_{Fermi} is equal to $-P^z_{miss}$. The negative P^z_{miss} correspondes to the $cos(\Theta_{miss}) < 0$. Our cut removes the quasi-elastic events more effectively than the elastic events.

We see in Figure 5.11 that the shape of the inclusive X_L-spectra for Carbon and Hy-

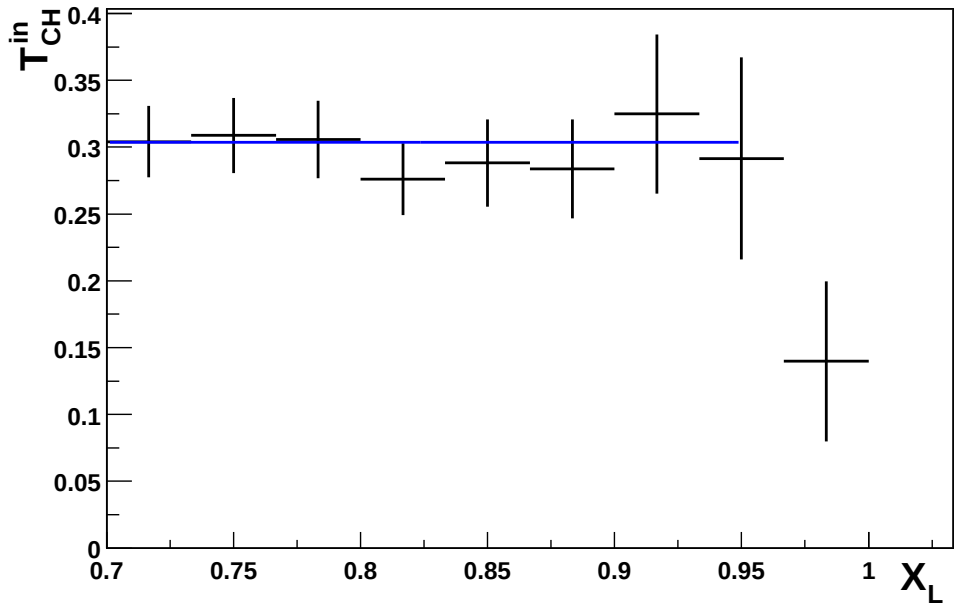

Figure 5.11: The ratio of the X_L distribution on Carbon to the one on Hydrogen. Elastic events are removed. The X_L-distributions are normalized to be per target proton.

drogen is very similar in the region of X_L from 0.7 to 0.95. The magnitude of the ratio is ~ 0.3.

To understand the magnitude of the T^{in}_{CH} ratio one has to investigate the degree to which allowing of the semi-inclusive reactions affects the Carbon yield. To explain this statement, we review the theoretical yield calculation for the quasi-elastic scattering. In the calculations, if the proton interacts with the nucleus, the reaction becomes inelastic. Inelastic reaction is not counted in the yield.

For the semi-inclusive $pp \rightarrow ppX$ reaction this approach does not work. We do not detect the neutral particles. The missing momentum can be a momentum of the X particle. It can also be a combined momentum of the particle X and the momentum lost during the final state interactions with nucleus. We can not know whether the protons interacted with

the nucleus.

Another effect that can change the T_{CH}^{in} ratio is the proton scattering on neutrons of the Carbon target. A low momentum π^-, produced in the $pn \to pp\pi^-$ reaction, can be absorbed by a nuclear proton. The pion is not observed in our detector and the event is added to the data sample. This process should increase the T_{CH}^{in} ratio. If the π^- is not absorbed, we may be able to see it in our detector and the event will be added to the sample of events with extra charged particles.

We are not aware of the existance of the calculations that take into account these effects. We quote the ratio of $T_{CH} = 0.304 \pm 0.011$. The interpretation of the ratio is non-trivial without the extensive theoretical calculations.

5.2.4 Dependence of the fragmentation cross section on X_L

In this section, we investigate the possibility that a large fraction of the inclusive $pp \to ppX$ events come from the fragmentation of the interacting hadrons. The 'two-track' data set was defined in section 5.1.1.

We perform a fit of the $\frac{dN}{dX_L}$ using the formula of Equation 5.13. The gaussian part of the fit is for fitting elastic and quasi-elastic events, smeared by the resolution. The polynomial part is for fitting the events with $(1-x)^n$ dependence in the cross section. This dependence can be associated with the processes of the hadron fragmentation.

In these processes the cross section factorizes into two parts. One part is a cross section of the scattering in the hard vertex. The other part, the hadron structure function G, comes from the fragmentation of the hadrons. The fragmentation cross section depends on the fraction of the longitudinal momentum that fragments carry away.

The extensive study of the fragmentation cross section was performed by Brodsky, Gunion *et al* [58, 59]. The cross section was shown to be $\sim (1-x)^m$. Here x is the fraction of the hadron's total longitudinal momentum carried by a fragment. The power m dependes on the details of the fragmentation process.

The dimensional counting rule is used [31] to determine the power m in the structure function $G_{a/A}$ for $x \to 1$. The $G_{a/A}$ is a structure function of the hadron A fragmenting into hadron a, which carries the fraction x of the A's longitudinal momentum.

$$G_{a/A} \sim (1-x)^{2N-1} \tag{5.16}$$

Here N is minimum number of quark spectators which are left behind after the fragmentation.

We can consider a process, at large energies, in which the proton fragments into a virtual baryon and a meson. The virtual baryon carries most of the proton's momentum $x_B \to 1$, as in the 'star dust' process [19]. The virtual baryon scatters of the target proton, producing two final state protons.

The differential cross section [58] is

$$\frac{d^2\sigma_{pp}(s)}{dxdt} \sim (1-x)^m \frac{d^2\hat{\sigma}_{Bp}(\hat{s})}{dxdt} \tag{5.17}$$

The $\hat{\sigma}_{Bp}$ is the cross section of the subprocess of a baryon-proton scattering. The $\hat{s}$ is the CM energy of the baryon-proton scattering. It is related to the s of the pp process.

$$\hat{s} \sim x * s, \qquad x \to 1 \tag{5.18}$$

The $\frac{d^2\sigma_{pp}(s)}{dxdt}$ can be re-written using the approximation for $\hat{s}$

$$\frac{d^2\sigma_{pp}(s)}{dxdt} \sim \frac{(1-x)^m}{x^l} s^{-l}. \tag{5.19}$$

The power l depends on the mechanism of the hard baryon-proton interaction.

We have to fit to the polynomial of the form $\frac{(1-x)^n}{x^l}$ to determine the correct power dependence of the fragmentation cross section. However, the fit to the polinomial $(1-x)^n$ provides the upper limit on the power n.

The given above example of the fragmentation process is one of the many processes contributing into our data sample. The distribution $\frac{d\sigma}{dX_L}$ is the inclusive distribution. It is a sum over many types of fragmentation, meson resonances production and baryon resonances production and decay. Many of these channels maybe suppressed in the limit of $x \to 1$. They may have different powers of n and l in the cross section. The power of the $(1-x)^n$ polinomial is a fit to the cross section for the cumulative $pp \to ppX$ process with two high P_T protons.

5.3 Characterization of the $pp \to pp\pi^0$ reaction

Here we describe the analysis of a 'two-track' subset of the inclusive data sample, described in section 5.1.1. We make a cut on the missing mass squared to select the events with at most one missing pion. The cut $|M^2_{miss} + 0.03| < 0.13$ is asymetric to account for the effects of the Fermi momentum distribution in carbon. This cut includes elastic and quasi-elastic events in the sample.

In section 5.3.1 we report a puzzling effect in the P_T^2 distribution of the missing pion.

This distribution for Carbon and Hydrogen targets is flat in a wide region. The expected behaviour of the missing P_T^2 distribution in inclusive pion production is an exponential fall-off. This has been demonstrated in many experiments.

We show that there is no 'flat-P_T^2' effect in the Monte-Carlo simulated dN/dP_T^2 distribution for the phase space, fragmentation process and isotropic resonance decay. We speculate that this effect may be related to the bremsstrahlung by protons in the wide-angle scattering.

In the section 4.2.4 we described the effect of gluon bremsstrahlung in the wide-angle scattering. We speculated that the low missing P_T^2 part of the bremsstrahlung spectra could be suppressed in the wide-angle scattering via Landshoff mechanism.

In the Landshoff type scattering, a proton is Lorentz contracted in the scattering plane. The physical picture of the Landshoff scattering was illustrated by Botts and Sterman [34] in the following way. Collisions between the constituents of the protons are likely to take place in the region of the space-time where the wave-functions of the protons are simultaniously non-vanishing. It is shown in Figure 5.12. The wave functions of the colliding protons are represented by a shaded disk perpendicular to the Z-axis. The unshaded disk, normal to the X-axis, represents the wave functions of the outgoing protons. The outgoing protons travel along the X-axis. The independent hard scattering in the Landshoff mechanism occure in the region of the overlap of two disks. The overlap region (blue brick pattern) has a shape of a 'cigar', which is normal to the scattering plane.

One can visiualize a Lorentz contracted proton as a 'cigar-shaped' object. The scattering plane coincides with the plane of the smallest section of the 'cigar-shaped' proton.

The transverse missing momentum has a component ($\vec{P}_{IN}$) in the scattering plane and

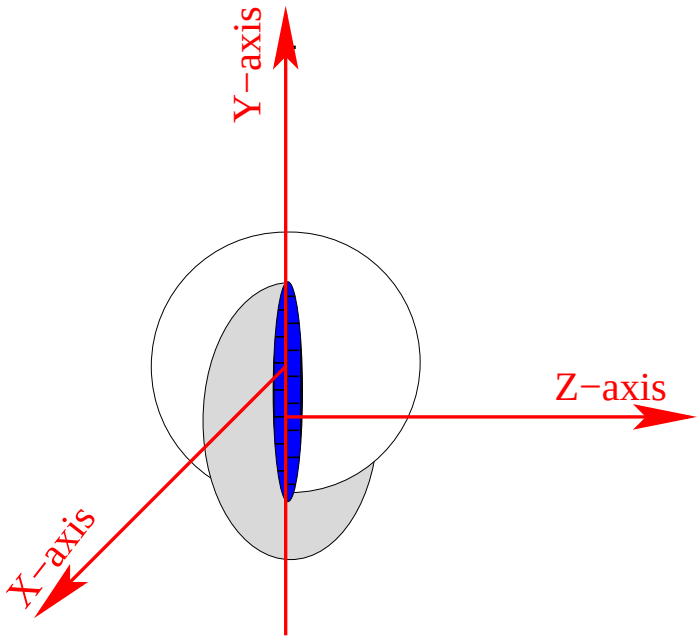

Figure 5.12: Physical picture for hadron-hadron scattering.

a component ($\vec{P}_{OUT}$) out of the scattering plane of the reaction.

$$\vec{P}_T^{miss} = \vec{P}_{IN} + \vec{P}_{OUT}$$

The suppression may occure for the soft part of the P_{IN} distribution. The 'cigar-shaped' protons have a small component of the color dipole moment in the scattering plane. The gluon (color field) emission could be suppressed in this plane. However, there would be no suppression out of the plane.

Based on these speculations, we may expect a dip in the P_{IN} distribution at small values.

We observe the suggested trends in the P_{IN} and P_{OUT} distributions of the missing momentum. The shapes of the distributions are not caused by the detector acceptance or the phase space effects. We observe that based on the momentum distributions for the

elastic events and Monte-Carlo simulations.

In sections 5.3.3 and 5.3.4, we characterize the $pp \to pp\pi^0$ reaction using the angular and momentum distributions of the missing particle.

The events are sorted into two sets using the cut on $M^2_{P_{3\pi^0}}$. One set of events has a low effective mass $M^2_{P_{3\pi^0}} < 2GeV^2$. The missing momentum for these events is mostly in the scattering plane. The distributions for low effective mass may be the result of the brehmsstrahlung in the Landshoff type scattering.

The second set of events with the high effective mass $M^2_{P_{3\pi^0}} > 2GeV^2$ has the missing momentum out of the scattering plane. For this set, other explanations may be more appropriate than the gluon bremsstrahlung idea. We propose the processes that can have the observed momentum distributions at the end of the section 5.3.

5.3.1 The flat dependence of the $\frac{dN}{dP_T^2}$ distribution

We study the $\frac{dN}{dP_T^2}$ distribution for the data set. In Figures 5.13,5.14 we plot this distribution for Carbon and Hydrogen targets.

We see a flat distribution for both targets. The enhancements at the very small P_T^2 are due to the quasi-elastic and elastic events for carbon and hydrogen correspondingly. The distribution is flat in a wide range up to values of $P_T^2 \sim .7(GeV/c)^2$.

We used Monte-Carlo to simulate the available phase space for the $pp \to pp\pi^0$ reaction. The P_T^2 distribution with restrictions of the phase space and the detector acceptance does not reproduce the flat dependence (Figure 5.15).

We use the cross section derived for the 'star dust' processes (section 4.2) in the Monte-Carlo simulations. It is applied to the $pp \to pp\pi^0$ events generated with the Monte-Carlo

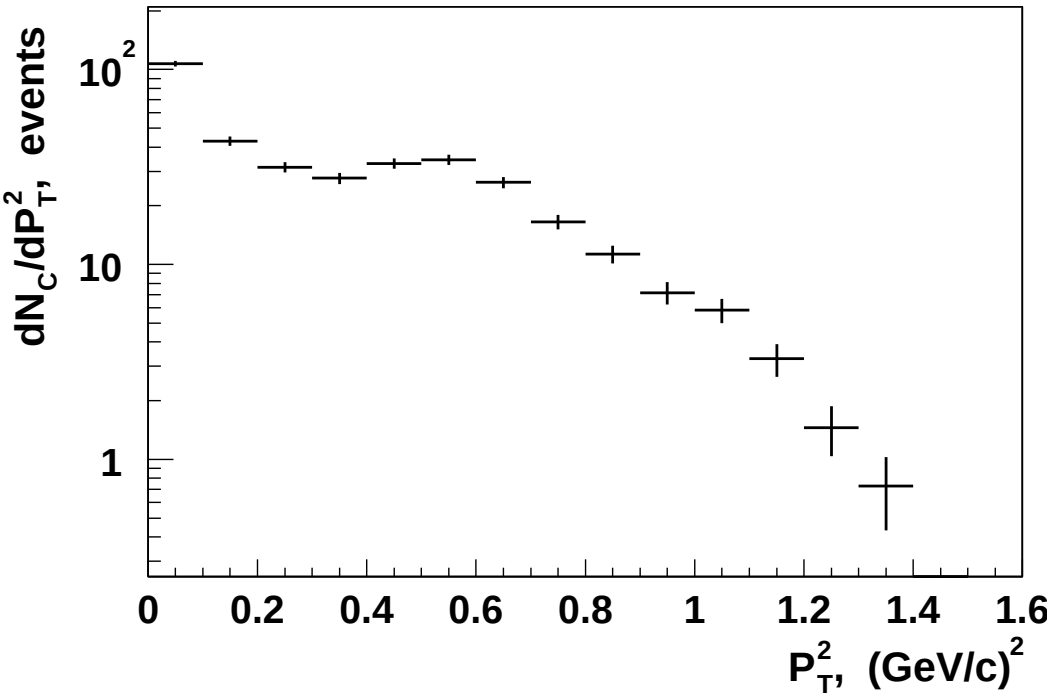

Figure 5.13: $\frac{dN_C}{dP_T^2}$ distribution for Carbon.

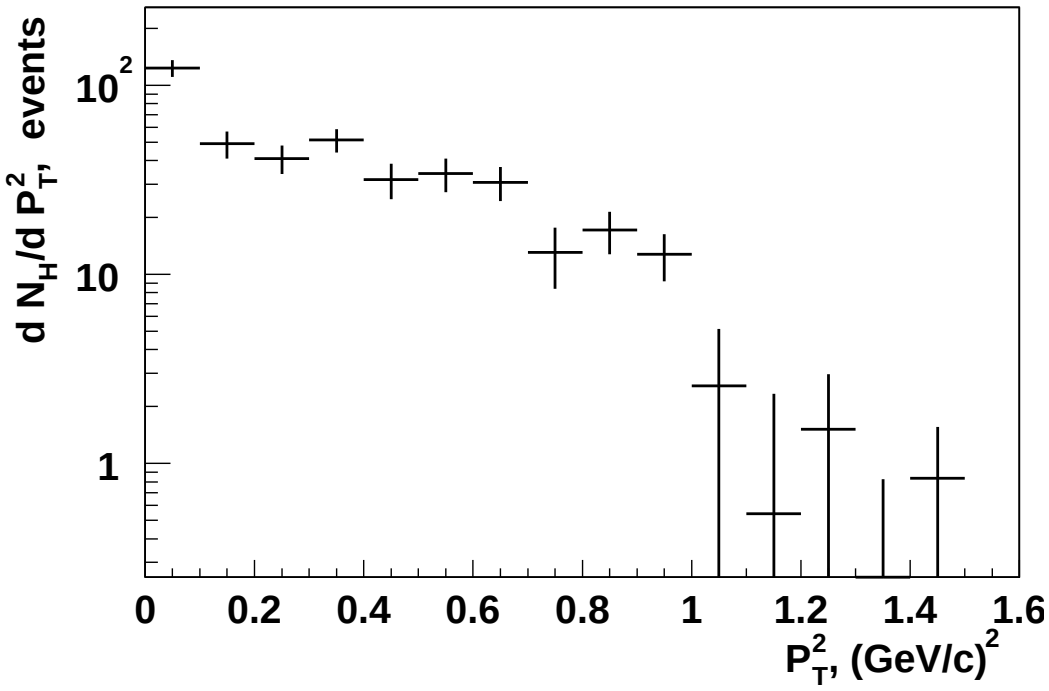

Figure 5.14: $\frac{dN_H}{dP_T^2}$ distribution for Hydrogen.

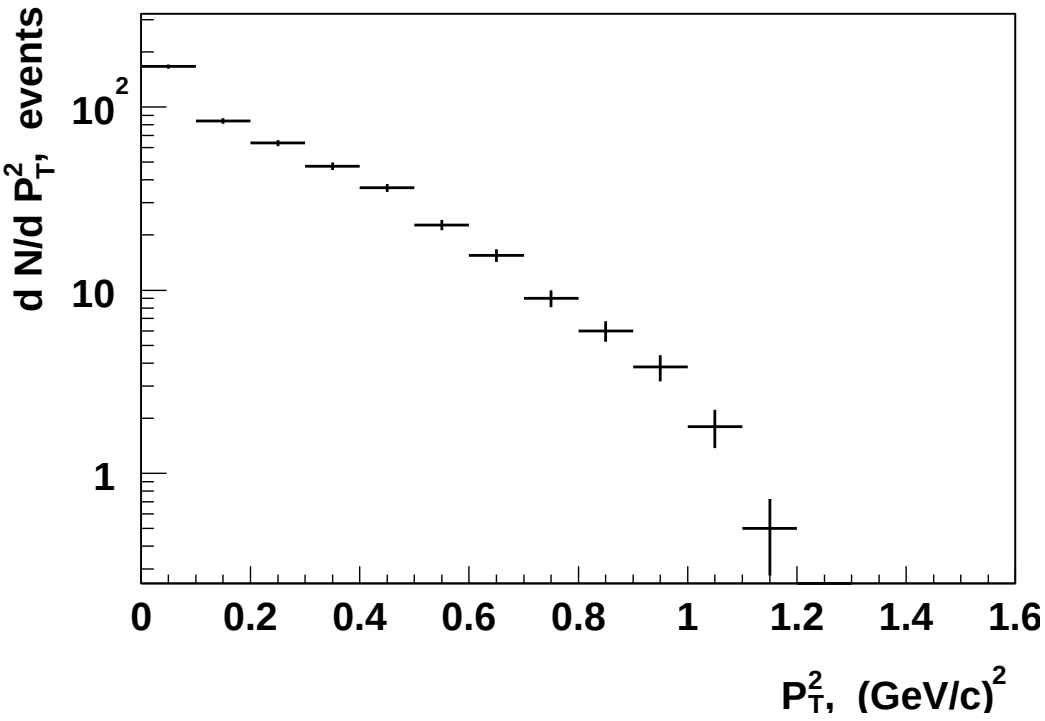

Figure 5.15: $\frac{dN}{dP_T^2}$ distribution for the phase space of the $pp \rightarrow pp\pi^0$ reaction. Monte-Carlo simulation in GEANT.

phase space generator. The cross section changes the slope of the distribution but does not create a flat part (Figure 5.16).

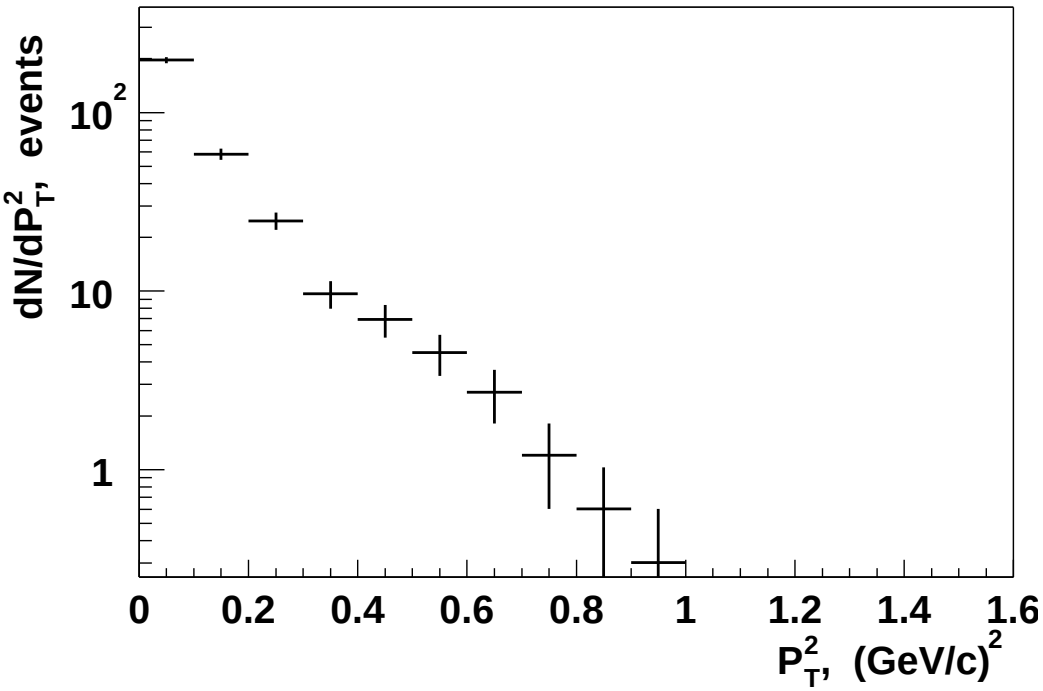

Figure 5.16: $\frac{dN}{dP_T^2}$ distribution for the reaction of the fragmentation in the $pp \to pp\pi^0$ process. Monte-Carlo simulation in GEANT.

We check if the flat shape of the P_T^2 distribution can be a result of a resonance decay. We simulate the resonance production with a consequent resonance decay. The phase space generator is used to produce $pp \to pN^*$ events. The resonance decay of the $N^* \to p\pi^0$ is assumed to be isotropic in the rest frame of the resonance.

We generate the distributions for N^* with the masses of 1.232 GeV,1.440 GeV and 1.520 GeV. In Figure 5.17 we plot the P_T^2 distribution for these resonances. The flat distribution is not reproduced in the case of the isotropic decay.

The inclusive π^0 production was studied in many experiments. We describe the conditions of the experiments and plot the $\frac{d\sigma}{dP_T^2}$ distributions in Appendix E.

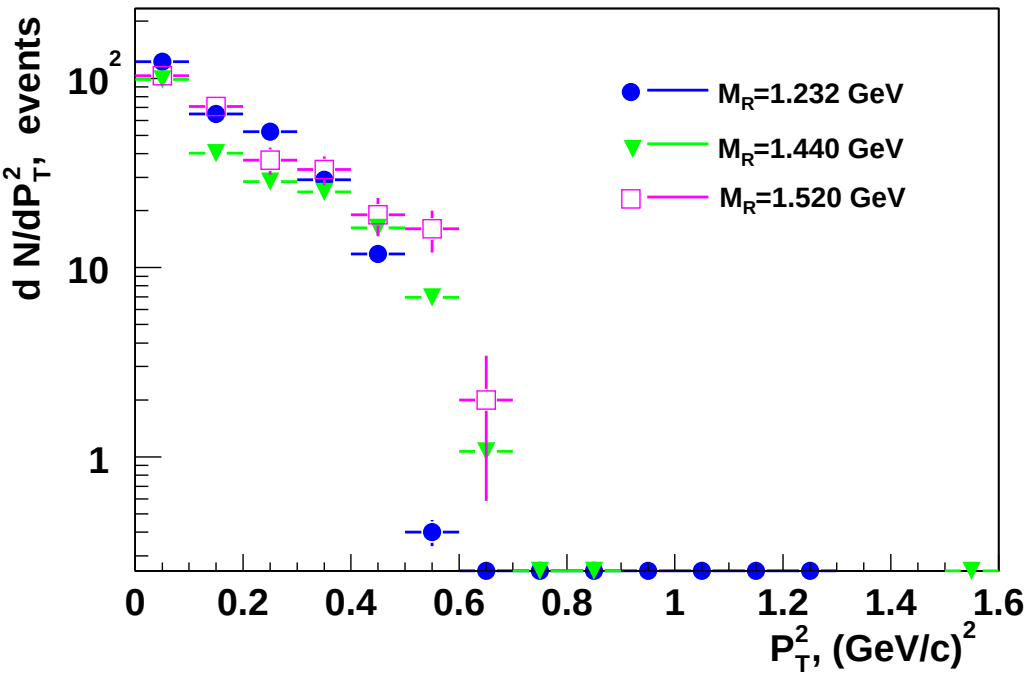

Figure 5.17: $\frac{dN}{dP_T^2}$ distribution for the $pp \to pN^* \to pp + \pi^0$ reaction. Monte-Carlo simulation in GEANT.

The shape of the differential $\frac{d\sigma}{dP_T^2}$ cross section is similar in production of different mesons under different conditions with varying beam types and changing energies. The distributions have an exponential fall-off with P_T^2. In these experiments the cross section decreases by about an order of magnitude over a range of $P_T^2 \in (0.05, 0.7)(GeV/c)^2$.

However, the shape of the cross section, that we observe, is flat in this range (Figures 5.13,5.14).

We hope to explain the $\frac{d\sigma}{dP_T^2}$ phenomenon based on the nature of our data sample. Our trigger selects the protons with large transverse momenta. Large transverse momentum of the out-going particles is the result of a hard scattering (section 4.1). The out-going protons experience Lorenz contraction. The contraction takes place in the direction of the incoming beam as well. The relativistic protons have a small size in the scattering plane due to this

effect.

We speculate that the 'flat-P_T^2' effect can be a result of a pion production via a bremsstrahlung of a 'cigar-shaped' proton in the Landshoff scattering. In the hard scattering, the quarks are accelerated when they absorb a large momentum in the direction, transverse to their original motion. This acceleration is accompanied by the radiation of the gluons, which may produce a pion by the means of a soft interaction with a proton.

In a composite object there are interference effects in the process of radiation by the individual constituents. In a color neutral proton, the radiation is not suppressed by the interference effects until the wavelengths of the radiated gluons are greater than or equal to the size of the proton.

The distance between the valence quarks of a normal size proton is about 1fm. The momentum of the gluon that corresponds to the wavelength of 1fm is about 0.2 GeV/c. For a larger wave length, the accelerating proton radiates as a color neutral object, not a composite system. A proton is a color singlet. The radiation of the color fields (gluons) for an accelerated color neutral object is suppressed. In this case the suppression of the soft part of the gluon spectra can be seen at missing $P_T^2 < .04(GeV/c)^2$.

Suppose that the transverse distance between the quarks of a 'cigar-shaped' proton is about 0.3 fm. Then, the bremsstrahlung may be suppressed at missing $P_T^2 < .36(GeV/c)^2$. The suppression of the soft gluon emission flattens the otherwise exponensial decrease of the missing P_T^2 spectrum.

There is no suppression of the small magnitude of the transverse momentum component out of the scattering plane.

The radiated gluons are mostly in the plane of the acceleration of the particle. The

plane of the acceleration coincides with the scattering plane in the case of hard scattering. We expect to see a large component of the missing transverse momentum in the scattering plane and a small component of the momentum out of the scattering plane.

5.3.2 The projections of the transverse momentum on the axis of the scattering plane

To check the bremsstrahlung hypothesis we study the projections of the missing transverse momentum on the scattering plane. The coordinate system related to the scattering plane is plotted in Figure 5.18. On this diagram (Figure 5.18) the beam (Z-axis) is coming at us. The XY ($R\Phi$) plane is transverse to the beam direction. We choose the direction of the transverse momentum of the particle with larger P_T as one of the scattering plane axis.

We projected the missing transverse momentum on the IN-plane and OUT-of-plane axis. in Figure 5.19 we plot the components of the transverse momentum of the missing particle for carbon and hydrogen. On can see (Figure 5.19) a strong suppression of the $\frac{dN}{dP_{IN}}$ distribution in the region of the small in-plane momentum ('IN-plane dip').

We need to check that the suppression is not an artefact of the acceptance or the phase space. We project the missing transverse momentum on the IN and OUT axis for elastic events (Figure 5.20). Elastic events have $\vec{P}_{miss} = 0$. The spread in the momentum comes from the detector resolution. There is no suppression of the IN-plane component distribution of the missing momentum for the elastic events. The resolution out of the scattering plane is better than the resolution in the scattering plane. It leads to the difference in the width of the plotted distributions.

We do not see the 'IN-plane dip' in the Monte-Carlo simulations of the phase space for

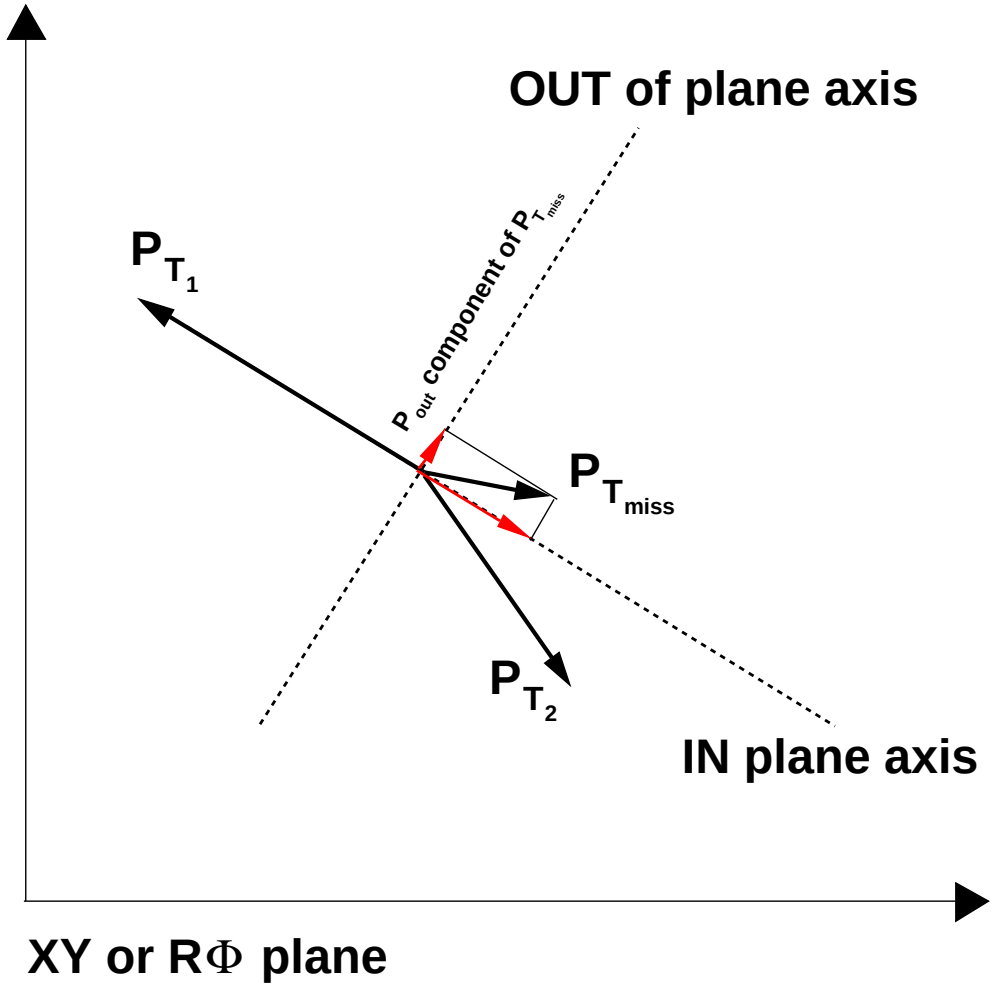

Figure 5.18: The coordinate system for the IN and OUT of plane components of the transverse momentum.

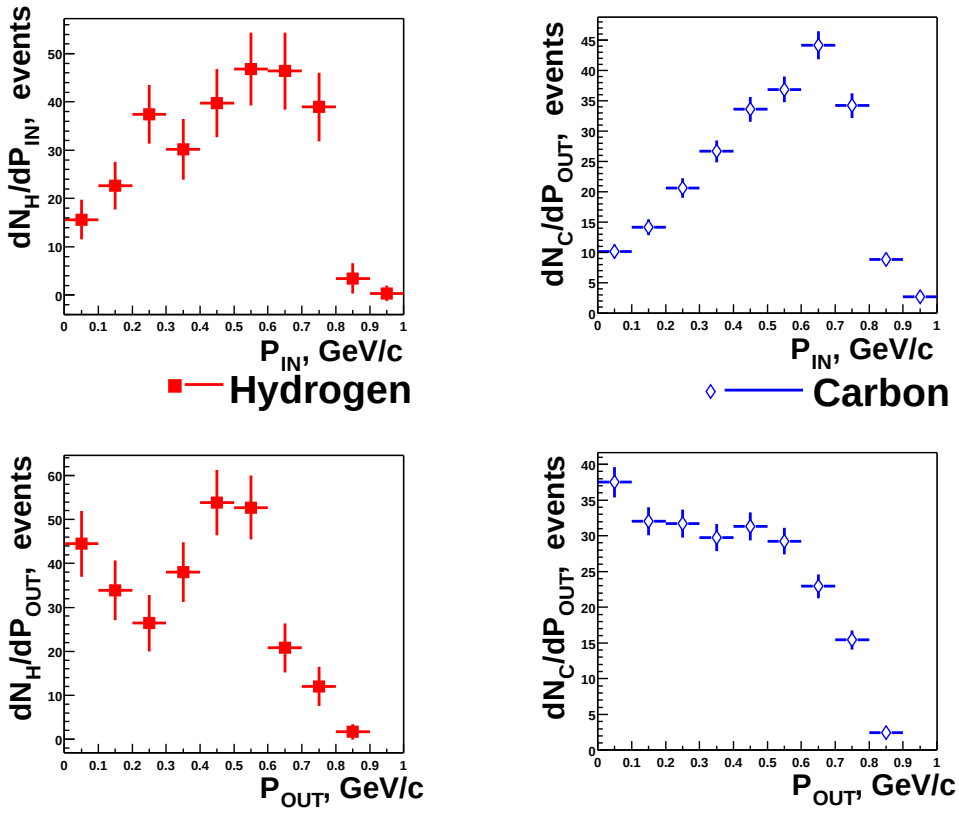

Figure 5.19: The components of the transverse momentum IN and OUT of the scattering plane.
LEFT: The distributions for the Hydrogen target.
RIGHT: The distributions for the Carbon target.
The elastic and quasi-elastic events are removed by the $cos(\Theta_{miss}) > 0.6$ cut.

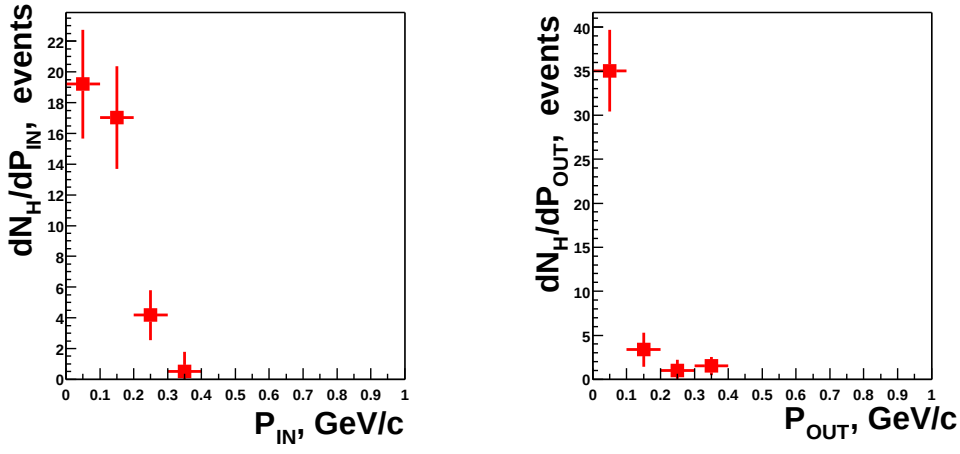

Figure 5.20: The components of the transverse momentum IN and OUT of the scattering plane for the elastic events on Hydrogen.

$pp \to pp + \pi^0$ reaction (Figure 5.21).

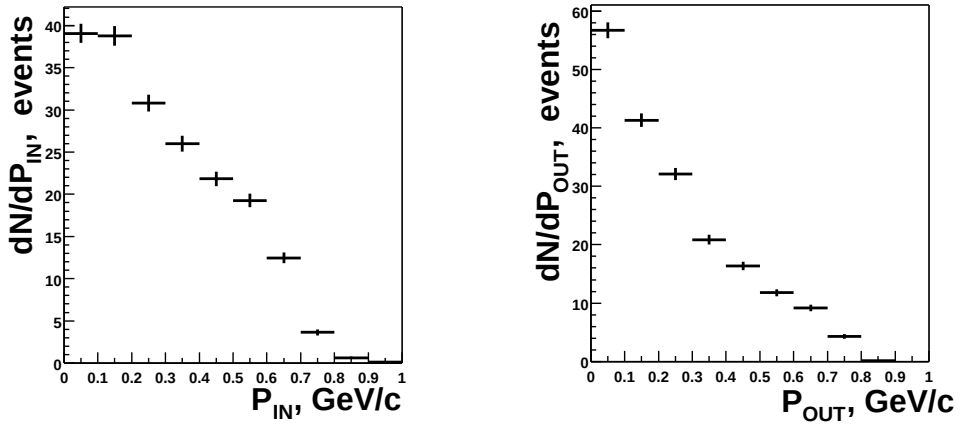

Figure 5.21: The components of the transverse momentum IN and OUT of the scattering plane for the Monte-Carlo simulated phase space of the $pp \to pp + \pi^0$ events.

We can simulate the general shape of the $\frac{dN}{dP_T^2}$ distribution, seen in Figures 5.13,5.14, via the resonance processes. We modify the cross section for the resonance decay. We introduce the anisotropic decay distribution in which the pion favors the original direction of the resonance's momentum. The probability of decay is proportional to $cos^2(\Theta_{\pi^0}/2)$.

Where Θ_{π^0} ($\Theta_{\pi^0} \in (0;\pi)$) is the angle between $\vec{P}_{\pi^0}$ and $\vec{P}_{resonance}$ in the rest frame of the resonance.

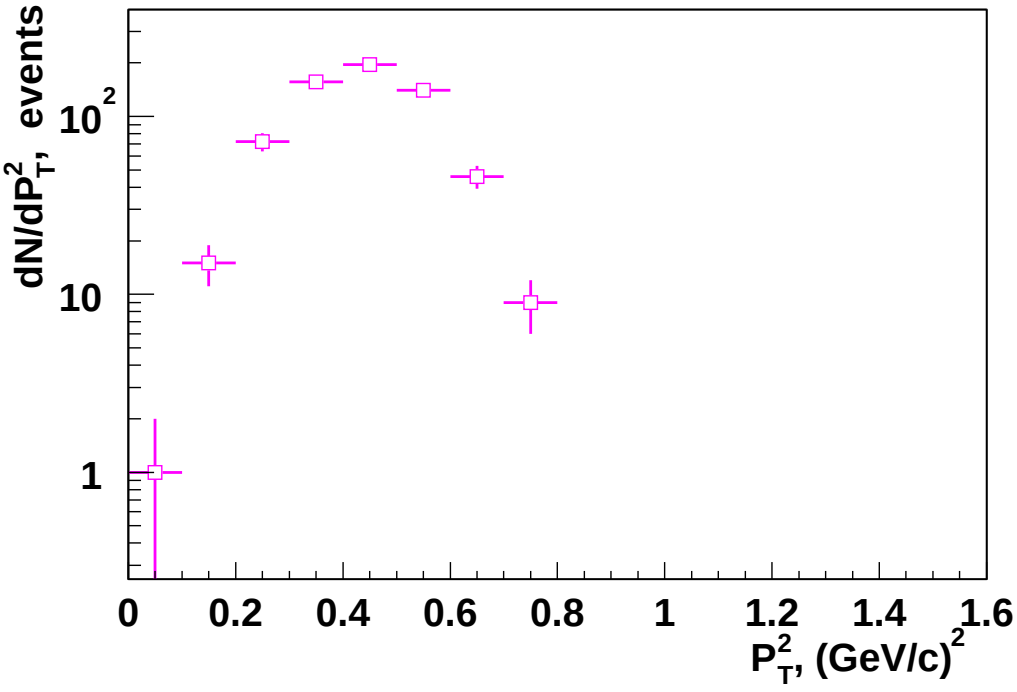

Figure 5.22: The P_T^2 distribution for a N(1520) resonance decay with anisotropic decay distribution. The pion is moving in the direction of the resonance's momentum. Monte-Carlo simulation in GEANT.

In Figure 5.22 we plot the $\frac{dN}{dP_T^2}$ for a $N^*(1520)$ resonance with a modified decay distribution. We see that the exponential fall-off is suppressed for small missing transverse momentum. However, the IN and OUT of plane projections do not follow the same trends as seen in the data.

We see that the distributions for the both components are suppressed at small values (Figure 5.23). It is possible to make the distribution for the OUT of plane component to be similar to the one seen in the data. We can do it by introducing the Φ anisotropy in the decay distribution of the resonance. The decay distribution of a resonance has to be very

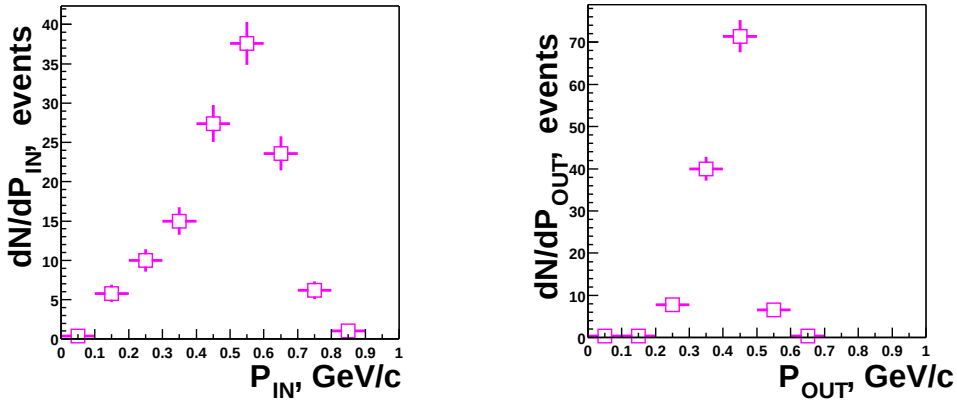

Figure 5.23: The components of the transverse momentum IN and OUT of the scattering plane for the N(1520) resonance decay with a modified cross section. Monte-Carlo simulation in GEANT.

anisotropic to reproduce the dependences seen in the data.

We summarize our observations here. We see a 'flat-P_T^2' distribution for our data sample. There is an asymetry between the components of the momentum in and out of the scattering plane. The asymetry is a lack of events with small component of the momentum in the scattering plane.

These observations are not the consequences of the detector acceptance or resolution. They are not the effects of the phase space either. We do not reproduce the trends, seen in the data, using the Monte-Carlo simulations of the fragmentation process or the isotropic resonance decay.

The bremsstrahlung by a 'cigar-shaped' proton might explain the 'flat-P_T^2' trend and the scattering plane asymetry.

5.3.3 The angular and momentum distributions in the CM frame of the incoming particles

We characterize the events of the data set with the angular and momentum distributions in the center of mass frame of the incoming particles. The diagram of the coordinate system is given in Figure 5.24. The beam direction and the direction of the one of the protons

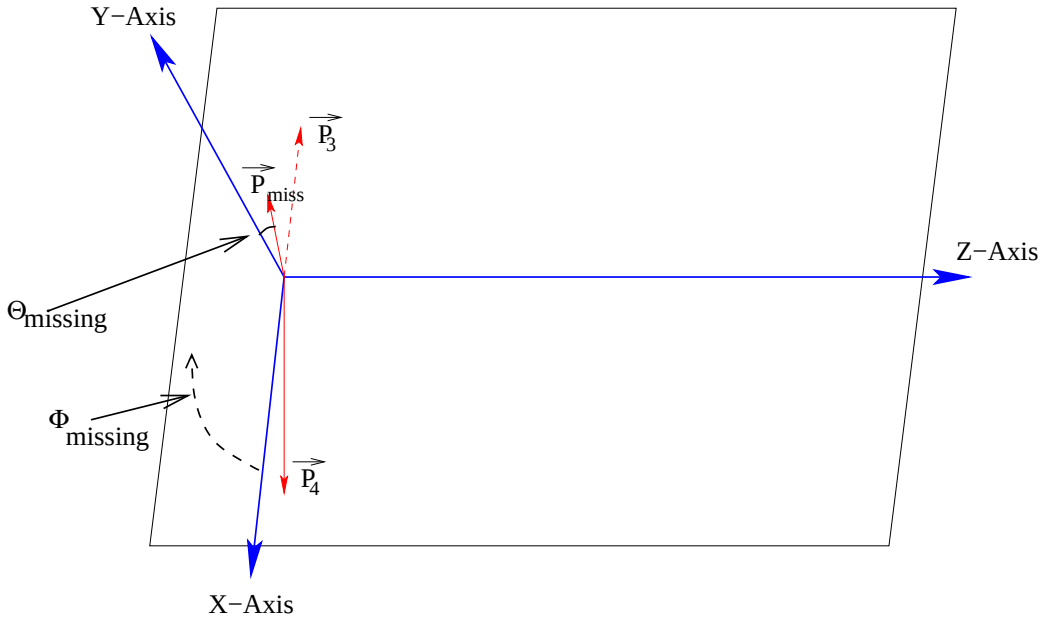

Figure 5.24: The diagram of the coordinate system in the CM frame of the incoming particles. The proton P_4 has the larger P_T than the proton P_3.

form the scattering plane. The Y-axis, perpendicular to this plane, is the OUT-of-plane axis. The beam direction, Z-axis, is one of the IN-plane axis. We call the axis, which is perpendicular to the Z and Y axis, the X-axis.

We choose the X-axis to be in the direction of the proton with the larger P_T. The proton with larger P_T is more likely to be a direct product of the hard scattering. In the case of bremsstrahlung or resonance decay a proton looses a fraction of the transverse momentum. The proton with smaller transverse momentum is more likely to be a product of a secondary

process. Based on this argument, the plane of the beam and the proton with large P_T is a good choice for the plane of the hard scattering. In this case we suppose that the missing particle comes from the bremsstrahlung of the second out-going proton.

In this coordinate system we plot the $cos(\Theta_{miss}^{CM})$ and Φ_{miss}^{CM}. The $cos(\Theta_{miss}^{CM})$ is the cosine of the angle between the momentum of the missing particle and the Y-axis. The Φ_{miss}^{CM} is the angle between the X-axis and the projection of the missing momentum on the scattering plane.

If the mechanism of the missing particle production is via gluon bremsstrahlung, we will see the distribution of the $cos(\Theta_{miss}^{CM})$ around 0. The $cos(\Theta_{miss}^{CM})$=0 corresponds to the missing particle in the scattering plane. We expect the Φ_{miss}^{CM} distribution to be centered around π rad. It corresponds to the bremsstrahlung of the missing particle along the direction of the second proton.

The 3D-LEGO plot of the $cos(\Theta_{miss}^{CM})$ versus Φ_{miss}^{CM} for Hydrogen target is provided in Figure 5.25. We project this histogram on the Φ_{miss}^{CM} and $cos(\Theta_{miss}^{CM})$ axis and plot it in Figure 5.26. The corresponding distributions for Carbon target are plotted in Figures 5.27 and 5.28. The Φ_{miss}^{CM} angle of the missing momentum looks as it is expected from the bremsstrahlung mechanism. The missing momentum is in the direction of the second particle. The distribution of the out-of-plane angle is not understood as clearly. We see a large number of events with the momentum of the missing particle pointing out of the scattering plane. This is not in agreement with the conclusions of the bremsstrahlung idea.

We find it possible to separate the out-of-plane and in-plane events. We make a cut on

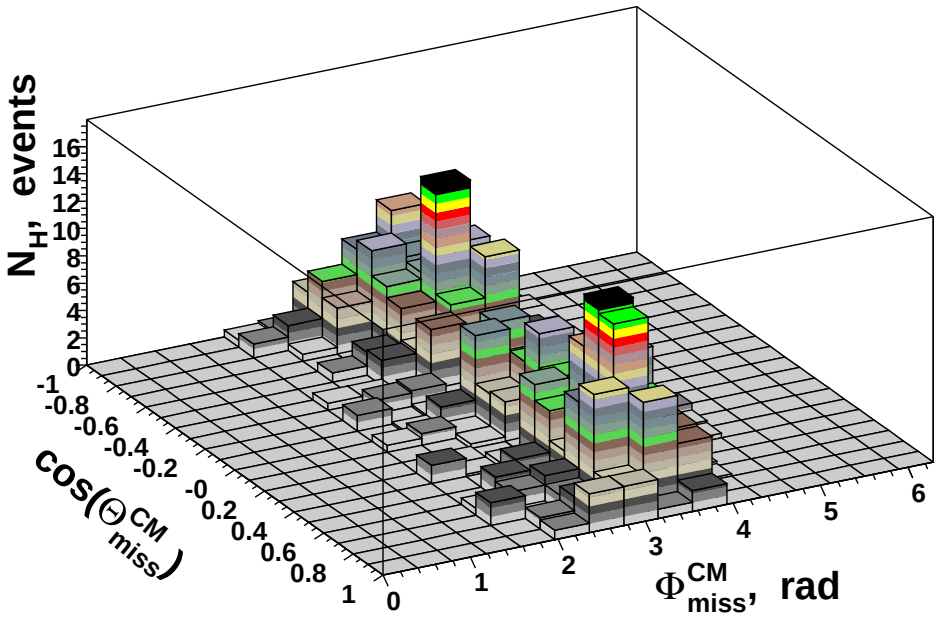

Figure 5.25: The LEGO plot of the $cos(\Theta^{CM}_{miss})$ versus Φ^{CM}_{miss} distribution for Hydrogen.

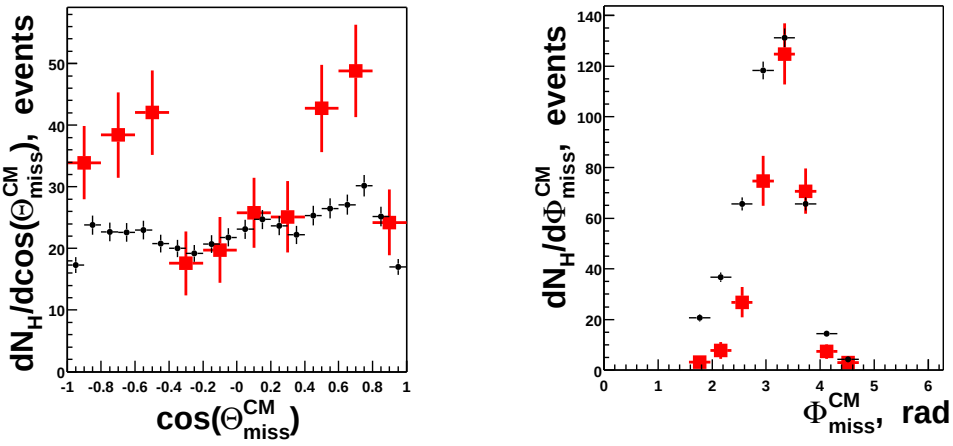

Figure 5.26: The projections of the LEGO histogram of the Figure 5.25.
LEFT: The $cos(\Theta^{CM}_{miss})$ distribution for $pp \to pp + \pi^0$ events.
RIGHT: The Φ^{CM}_{miss} distribution for $pp \to pp + \pi^0$ events.
The data is for the Hydrogen target. The Monte-Carlo simulated distributions for the phase space of the $pp \to pp + \pi^0$ reaction are plotted in black (small circle marker).

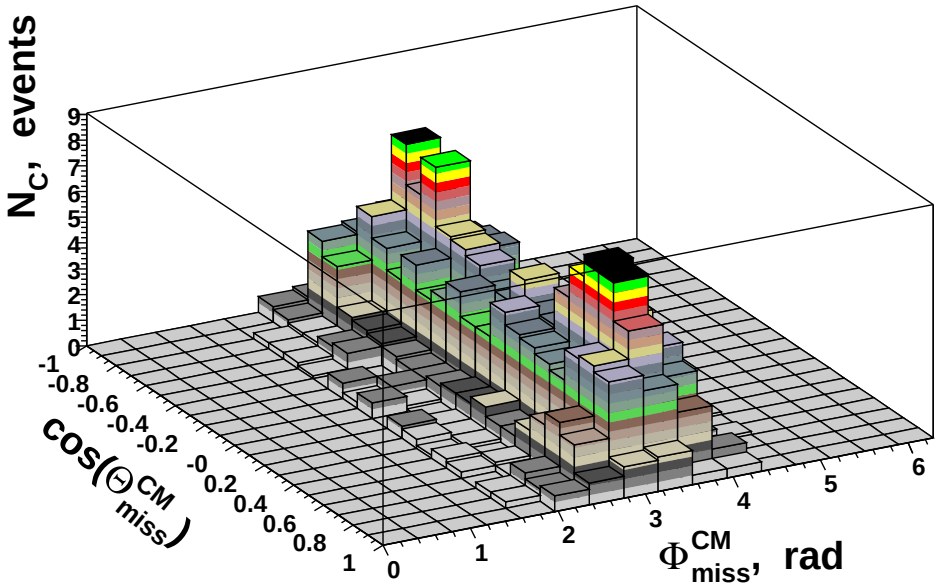

Figure 5.27: The LEGO plot of the $cos(\Theta^{CM}_{miss})$ versus Φ^{CM}_{miss} distribution for Carbon.

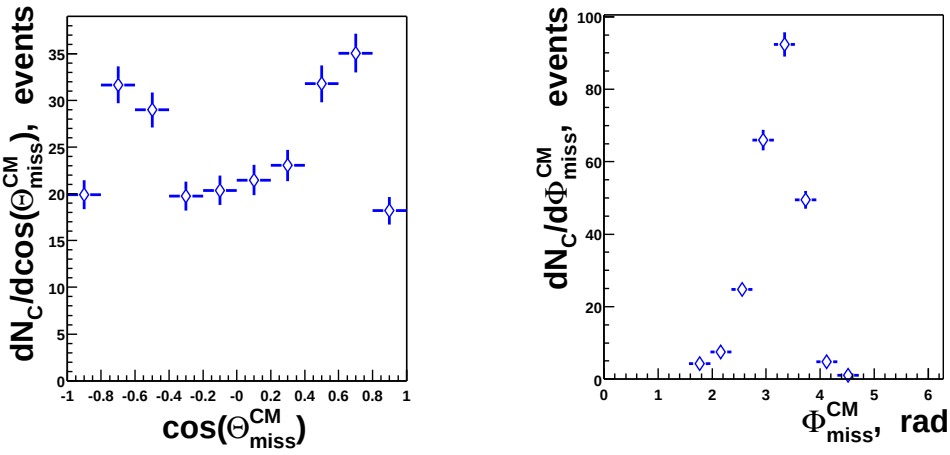

Figure 5.28: The projections of the LEGO histogram of the Figure 5.27.
LEFT: The $cos(\Theta^{CM}_{miss})$ distribution for $pp \to pp + \pi^0$ events.
RIGHT: The Φ^{CM}_{miss} distribution for $pp \to pp + \pi^0$ events.
The data is for the Carbon target.

the effective mass of the second proton and the missing particle. This cut

$$M^2(p\pi^0) < 2GeV^2. \tag{5.21}$$

selects the events with the missing particle in the scattering plane. The angular distributions are provided in Figure 5.29. We see the missing momentum to be in the scattering plane

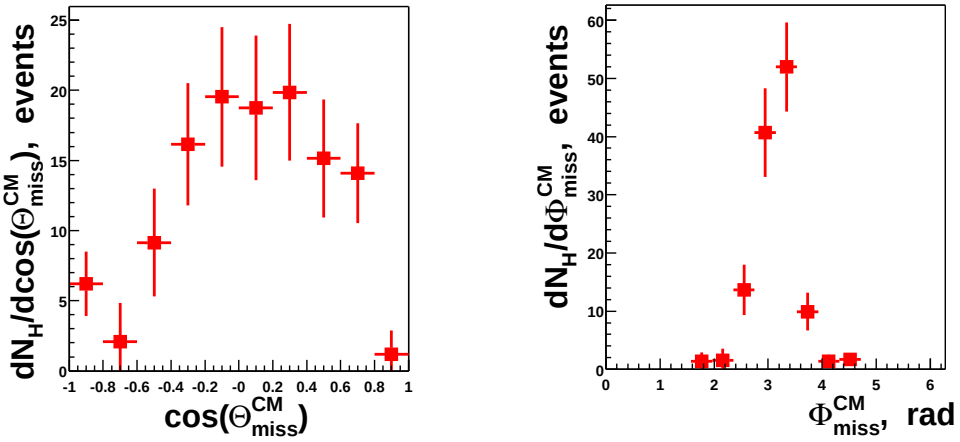

Figure 5.29: The $cos(\Theta^{CM}_{miss})$ and Φ^{CM}_{miss} distribution for $pp \rightarrow pp + \pi^0$ events with the $M^2_{eff} < 2GeV^2$ cut. The data is for the Hydrogen target.

and along the direction of the second proton. Both distributions are in a good agreement with the bremsstrahlung radiation mechanism.

We select the out of plane events with the following cut

$$M^2(p\pi^0) > 2GeV^2. \tag{5.22}$$

The angular distributions show the missing momentum being in the direction of the second particle but out of the scattering plane (Figure 5.30). Moreover, these events have on average the larger magnitude of the missing momentum than the events with the in-plane $\vec{P}_{miss}$ (Figure 5.31).

The angular distributions for Carbon target in the selected regions of the M^2_{eff} are plotted in Figures 5.32 and 5.33.

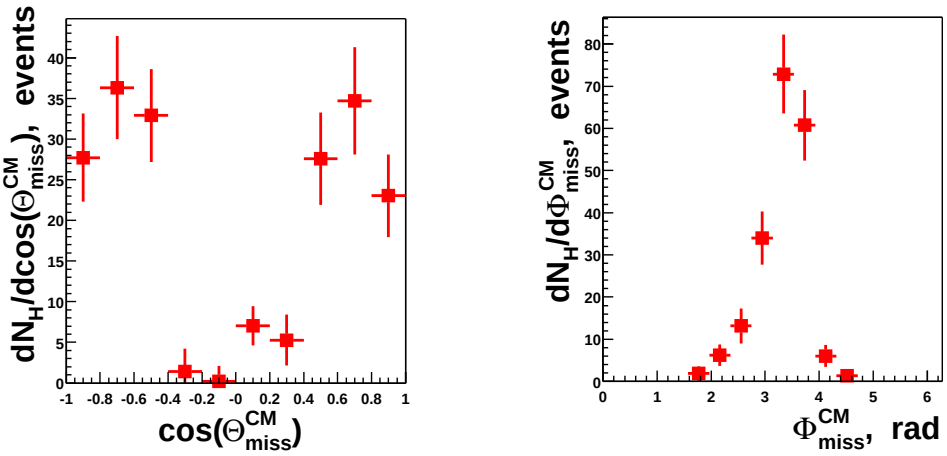

Figure 5.30: The $cos(\Theta^{CM}_{miss})$ and Φ^{CM}_{miss} distribution for $pp \rightarrow pp + \pi^0$ events with the $M^2_{eff} > 2GeV^2$ cut. The data is for the Hydrogen target.

An explanation of the out-of-plane production of π^0 was proposed by E.Piasetzky [60]. He suggested that in the process of the hard scattering a proton can be excited into a special state. In this state one of the quarks is moving out of the scattering plane. The other two are moving in the opposite direction. The single quark forms a pion during the break-off. E.Piasetzky speculated that momentum of the pion should be on the order of 1 GeV/c. This idea explaines well the angular and momentum distributions for the out-of-plane events.

We propose a second explanation for these events. We recall the differential cross sections for the resonance production measured by Ankenbrandt *et al* [48]. According to their measurement the $N^*(1512)$ and $N^*(1688)$ resonances have cross section comparable to the elastic cross section in the hard wide-angle scattering. The cross section for a lower mass resonance $N^*(1238)$ is smaller by more than an order of magnitude.

It is possible that by applying a cut on the effective mass $M^2(p\pi^0) > 2GeV^2$ we select

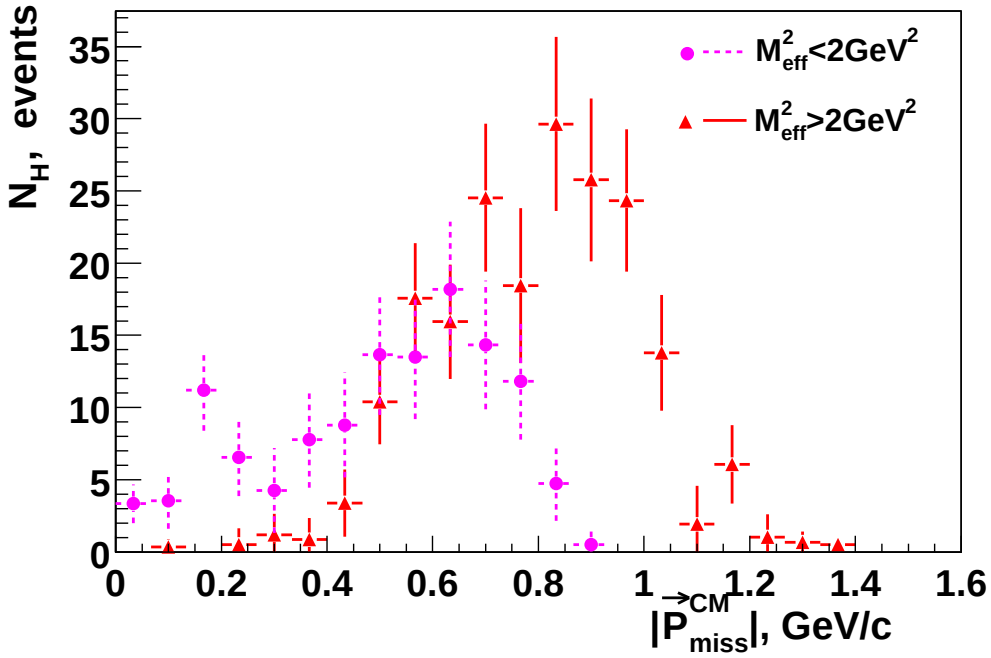

Figure 5.31: The comparison of the magnitude of the $\vec{P}_{miss}$ for the $M^2_{eff} < 2Gev^2$ and the $M^2_{eff} > 2Gev^2$ cuts. The pink (dashed and circle marker) histogram is for the $M^2_{eff} < 2Gev^2$ cut. The red (solid and triangle marker) histogram is for the $M^2_{eff} > 2Gev^2$ cut. The data is for the Hydrogen target.

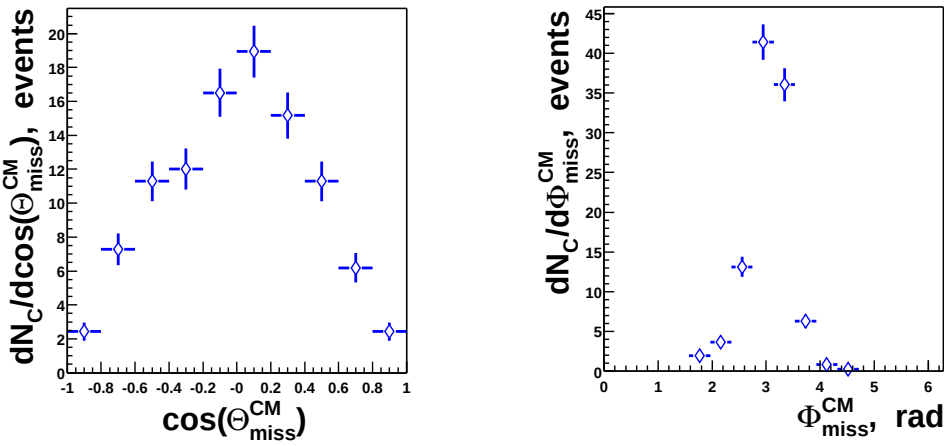

Figure 5.32: The $cos(\Theta^{CM}_{miss})$ and Φ^{CM}_{miss} distribution for $pp \rightarrow pp + \pi^0$ events with the $M^2_{eff} < 2GeV^2$ cut. The data is for the Carbon target.

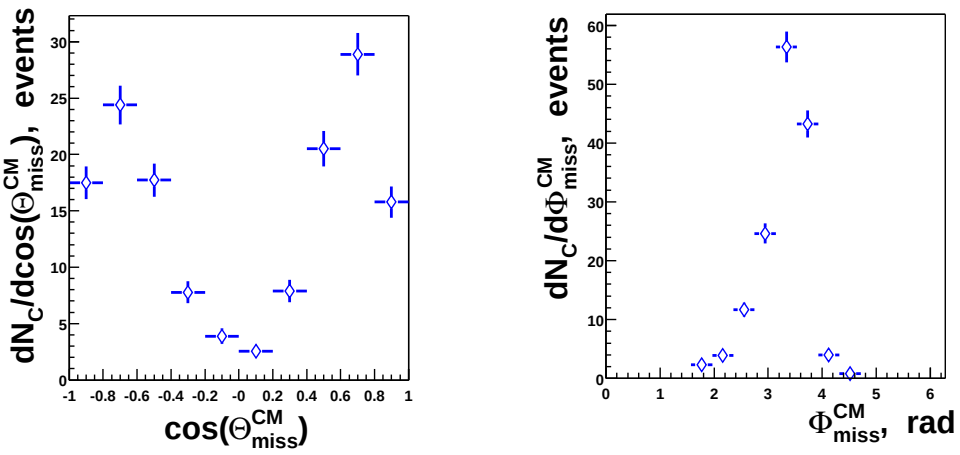

Figure 5.33: The $cos(\Theta^{CM}_{miss})$ and Φ^{CM}_{miss} distribution for $pp \rightarrow pp + \pi^0$ events with the $M^2_{eff} > 2GeV^2$ cut. The data is for the Carbon target.

mostly the π^0 production from the resonance decay. In contrust, the cut $M^2(p\pi^0) < 2GeV^2$ selects the events with π^0 coming from bremsstrahlung.

In the case of a resonance decay we simulated the pion production with a non-isotropic resonance decay distribution (Figure 5.23). The distributions of the IN and OUT of plane components of the $\vec{P}_{miss}$ simulated with Monte-Carlo look similar to the data in the region of the large effective mass (Figure 5.34). However, we do not know how to justify such anisotropy in the decay distribution of the resonances.

5.3.4 The angular distributions in the Rest Frame of the resonance

In a different represantation of the angular distributions, we characterize the events in the Rest Frame of the resonance. The Rest Frame (RF) coordinate system is defined based on the assumption that one of the protons and a pion form a resonance. Then, the momentum

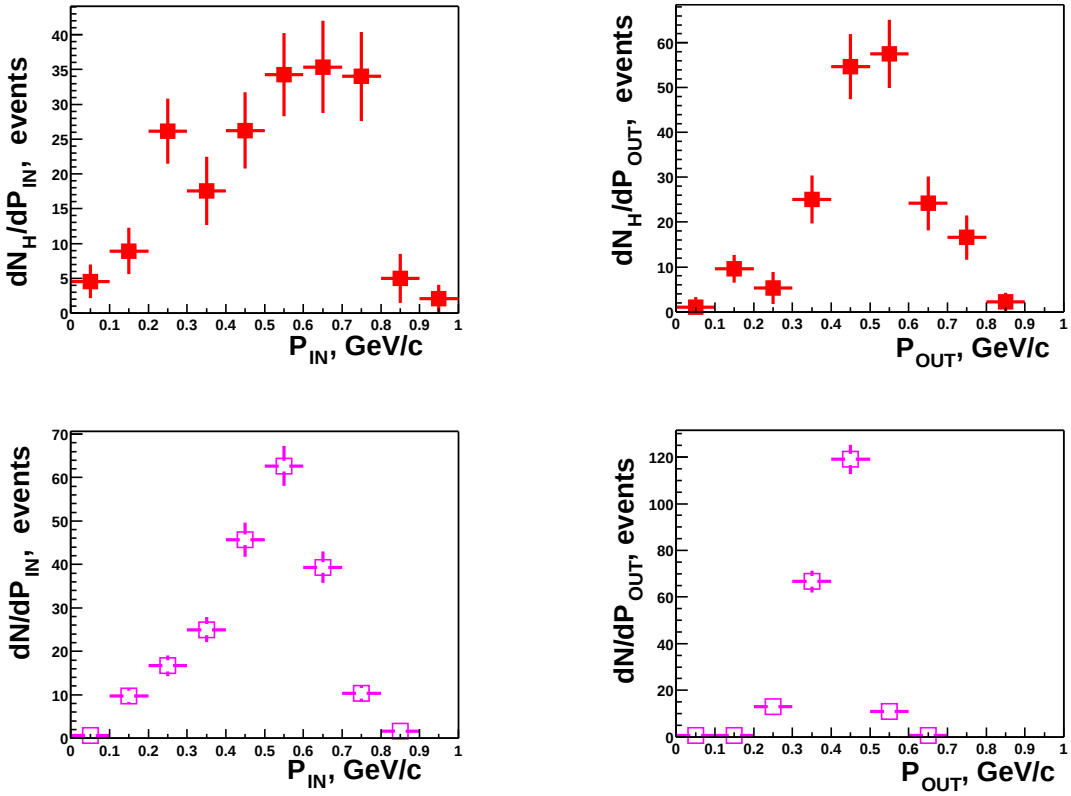

Figure 5.34: The comparison of the IN and OUT of plane components of the $\vec{P}_{miss}$ for the data and the simulated π^0 production.
TOP: The components of the transverse momentum IN and OUT of the scattering plane for the data on the Hydrogen target with $M^2_{eff} > 2Gev^2$ cut.
BOTTOM: The components of the transverse momentum IN and OUT of the scattering plane for the simulated π^0 production via non-isotropic resonance decay of the $N^*(1520)$.

of the resonance is equal to the sum of the momentums of a proton and a pion.

$$\vec{P}_{resonance} = \vec{P}_{proton} + \vec{P}_{pion} = \vec{P}_3 + \vec{P}_{miss}$$

The diagram of the coordinate system is given in Figure 5.35. The beam direction and

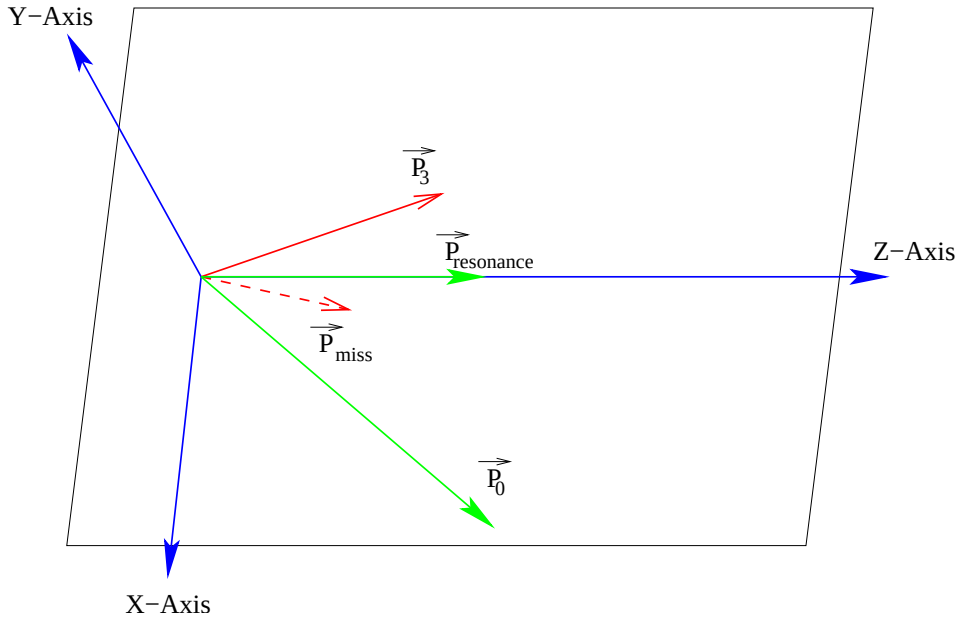

Figure 5.35: The diagram of the coordinate system in the Rest Frame of the resonance. The proton P_3 has the smaller of the proton P_Ts.

the direction of the resonance form the scattering plane. The Y-axis, perpendicular to this plane, is the OUT-of-plane axis. The resonance direction, Z-axis, is one of the IN-plane axis. We call the axis, which is perpendicular to the Z and Y axis, the X-axis. The Z-axis, X-axis, $\vec{P}_{resonance}$ and $\vec{P}_0$ are all in the scattering plane.

In this coordinate system we analize the $cos(\Theta^{RF}_{miss})$ and Φ^{RF}_{miss} distributions. The $cos(\Theta^{RF}_{miss})$ is the cosine of the angle between the momentum of the missing particle and the Y-axis. The Φ^{RF}_{miss} is the angle between the Z-axis and the projection of the missing momentum on the scattering plane. We will refer to the region of Φ^{RF}_{miss} less than $\frac{\pi}{2}$ as the

forward hemishpere.

In the previous sections we discussed that the missing pion may be a product of the resonance decay. We presented the Monte-Carlo simulations of the non-isotropic resonance decay. The general trends of the data were reproduced when the pion was generated with the momentum in the forward hemisphere.

We plot the $cos(\Theta^{RF}_{miss})$ and Φ^{RF}_{miss} distribution for Hydrogen and Carbon targets in Figure 5.36. The distributions for Hydrogen target are red and have a square marker. The Carbon target distributions are blue and have a diamond marker. As we expected,

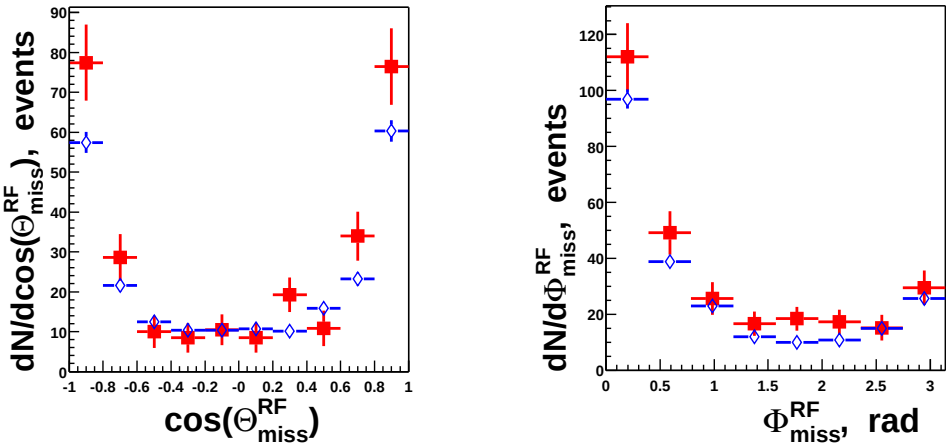

Figure 5.36: The angular distributions in the Rest Frame.
LEFT: The $cos(\Theta^{RF}_{miss})$ distribution for $pp \to pp + \pi^0$ events.
RIGHT: The Φ^{RF}_{miss} distribution for $pp \to pp + \pi^0$ events.
The data points in red (square marker) are for the Hydrogen target. The data points in blue (diamond marker) are for the Carbon target.

in the majority of events, the momentum, $\vec{P}^{\pi^0}_{miss}$, is in the forward hemisphere. Similar to the distributions in the CM frame, in some events $\vec{P}^{\pi^0}_{miss}$ is OUT of the scattering plane. We divide the data in two sets the same way it was done before. We make a cut on the M^2_{eff}. The distributions for two regions in the M_{eff} are plotted in Figures 5.37 and 5.38.

We observe an isotropic distribution (Figure 5.37) in $cos(\Theta^{RF}_{miss})$ for the events with the

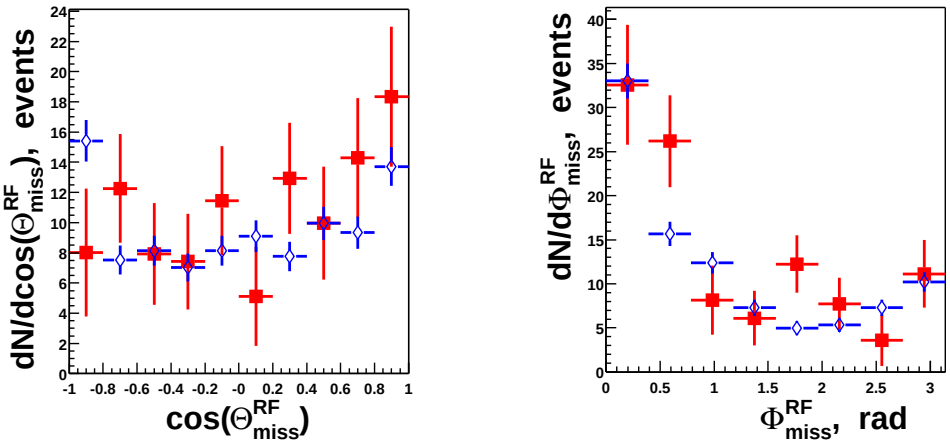

Figure 5.37: The $cos(\Theta^{RF}_{miss})$ and Φ^{RF}_{miss} distribution for $pp \rightarrow pp + \pi^0$ events with the $M^2_{eff} < 2GeV^2$ cut.
LEFT: The $cos(\Theta^{RF}_{miss})$ distribution for $pp \rightarrow pp + \pi^0$ events.
RIGHT: The Φ^{RF}_{miss} distribution for $pp \rightarrow pp + \pi^0$ events.
The data points in red (square marker) are for the Hydrogen target. The data points in blue (diamond marker) are for the Carbon target.

small M^2_{eff} (less than $2GeV^2$). However, the missing momentum is mostly in the forward hemisphere.

The $cos(\Theta^{RF}_{miss})$ distribution for the large M^2_{eff} (greater than $2GeV^2$) indicates that the momentum of the missing pion is out of the scattering plane but still mostly in the forward hemisphere. The angular distributions for the large M^2_{eff} are very non-isotropic.

The angular distributions in the rest frame of the resonance are plotted with an assumption that a pion is the product of a resonance decay. These distributions are non-isotropic in the scattering plane. The pion is produced in the approximate direction of the resonance momentum. The decay distribution becomes even more non-isotropic in the out of plane direction when the resonance mass is large (more than $2GeV^2$). For the events with large resonance mass the pion is produced out of the scattering plane and along the direction of

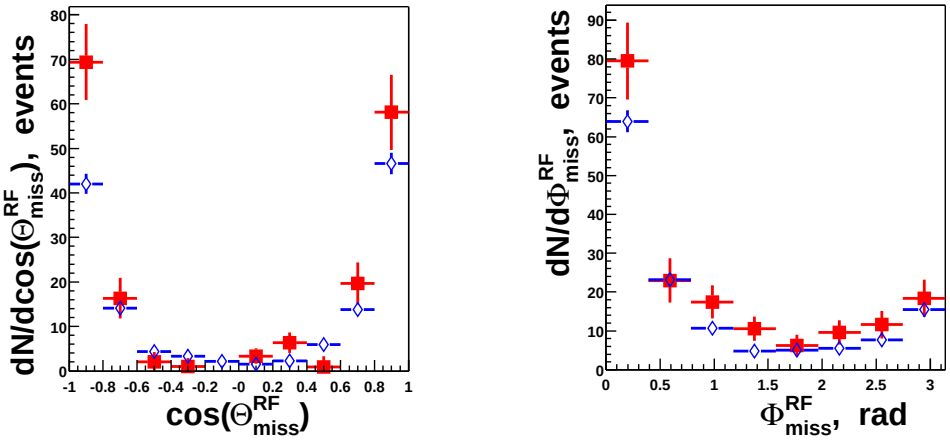

Figure 5.38: The $cos(\Theta^{RF}_{miss})$ and Φ^{RF}_{miss} distribution for $pp \to pp + \pi^0$ events with the $M^2_{eff} > 2GeV^2$ cut.
LEFT: The $cos(\Theta^{RF}_{miss})$ distribution for $pp \to pp + \pi^0$ events.
RIGHT: The Φ^{RF}_{miss} distribution for $pp \to pp + \pi^0$ events.
The data points in red (square marker) are for the Hydrogen target. The data points in blue (diamond marker) are for the Carbon target.

the resonance's momentum.

5.4 Conclusion

We summurize the results of the research, described in this chapter, below.

The semi-inclusive $pp \to ppX$ reaction was analized using the the distributions in the variable X_L. It was defined as a fraction of the total longitudinal momentum carried by two high P_T protons. We observed a shift in the X_L distribution for quasi-elastic events due to the strong s-dependence of the elastic pp cross section.

The differential cross section of the reaction was characterized with a function $F(X_L)$ in the limit $X_L \to 1$. This function is a sum of the polynomial of $(1 - X_L)$ and a gaussian part, centered around $X_L \sim 1$.

The angular and momentum distributions were analyzed for the $pp \rightarrow pp\pi^0$ reaction. We observed an unexpected 'flat-P_T^2' distribution for these events. We proposed an explanation of this effect. We speculated that a pion production via gluon bremsstrahlung by a proton of a small size in the plane of the wide-angle scattering can reproduce the observed distributions.

According to this idea, the missing pion should be in the scattering plane and have the missing momentum in the direction of the radiating proton. For a part of the data sample, we observe the trends in the angular and the momentum distributions that are in agreement with our interpretation.

In the other part of the data sample, the missing pion has a momentum pointing in the direction of the radiating proton but out of the plane of scattering. In general terms, we proposed two ideas that might explain these distributions.

Chapter 6

Results and Conclusions

Introduction

In this chapter we discuss the results of the analysis described in this thesis.

We analyzed the data for two data sets. They are the semi-inclusive $pp \rightarrow pp\pi^0$ reaction and inclusive $pp \rightarrow ppX$ reaction. In the first section (6.1) of the chapter we will discuss the less understood new effects in the analysis of the $pp \rightarrow pp\pi^0$ reaction.

The semi-inclusive $pp \rightarrow pp\pi^0$ reaction was characterized using the angular and momentum distributions. The emphasis was on the magnitude and direction of the momentum of the missing particle with respect to the scattering plane.

We could not explain the angular and momentum distributions, with respect to the scattering plane, in the light of the known theoretical concepts for the pion production. We speculate that a process of pion production via gluon bremsstrahlung in Landshoff scattering could provide an interpretation of the distributions for a part of the data sample.

The data set of the more inclusive, $pp \rightarrow ppX$, reaction was characterized using X_L variable, the fraction of the total longitudinal momentum in the initial state, carried by two final state high P_T protons. We have shown that the distributions in this variable can be used to understand the dependence of the wide-angle scattering cross section on the CM

energy.

In the well understood case of the elastic and quasi-elastic scattering we observed a shift in the X_L distribution on the nuclear target with respect to the distribution on the Hydrogen target. The shift indicates that the wide-angle elastic cross section has a strong dependence on the CM energy.

6.1 Characterization of the $pp \to pp\pi^0$ reaction

In this section we summarize the new effects that we see in the angular and momentum distributions for $pp \to pp\pi^0$ reaction and propose an interpretation of these effects.

We observe two striking effects in the momentum distributions of the $pp \to pp\pi^0$ events.

The first effect is observed in the distribution of the transverse component of the missing momentum. The missing momentum in this data sample is the momentum of an undetected π^0. The P_T^2 distribution of the missing pion is flat up to the values of P_T^2 approximately equal to $0.7(GeV/c)^2$. The effect is observed for Carbon and Hydrogen targets. The elastic and quasi-elastic events create a slight enhancement at the small values of the missing P_T^2.

We ran Monte-Carlo simulations in attempt to reproduce this effect. The simulations included the pion production via the proton fragmentation and resonance decay. In the simulation of the proton fragmentation we used the cross section formula derived for a 'star dust' process. The simulation of the pion production through the resonance decay had isotropic distribution for the decay. We were not able to create the flat P_T^2 distribution in these simulations.

The second unexpected effect is the suppression of the low values of the missing momen-

tum in the scattering plane of the reaction. We observe this effect in the distribution of P_{IN} variable. It is the projection of the missing momentum on the scattering plane. We see no such suppression in the distribution of the P_{OUT}, the projection of the missing momentum on the perpendicular to the scattering plane axis.

We indicated that the dip at small values of the P_{IN} distribution is not due to the resolution or detector acceptance effects. The elastic events form a peak at $P_{IN} \sim 0$, which is smeared by detector resolution. There is no suppression of the small values of P_{IN}.

The Monte-Carlo simulations of the phase space, the fragmentation process and isotropic resonance decay do not reproduce the dip at small values of P_{IN}. It may be possible to create the dip using the anisotropic resonance decay distributions. However, it is unclear what could cause such anisotropy, required to reproduce the observed effects.

We speculate that a pion production via gluon bremsstrahlung in the Landshoff type wide-angle scattering may create the flat part in the P_T^2 distribution and the dip in the P_{IN} distribution. The explanation is based on the idea of the gluon bremsstrahlung by the colored quarks, accelerated in the process of wide-angle scattering. The gluons could interact softly with a proton, producing a pion. The pion may retain some kinematic characteristics of the emitted gluons.

The lowest order calculations of the cross section for the wide-angle elastic scattering indicate that the Landshoff scattering should provide the dominant contribution in the scattering. However, in elastic case the higher order radiative corrections suppress the amplitude of the Landshoff process. In the $pp \to pp\pi^0$ reaction the radiation is allowed. There is no suppression of the amplitude due to the radiative corrections. In this situation, the dominance of the Landshoff type scattering may be restored.

In the wide-angle Landshoff scattering, quarks are accelerated in the direction transverse to their original direction of motion. The acceleration of quarks, colored objects, is accompanied by the radiation of the color fields. These color fields, gluons, may interact softly with the protons, producing a signle pion.

The radiation of the gluons by a proton may be suppressed for the gluon momentum smaller then the reciprocal of the size of the proton. For a normal size proton the distance between quarks is about 1 fm. Then it might be possible to see the suppression of the gluon radiation for the missing momentum squared less than 0.04 $(GeV/c)^2$.

The Lorentz contraction reduces the size of the interacting protons in the scattering plane. For a Lorentz contracted proton the suppression of the gluon radiation could occur for the missing momentum squared, which is as high as 1 $(GeV/c)^2$.

We may expect that the suppression of the gluon radiation in the scattering plane can lead to the flattening of the exponential fall-off of the P_T^2 distribution. Moreover, since the Lorentz contraction takes place in the scattering plane we could expect that the radiation is suppressed only in the P_{IN} component of the momentum.

The gluon bremsstrahlung by Lorentz contracted protons that undergo the Landshoff type wide-angle scattering may predict the flat shape of the missing P_T^2 distribution and the dip in the P_{IN} distribution. If a gluon bremsstrahlung occurs, the missing momentum could be in the direction of the radiating proton and confined to the scattering plane.

In the analysis of the angular distributions of the missing pion we observe the predicted dependences. The momentum of the missing pion is in the narrow region along the direction of the radiated particle. The $\cos(\Theta)$ distribution indicates that the missing pion is mostly in the scattering plane of the reaction.

We summarize our observations about the distributions of the $pp \rightarrow pp\pi^0$ reaction. There are unexpected trends in the momentum distributions of the missing particle. We observe a flat distribution in P_T^2 and a dip at small values in P_{IN}. We can not explain or simulate these distributions using available models of the pion production. We propose that the pion may be produced in the process of gluon bremsstrahlung by the Lorentz contracted protons, taking part in the Landshoff type wide-angle scattering. This interpretation may provide an explanation of the momentum and angular distributions of a missing pion.

6.2 Characterization of the $pp \rightarrow ppX$ reaction

In this section we summarize the results of the analysis of the inclusive $pp \rightarrow ppX$ processes.

We analyze the inclusive sample using the variable X_L. It is defined to be the fraction of incident momentum seen in the longitudinal component of the 'two-track' final state.

The shape of the X_L-distribution is a combination of the inclusive distribution and the elastic (quasi-elastic) distribution. We fit the inclusive part by a function, falling as $(1-X_L)^l$ for $X_L \rightarrow 1$. The elastic (quasi-elastic) part of the distribution is fit by a gaussian.

As the result of the fit we see that the position of the gaussian peak is at $X_L = 1$ for the distribution on Hydrogen target. However, it is different for Carbon target, the center of the gaussian peak is shifted to higher X_L.

The difference between the scattering on the Hydrogen target and scattering on the Carbon target is in the momentum distributions of the target nucleons. The proton of the Hydrogen target is at rest. The proton of the Carbon target is in motion. The momentum distribution of the nucleon is usually parametrized by a nuclear momentum distribution

function. It is defined as a probability to find a nucleon with a given momentum inside the nucleus.

The momentum distribution of the target nucleons in Carbon increases the width of the gaussian peak. However, the motion of the struck proton does not create a shift of the center of the X_L distribution on Carbon.

We argue that the shift in the X_L distribution for Carbon is the result of the combination of the strong s-dependence of the wide-angle elastic cross section and the Fermi motion of the target nucleons. We discussed the strong s-dependence of the elastic cross section in the section 4, the cross section was parametrized using the dimensional scaling power law $\sigma \sim s^{-10}$ for proton-proton scattering.

Because of the strong s-dependence, it is advantageous for the incident proton to scatter of the proton with the nuclear momentum in the same direction as the incident momentum. The CM energy is smaller than, for example, for scattering off the proton at rest.

The preferred direction of the momentum of the target nucleon is a convolution of the strong s-dependence and the Fermi momentum distribution. The result of this convolution is the shift in the X_L distribution for the Carbon target.

We observe the shift in the quasi-elastic part of the X_L distribution on Carbon, when compared to the elastic part of the X_L distribution on Hydrogen. We explain that the shift is a convolution of the strong s-dependence of the elastic cross section and the nuclear momentum distribution.

6.3 Conclusion

We underline here the main results of our research.

- We observed new effects in the momentum distributions of the missing pion in the $pp \to pp\pi^0$ reaction.
  - We saw an unexpected suppression of the missing P_T^2 distributions at low values for Carbon and Hydrogen targets.
  - There is an unexpected dip in the P_{IN} distribution at $P_{IN} \sim 0$ for Carbon and Hydrogen targets. The dip is absent in the distribution of the P_{OUT} component of the missing momentum.
- We proposed an interpretation of the unexpected suppression in the P_T distribution and dip in P_{IN} distribution. We speculated that the pion may be a product of the gluon bremsstrahlung by the Lorentz contracted protons, taking part in wide-angle Landshoff scattering. The observed momentum distributions of the missing pion could be interpreted in such model.
- In the analysis of the inclusive $pp \to ppX$ reaction we observe the new effect in X_L distributions. There is a shift in X_L for the nuclear target in the region of the quasi-elastic events. We speculate that the shift is a convolution of the nuclear momentum distribution and the strong s-dependence of the wide-angle elastic cross section.
- We provided an estimate of the transparency for the quasi-exclusive processes. The transparency T_{CH} is equal to 0.304 ± 0.011. The interpretation of the value of the transparency will require extensive theoretical calculations.

- A smooth extrapolation of the missing mass distribution toward the edge of the detector acceptance indicates that there may be an enhancement in the region of the ϕ meson mass. Future investigations may be helpful to understand the mechanism of the ϕ production in this kinematic region.

These observations of the new effects in the P_T and X_L distributions may indicate that the studied reactions have strong dependence of the cross section on the center of mass energy. However, future studies are required to fully understand if the inclusive events in $pp \rightarrow ppX$ reaction have a strong s-dependence of the cross section.

Appendix A

Correction of the C1 wiring

During the data analysis we noticed that the hits in the straw tubes of two sectors in C1 are never grouped together in a bunch of four tubes. The good trace left by a particle in a chamber looks as a bunch of tubes (Fig. A.1). In two of the sectors tube were together in the

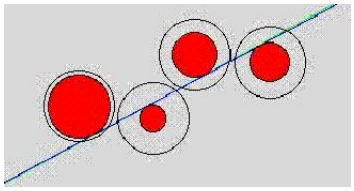

Figure A.1: The correct tube bunching in the chamber C1.

groups of two but never joined in a four-tube bunch (Fig. A.2). This problem can be caused

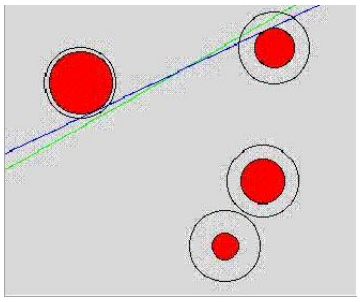

Figure A.2: The incorrect tube bunching in the chamber C1.

by the incorrect connection of the wires going from the straw tubes to the motherboard. The schematics of the connection is shown on the Figure A.3.

We realized that if the wires are interchanged between the first and the forth rows as

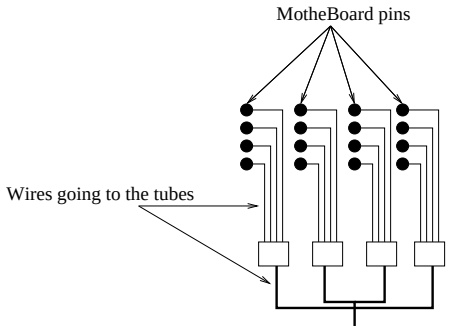

Figure A.3: The connection of the wires to the motherboard in C1.

well as between the second and the third rows (Fig. A.4), we get the pattern seen in the data. On the Figure A.4 we show the proper connection of the wires with the dashed lines.

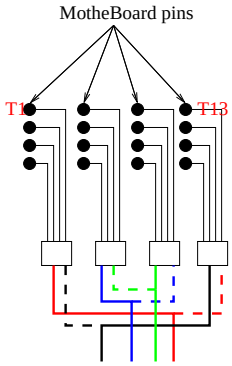

Figure A.4: The connection of the wires to the motherboard in C1.

The incorrect connection is shown with solid lines.

The Data-Aquisistion software collects the information from the wire T13 but it records it as the information for the wire T1 (Fig. A.4). The reconstruction program reads the data from the database and the RUN file. The position of the hit is in T1 instead of T13. This creates the mix up that we observed in the data.

We wrote a routine that relates the position and calibration information to the proper tubes. This routine is run when the database EVA_CONST.rz is created. The name of the routine is 'subroutine SWTUB2(chbeg,chend,swtype)'. It is a part of the 'rz_extra.f'

file, located in the 'ZONOFF/RZBASE/LIB' directory. The routine uses the input file 'swt2.cmd'. It is located in the 'ZONOFF/RZBASE/cmds98/tdc6gev' directory.

Appendix B

Parametrization of the trajectory

In this Appendix we describe the parametrization of the particle's trajectories. We described the trajectories of the particles in our detector in the section 3.2. The parametrization of the part of a trajectory inside the magnetic field is used to calculate the vertex for the event. We parametrize the trajectory with a helix. It has the axis along the Z-axis of the coordinate system of the detector. Helix has an arc as a projection in XY-plane.

The equations of the helix in the cartesian coordinate system are

$$x = x_c + Rcos(\omega t + \phi_0) \tag{B.1}$$

$$y = y_c + Rsin(\omega t + \phi_0)$$

$$z = z_0 + V_{||}t \qquad\qquad \omega = \frac{V_\perp}{R} = \frac{V_{||}}{R * tg(\theta)}$$

Here x_c, y_c are the coordinates of the center of the arc in the XY-plane, R is the radius of the arc and ϕ_0 is the ϕ angle of the track (we will call it the helix phase). The variables $V_{||}$ and $V_\perp$ are the velocities parallel and perpendicular to the Z-axis.

We use a special coordinate system to find the parameters of the trajectory (section 3.2.3). The circular trajectory is approximated by a parabolic trajectory. The formula for a fit in the special coordinate system is $y = cx^2/2 + bx$.

We use the formulas for the curvature and center coordinates of the non-linear curve

$f(x)$ to find R,x_c,y_c.

$$x_c = x - \frac{\frac{df(x)}{dx}(1+(\frac{df(x)}{dx})^2)}{\frac{d^2f(x)}{dx^2}} \qquad (B.2)$$
$$y_c = y + \frac{(1+(\frac{df(x)}{dx})^2)}{\frac{d^2f(x)}{dx^2}}$$
$$R = \frac{(1+(\frac{df(x)}{dx})^2)^{3/2}}{\frac{d^2f(x)}{dx^2}}$$

The arc passes through the point (x,y)=(0,0) in the special coordinate system. We use this point to evaluate the equations B.2. The parameters of the track are

$$x_c = -\frac{b(1+b^2)}{c} \qquad y_c = \frac{1+b^2}{c} \qquad R = \frac{(1+b^2)^{3/2}}{c}. \qquad (B.3)$$

We substitude $V_\perp$ in the equations B.2 using the Z,Z_0 and $tg(\theta)$. As a result we have equations that define the X and Y coordinates of the particle as a function of the Z coordinate.

$$x = x_c + Rcos(\phi_0 - \frac{(z-z_0)tg(\theta)}{R}) \qquad (B.4)$$
$$y = y_c + Rsin(\phi_0 - \frac{(z-z_0)tg(\theta)}{R})$$

There is a function that returns X, Y, Z for a given Z in the reconstruction code. It is a member of the track class. It's name is track::fxyz(float z). It is used in the calculation of the vertex position for an event.

Appendix C

The Glauber approach

In this chapter we discuss the Glauber approach in the hadron-nucleus scattering.

In naive picture of a hadron scattering on nucleus, the incoming and out-going hadrons do not interact with the nucleus. At high energy this approach is called Plane Wave Impulse Approximation (PWIA). The hadron-nucleus scattering amplitude in this approach depends on the amplitude of the elastic hadron-nucleon scattering and the nucleus spectral function. The nucleus spectral function is interpreted as a probability to find a nucleon with a given momentum at a given energy in the nucleus.

The initial and final state interactions of the hadrons are taken into account in the Plane Wave Impulse Approximation with Distorted Waves [61]. Mostly, the hadrons experience relatively soft interactions with individual nucleons of a nucleus. In this approach, the initial and final state interactions lead to the production of pions or to the knock out of slow nucleons from the nucleus. In either case, the reaction becomes inelastic.

In the Glauber method the interaction of the hadrons with nucleus is described by the absorption factors. The absorption factor determines attenuation of the yield due to the interaction of the hadrons with the nuclear medium. It depends on the density of the nucleons in the nucleus and the cross section of the hadron interaction with individual nucleons. The schematic picture of the interaction in the nucleus is given on the Figure C.

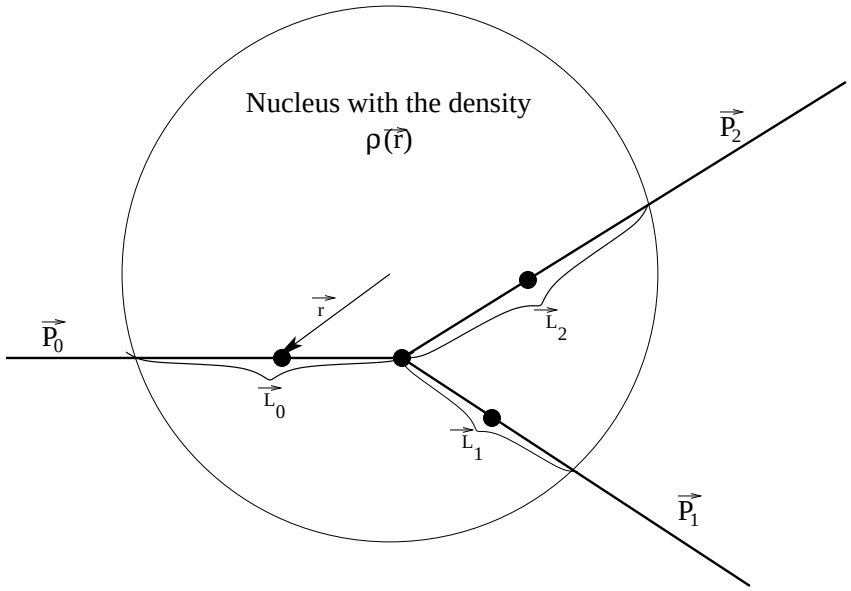

Figure C.1: The passage of hadrons through the nucleus before and after the interaction .

The absorption coefficient for i-th hadron, passing through the nucleus, is given by the following formula:

$$\phi_i(\vec{r}) = e^{-.5\int \sigma_{hN}^{tot}\rho(\vec{r}-\frac{\vec{p_i}}{p_i}L)dL}. \tag{C.1}$$

The integration is performed over the length of the hadron path L_i. The hadron path is taken from the point of the hard interaction along the hadron trajectory in the nucleus.

In the limit $\sigma_{hN}^{tot} \to 0$ the Glauber method is identical to the PWIA. The calculations in the Glauber approach were succesfully used to parametrize the data on the quasi-elastic knock-out of the protons and neutrons from Carbon nucleus [62].

The Glauber model does not include the specifics of the interaction of the PLC with nucleons. However, one can account for the effects of **color transparency**. The total cross section σ_{hN}^{tot} should be replaced by the cross section of the PLC with nucleons $\sigma_{PLC,N}^{tot}$. The resulting absorption coefficient depends on the type and on the expansion mechanism of

the PLC. In the outcome, the nuclear transparency will be modified.

Appendix D

The 'star dust' process

In this Appendix we calculate the cross section of the 'star dust' or the fragmentation process. As we discussed earlier the 'star dust' process can be schematically described by the diagram on the Figure D.1. The components of the cross section for this process are

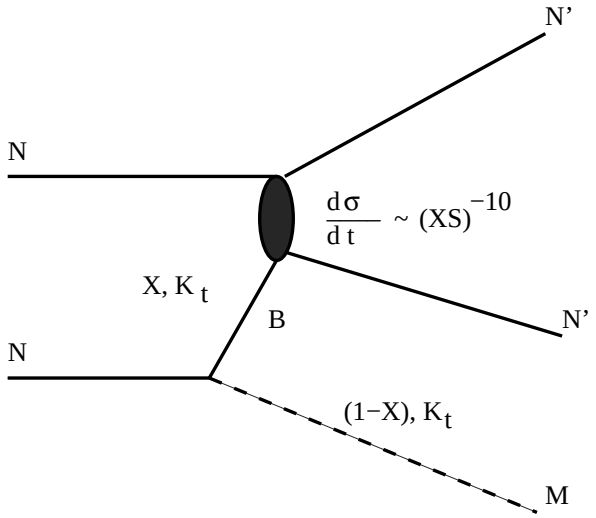

Figure D.1: The "Star dust" process diagram.

the splitting function $f_{\pi NN}$ and $\sigma_{NB\to N'N'}$.

The form of the pion splitting function was discussed by Sullivan [63]. Sullivan estimated the contribution to the electromagnetic structure function of the proton from the one pion exchange in reaction with virtual photon (Fig. D.2). For this case the splitting function is

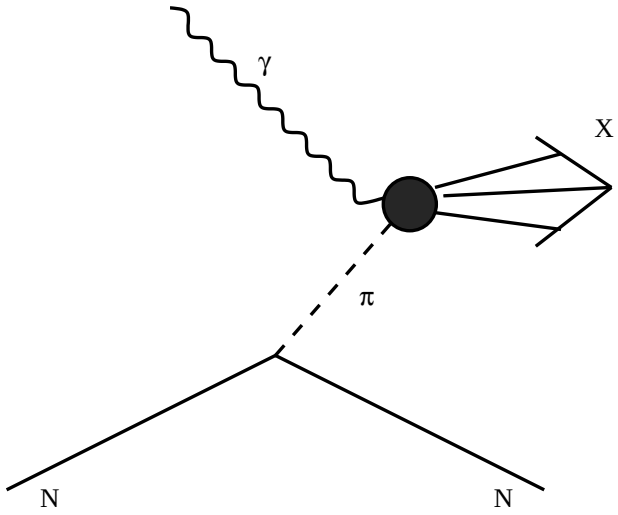

Figure D.2: Pionic contribution to the nucleon form-factor in the Sullivan process. It is based on the one-pion exchange model.

given by [64]

$$f_{\pi NN} = \frac{3yg^2_{\pi NN}}{16\pi^2}\int dt \frac{-t}{(t-m_\pi^2)^2}(F_{\pi NN}(t))^2. \tag{D.1}$$

Here t is the pion four-momentum, $g_{\pi NN}$ is the coupling constant, y is the pion's longitudinal momentum fraction and $F_{\pi NN}(t)$ is the form-factor for emission of the off-shell pion.

The cross section for hadron scattering via one pion exchange (Fig. D.3) is well known (see Zoller [65] for example). The complete formula for cross section of the process on the

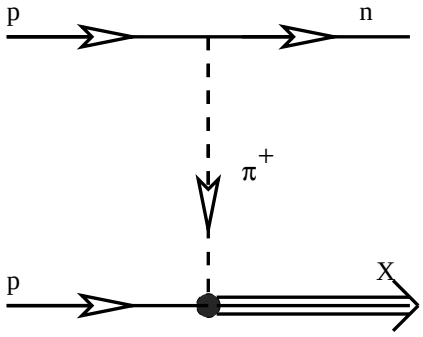

Figure D.3: A diagram of the hadron-hadron scattering via the one pion exchange.

Fig. D.3 is following

$$E\frac{d^3\sigma}{d^3p} = \frac{g^2_{\pi pp}}{(2\pi)^3}\frac{-tG^2_{\pi NN}(x,p_t^2)}{(t-m_\pi^2)^2}(1-x)\sigma^{tot}_{\pi p}(s(1-x)). \tag{D.2}$$

Here x is the fraction of the CM longitudinal momentum ($x = \frac{2p^*_z}{\sqrt{s}}$) carried by the neutron. After the substitution $x \to 1-x$ and using proper $\sigma_{pp}(s)$ we get the cross section formula for the pion fragmentation with the consequent hard scattering (Fig. 4.15).

This cross section formula has a nucleon form-factor. There are several types of the form-factors discussed in literature [65, 66].

$$\begin{aligned} &G(t) = (\frac{1-m_\pi^2/\Lambda^2}{1-t/\Lambda^2})^n \qquad n = 1,2 \\ &G(t) = e^{\frac{t-m_\pi^2}{\Lambda^2}} \\ &t = m_\pi^2 - (1-x)(\frac{m_N^2+p_t^2}{x} + \frac{m_\pi^2+p_t^2}{1-x} - m_N^2) \end{aligned} \tag{D.3}$$

We will use the exponential form-factor for Monte-Carlo simulations in Chapter 5.

Finaly, the complete formula for the 'star dust' process of the Figure D.1:

$$E\frac{d^3\sigma}{d^3p} = \frac{g^2_{\pi pp}}{(2\pi)^3}\frac{-te^{\frac{t-m_\pi^2}{\Lambda^2}}}{(t-m_\pi^2)^2}x\sigma^{tot}_{\pi p}(s*x). \tag{D.4}$$

Here $t = m_\pi^2 - x(\frac{m_N^2+p_t^2}{1-x} + \frac{m_\pi^2+p_t^2}{x} - m_N^2)$.

Appendix E

Data on inclusive π^0 production

In this appendix we give a summary of the data from several experiments, that studied the inclusive π^0 production.

The production of π^0 in pp collisions was studied by Abolins *et al* [51]. They detected pions in semi-exclusive reaction $pp \to pp\pi^0$ and in more inclusive case of $pp \to pp + m\pi^0$ ($m \geq 1$). The differential cross section they obtained is plotted on the Figure E.1. Over the range of P_T where our distributions are flat, Abolins *et al* observe a drop of more then an order of magnitude in differential cross section. On the same figure we see a distribution for K_s^0 production in inclusive $pp \to p + K_s^0 + anything$ reactions. It has a similar dependence. The fits with $exp(a + bP_T^2 + cP_T^4)$ are shown as solid lines. The slopes of the exponents are the same within the accuracy of the measurements.

A number of other experiments detected pions in collisions of the proton beam with nuclear targets.

Abraamyan *et al* [67] obtained the differential cross section $\frac{d\sigma}{dP_T^2}$ for inclusive π^0 production in pC and pCu collisions ($pC \to \pi^0 + X$) at the beam momentum of 4.5 GeV/c. The differential cross section shows an exponential drop with P_T^2 (Fig. E.2). There are restrictions imposed on the kinematic variables of the π^0. The angle of the pions in the LAB frame is restricted to be less then 16°. The energy of the pions is $E > 2$ GeV.

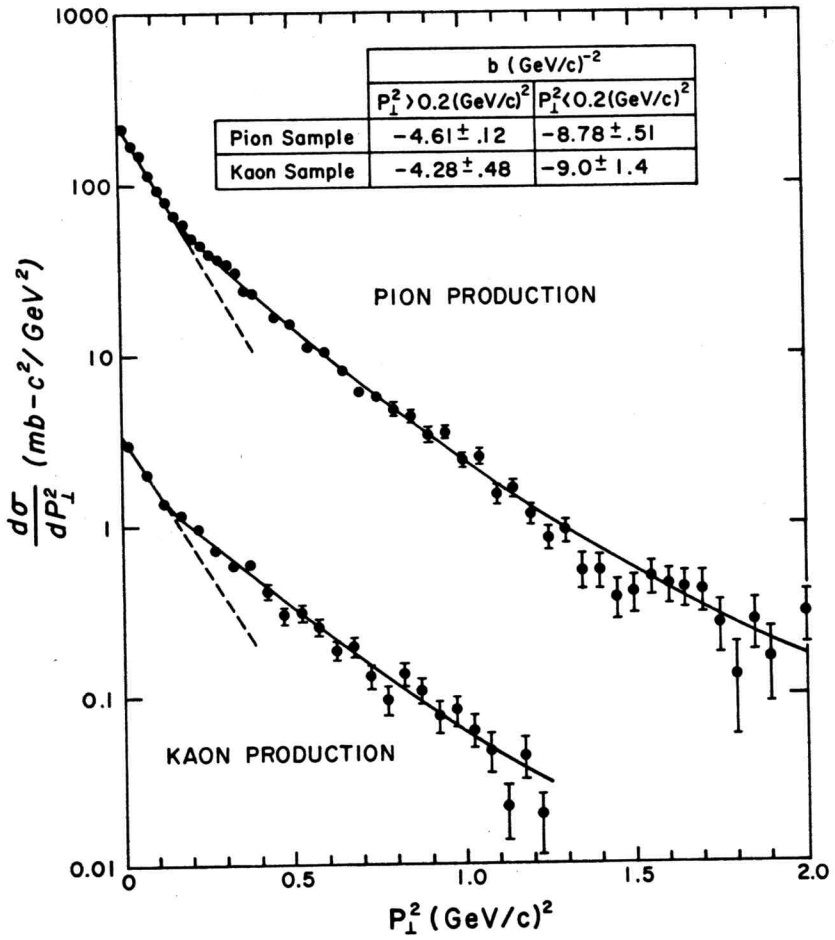

Figure E.1: $\frac{d\sigma}{dP_T^2}$ distribution for $pp \to pp+m\pi^0$. The measurement of the proton scattering on Hydrogen in the bubble chamber (Abolins *et al*).

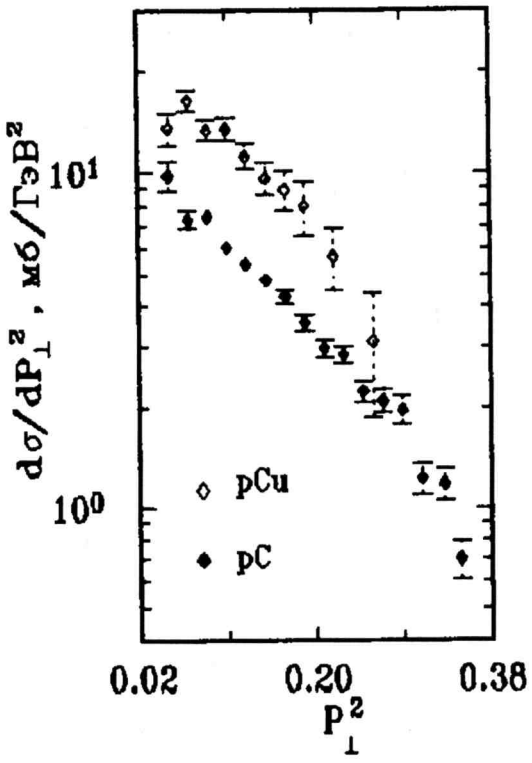

Figure E.2: $\frac{d\sigma}{dP_T^2}$ distribution for $pC \to \pi^0 + X$ and $pCu \to \pi^0 + X$. The measurement of the proton scattering on Carbon and Copper targets at 4.5 GeV/c incoming beam momentum (Abraamyan *et al*).

The differential cross section of the production of the π^0 in Au+Au collisions was measured by Teis *et al* [68]. In the restricted rapidity range the differential cross section $\frac{d\sigma}{dP_T^2}$ has an exponential trend seen in other experiments (Fig. E.3).

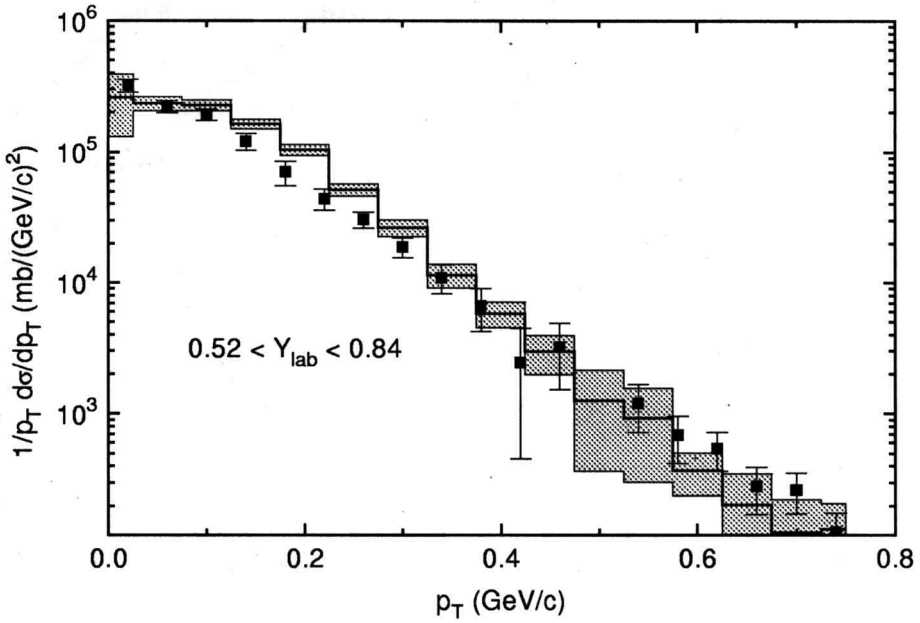

Figure E.3: $\frac{d\sigma}{dP_T^2}$ distribution for $Au + Au \rightarrow \pi^0 + X$. The measurement of the inclusive production of π^0 in Au-Au collisions at the energies of 1-2Gev/A (Teis *et al*).

The exponential dependence of the differential cross section was also observed in production of ρ and f mesons in $\pi^+ p$ collisions at 8,16 and 23 GeV/c beam momenta [69]. The ρ and f productions were measured in the inclusive $\pi^+ p \rightarrow \pi^+ \pi^- + X$ reactions. The $\frac{d\sigma}{dP_T^2}$ is shwon on the Figure E.4. The fits to the form $Aexp(-BP_T^2)$ are shown as solid lines.

All the experiments show the drop in the $\frac{d\sigma}{dP_T^2}$ cross section by at least an order of magnitude in the region of P_T^2 up to 0.7 $(Gev/c)^2$.

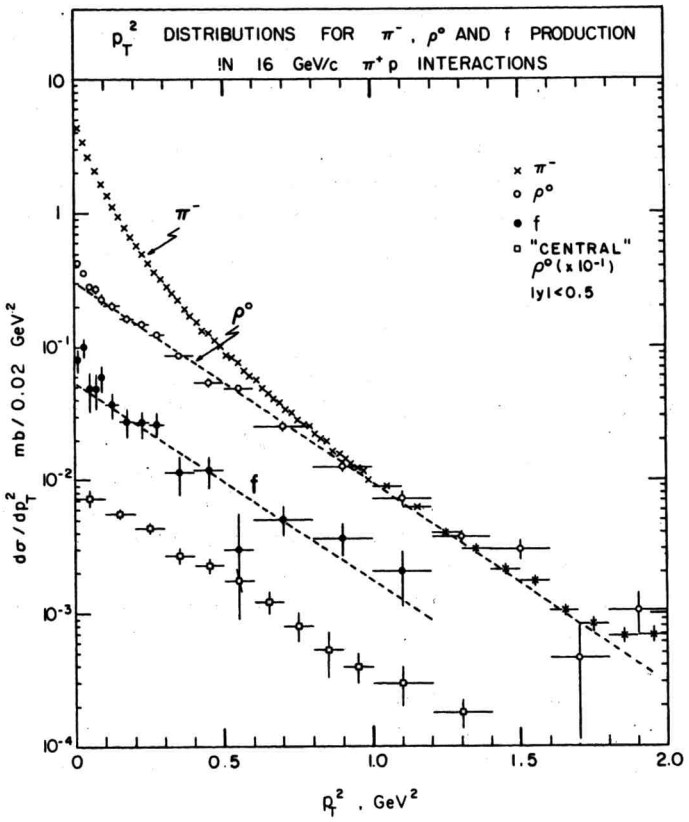

Figure E.4: $\frac{d\sigma}{dP_T^2}$ distribution for ρ and f production. The measurement of the inclusive ρ and $f(1270)$ production in $\pi^+ p$ collisions at 8,16 and 23 GeV/c (Deutschmann *et al*).

Bibliography

[1] D.Zhalov and et al, in *Proceedings of 7th Conference on Intersections Between Particle and Nuclear Physics (CIPANP 2000),Quebec City, Quebec, Canada*, edited by A. B. MacInnis (MIT, Middleton, MA 01949 USA, 2000).

[2] S.F.Heppelmann and et al, to be published in Phys.Rev.Lett. (2001).

[3] A. Leksanov, Ph.D. thesis, Penn State University, State College, PA, 2000.

[4] S.J.Brodsky and G.R.Farrar, Phys.Rev.Lett. **31**, 1153 (1973).

[5] S.J.Brodsky, in *Proceedings of the Thirteenth International Symposium on Multiparticle Dynamics, Volendam, The Netherlands*, edited by W. Kittel (World Scientific, Singapore, 1983).

[6] L.L.Frankfurt, G.A.Miller, and M.Strikman, Ann.Rev.Nucl.Part.Sci. **45**, 501 (1994).

[7] L.Frankfurt, G.A.Miller, and M.Strikman, Nucl.Phys. **A555**, 752 (1993).

[8] L.L.Frankfurt, M.I.Strikman, and M.B.Zhalov, Phys.Rev.C **50**, 2189 (1994).

[9] L.Frankfurt., M.Strikman, and M.Zhalov, Phys.Lett. **B503**, 73 (2001).

[10] B.Z.Kopelovich and B.K.Jennings, Phys.Rev.Lett. **70**, 3384 (1993).

[11] S.J.Brodsky and G. de Teramond, Phys.Rev.Lett. **60**, 1924 (1988).

[12] J.P.Ralston and B.Pire, Phys.Rev.Lett. **61**, 1823 (1988).

[13] A.S.Carroll and et al, Phys.Rev.Lett. **61**, 1698 (1988).

[14] M.R.Adams and et al, Phys.Rev.Lett. **74**, 1525 (1995).

[15] D.Ashery and et al, Nucl.Phys.Proc.Suppl. **90**, 67 (2000).

[16] T.G.O'Neil and et al, Phys.Lett. **B351**, 87 (1995).

[17] I.Mardor and et al, Phys.Rev.Lett. **81**, 5085 (1998).

[18] A.Malki and et al, to be published in Phys.Rev.D. (2001).

[19] M.Strikman and M.Zhalov, Nucl.Phys. **A670**, 135c (2000).

[20] M.Strikman and M.Zhalov, *KEK-Tanashi Symposium on Physics of Hadrons and Nuclei* (Tokyo, Japan, 1998).

[21] D.Andrews and et al, A Superconducting Solenoid for Colliding Beam Experiments, 1982.

[22] J.Wu, Ph.D. thesis, Penn State University, State College, PA, 1991.

[23] F.J.Barbosa and et al, Large Cylindrical Straw Tube Arrays for the EVA Detector, 1991.

[24] J.Fisher, A.Hrisoho, V.Radeka, and P.Rehak, Proportional chambers for very high counting rates based on gas mixtures of CF_4 with hydrocarbons.

[25] U.A.Kasanskii, A.I.Abramov, and E.S.Matusevich, in *Basics of the Experimental Methods in Nuclear Physics*, edited by A.I.Melnikova (Atomizdat, 113114,Moscow,USSR, 1970), p. in Russian.

[26] A.Zastawny, Nucl.Instr.and Meth. **A 385**, 239 (1997).

[27] S. Durant, Ph.D. thesis, Penn State University, State College, PA, 1991.

[28] J.Wu and et al, Nucl.Instrum.Meth. **A349**, 183 (1994).

[29] J.F.Gunion, J.F.Brodsky, and R.Blankenbecler, Phys.Rev. 1 (1973).

[30] S.J.Brodsky, *Nuclear and Particle Physics Summer School* (Launceston, Australia, 1987).

[31] S.J.Brodsky and G.R.Farrar, Phys.Rev. D **11**, 1309 (1975).

[32] P.V.Landshoff, Phys.Rev. D **10**, 1024 (1974).

[33] A.Donnachie and P.V.Landshoff, Particles and Fields **2**, 55 (1979).

[34] J.Botts and G.Sterman, Phys.Lett. B **224**, 201 (1989).

[35] A.H.Mueller, Phys.Rep **73**, 237 (1981).

[36] V.V.Sudakov, Soviet Physics JETP **3**, 65 (1956).

[37] C.W.Akerlof and et al, Phys.Rev. **159:5**, 1138 (1967).

[38] A.S.Carroll and et al, Phys.Rev.D **49:1**, 58 (1988).

[39] J.W.Cronin and et al, Phys.Rev.Lett. **31**, 1426 (1973).

[40] A.E.Chudakov, Izv.Akad.Nauk 650 (1955).

[41] M.Strikman, L.L.Frankfurt, G.R.Farrar, and H.Liu, Phys.Rev.Lett. **61**, 686 (1988).

[42] A.G.Sitenko, in *Theory of nuclear reactions*, edited by L.V.Belova (Energatomizdat, 113114,Moscow,USSR, 1983), p. in Russian.

[43] B.K.Jennings and G.A.Miller, Phys.Rev.D **44**, 692 (1991).

[44] N.C.R.Matkins and et al, Phys.Rev.Lett. **72**, 1986 (1994).

[45] Y.Golubeva and et al, Phys.Rev.C **57**, 2618 (1998).

[46] N.N.Nikolaev and et al, Phys.Rev.C **50**, 1296 (1994).

[47] A.Malki, Master's thesis, Tel-Aviv University, Tel-Aviv, Israel, 2000.

[48] C.M.Ankenbrandt and et al, Phys.Rev. **170**, 1223 (1968).

[49] J.V.Allaby and et al, Phys.Lett. **34B**, 435 (1971).

[50] E.Colton, Z.M.Ma, G.A.Smith, and P.E.Schlein, Phys.Rev.D **7**, 3267 (1973).

[51] M.A.Abolins and et al, Phys.Rev.Lett. **25:2**, 126 (1970).

[52] C. degli Atti and S.Simula, Phys.Rev.C **53**, 1689 (1996).

[53] S.Okubo, Phys.Rev.D **16:7**, 2336 (1977).

[54] V.Blobel and et al, Phys.Lett. **59B**, 88 (1975).

[55] A.Shor, Phys.Rev.Lett. **54:11**, 1122 (1985).

[56] J.Rafelski and B.Muller, Phys.Rev.Lett. **48:16**, 1066 (1982).

[57] J.Rafelski, Nucl.Phys. **A418**, 215c (1984).

[58] S.J.Brodsky and J.F.Gunion, Phys.Rev.D **17**, 848 (1978).

[59] J.F.Gunion, Phys.Rev.D **10**, 242 (1974).

[60] E. Piasetzky, Private communications (2001).

[61] R.Bengtsson and et al, Phys.Rep. **41**, 193 (1978).

[62] S.Belostotsky and et al, in *Proceedings of the International Symposium on Modern Development in Nuclear Physics* (World Scientific, Singapore, 1987), p. 191.

[63] J.D.Sullivan, Phys. Rev. **D5**, 1732 (1972).

[64] W.Melnitchouk, A.W.Thomas, and A.I.Signal, Hadrons and Nuclei **340**, 85 (1991).

[65] V.R.Zoller, Particles and Fields **53**, 443 (1992).

[66] J.Speth and A.W.Thomas, Adv.Nucl.Phys. **24**, 83 (1998).

[67] Abraamyan and et al, Yad.Fiz. **59:2**, 271 (1996).

[68] S.Teis, Ph.D. thesis, Institut fur Theoretische Physik, Universitat Giessen, D-35392 Giessen, Germany, 1997.

[69] M.Deutschmann and et al, Nucl.Phys. **B103**, 426 (1976).

VITA

NAME:

Daniel Zhalov

BORN:

August 25, 1974
Leningrad, USSR

EDUCATION:

1990-1995 B.S. in Physics and Mathematics,
The Saint Petersburg Technical State University
St. Petersburg, Russia

1995-2001 Ph.D. in Physics,
The Pennsylvania State University
University Park, PA

EMPLOYMENT:

1996-2001 The Pennsylvania State University
University Park, PA
Research/Teaching Assistant
Physics Department, Laboratory of Elementary Particles Science

As of 09-04-2001 MIS Analyst
Capital One
4801 N Park road
Glen Allen, VA, 23060

TECHNICAL PUBLICATIONS:

- D. Zhalov et al, Longitudinal Momentum Fraction X_L for Two High P_t Protons in $pp \to ppX$ Reaction
  Ref: nucl-ex/0009007
- A. Leksanov et al, A New Measurement of the Energy Dependence of Nuclear Transparency for Large Momentu m Transfer ^{12}C(p,2p) Scattering
  Ref: nucl-ex/0009008
- An Tang et al, n-p Short-Range Correlations from (p,2p+n) Measurements
  Ref: nucl-ex/0009009
- A. Malki et al, Backward emitted high-energy neutrons in hard reactions of p and π^+ on carbon
  To be published in PRD, Ref: nucl-ex/0005006
- S. Heppelmann et al, Energy Dependence of Nuclear Transparency in C(p,2p) Scattering
  To be published in PRL, Ref: hep-ex/0104039